DENSITY FUNCTIONAL TIGHT-BINDING STUDY OF Li-INTERCALATION IN β-MnO_2 FOR LITHIUM-ION BATTERIES

By

NGOBENI PERCY

Submitted in fulfillment of the requirements for the degree of

MASTER OF SCIENCE

In

PHYSICS

In the

FACULTY OF SCIENCE AND AGRICULTURE

(School of physical and mineral sciences)

At the

UNIVERSITY OF LIMPOPO

SUPERVISOR: Dr K.P Maenetja

CO-SUPERVISOR: Prof P.E Ngoepe

2022

ABSTRACT

The derivation of β-MnO_2 potentials was carried out using self-consistent density functional tight-binding (SSC-DFTB) parameterization within Material Studio®. For exchange-correlation functional, the generalized gradient approximation (GGA) was used in the form of PBE exchange-correlation functional during parameterization. $Dmol^3$ is a density functional theory-based program that is used to calculate the lattice parameter of ferromagnetic β-MnO_2. The potentials were used in the investigation of the structural and electronic properties of β-MnO_2. After successfully parameterizing β-MnO_2, the lattice parameters were compared with the results from experiments and Density Functional Theory. Density functional tight-binding (DFTB) was employed to investigate the electronic properties of β-MnO_2 such as density of states (DOS) and band structures. The DOS was calculated to check the nature of the investigated system. The electronic band structures calculated were also to confirm the results of the DOS since they go hand in hand.

We further employed the Density Functional Theory to investigate the surfaces (110) of β-MnO_2, β-TiO_2, and β-VO_2 which act as catalysts in Li/Na-air batteries. We investigated the electronic properties of metal oxides β-MnO_2, β-TiO_2, and β-VO_2 (MO_2) which are used as a catalyst in metal-air batteries. Electronic properties of MO; MnO_2, TiO_2, and VO_2 were determined by looking at the tetragonal structure. However, further investigations of the electronic properties of oxygen adsorption Li/MO_2 and Na/MO_2 (110) surfaces in metal-air batteries.

DECLARATION

I declare that the report hereby submitted to the University of Limpopo for the degree of Master of Science has not been earlier submitted by me for a degree at this or any other university: that it is my work in strategy and execution, and that all material contained therein has been duly acknowledged.

14 September 2022

NGOBENI P

Date

ACKNOWLEDGMENTS

Firstly, I would like to thank the almighty God, for this project was possible and successful because of Him. The work presented was carried out under the supervision of Professor P.E. Ngoepe and Doctor K.P. Maenetja from Material Modelling Centre, University of Limpopo. I would also like to thank all my colleagues in the Material Modelling Centre and the Department of Physics for being cooperative during the execution of this work.

Special appreciation to the National Research Fund (NRF) and Material Modelling Centre for the financial support provided during the period of this work.

DEDICATION

This work is dedicated to:

My Parents

David and Dorris

My Siblings

Nonhlanhla and Nhlaluko

CONTENTS

List of acronyms

LA - Longitudinal Acoustic

TA - Transverse Acoustic

LO - Longitudinal Optical

TO - Transverse Optical

DFTB – Density Functional tight binding

DFT – Density Functional Theory

ORR – Oxygen Revolution Reaction

OER – Oxygen Evolution Reaction

CASTEP – Cambridge Sequential Total Energy Package

VASP – Vienna Ab-initio Simulation Package

GGA – Generalized Gradient Approximation

LDA – Local Density Approximation

HEG – Homogeneous Electron Gas

SCC – Self-consistent-charge

USP – Ultra-soft pseudo-potentials

DOS – Density of States

E_f – Fermi level

List of figures

List of tables

Chapter 1: Introduction

1.1. Rationale

Energy storage exists to progress the unwavering quality and execution of frameworks to coordinate them into the control framework network. For the past two decades, lithium-ion batteries exist as the source of control for individual computerized electronic change [1]. Standard of living activity embraces the total performance of portable hardware which requests progressed Li-ion batteries, cell phone charges with an increased part that's a reduced sum of commonly than the current phone and will improve the quality of people's life. They give high energy, but control density remains too low for high control applications. A challenge is to actualize battery innovation in large-scale high-power frameworks, while a developing commercial center for Li-ion batteries in electric vehicles and crossbreed vehicles requires Li-ion batteries with not as it were high power, high capacity, high charging rate, and long life but moreover progressed security performance and low cost [2].

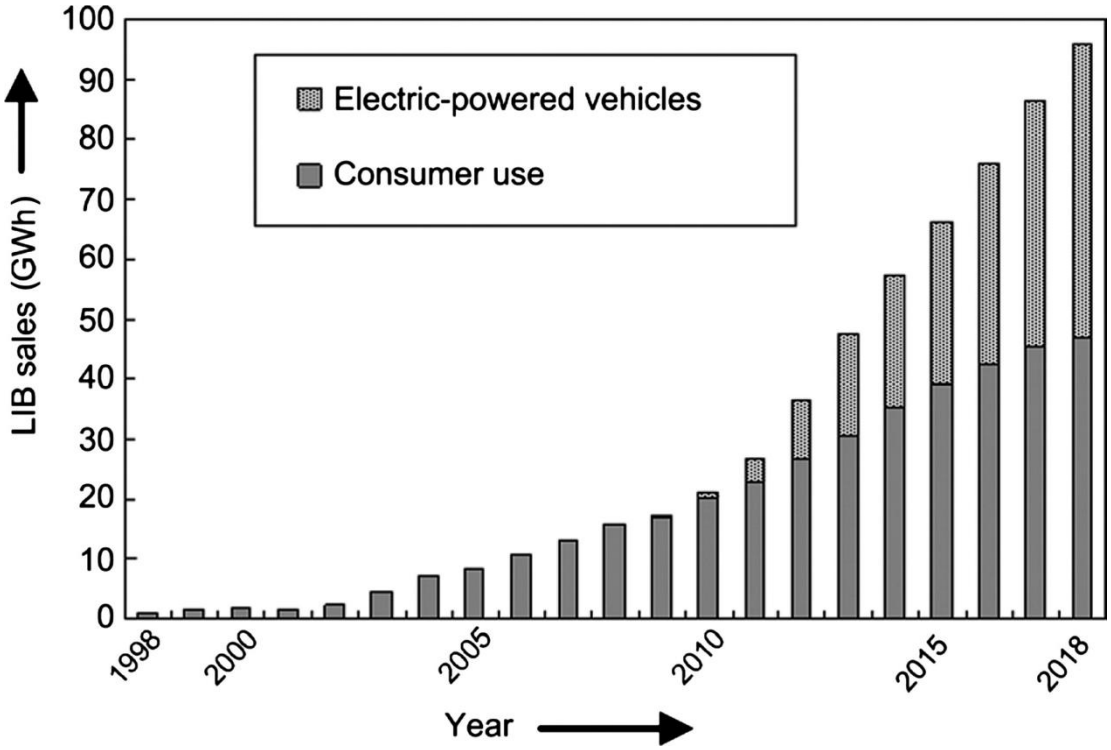

Figure 1.1: Insistence of Li-ion batteries in the last two decades.

Figure 1.1 above, appears that there is a fast increment in requests for Li-ion over a long time in electric-powered vehicles which are anticipated to assemble the requests for consumer use. Li-ion batteries are utilized to shield the rotating and changing green vitality supply from renewable assets, such as sun-based and wind, to smooth the distinction between energy supply and demand. For illustration, extrasolar energy created during the daytime can be saved in Li-ion batteries that will give energy at night when daylight is inaccessible [2].

As progressively extreme issues of natural contamination and asset exhaustion are brought around by the current fossil fuel-based energy framework, the requirements for clean and renewable energy sources are getting to be progressively pressing. The battery storage system is a green and profoundly proficient end-use energy. These days, electrochemical energy-storage gadgets with different time scales and measurement scales have entered each perspective of our existence, counting smart grids, electric vehicles, and smart portable gadgets. Amid the investigation of the history of electrochemical energy capacity, the inquiry about advances in materials science has to a great extent advanced the improvement and commercialization of electrochemical energy-storage gadgets such as Li-ion batteries. With intense efforts applied to materials research, the future application of more sorts of electrochemical energy-storage gadgets provides an advantage.

Metal-air batteries are a family of electrochemical cells fueled by metal oxidation and oxygen reduction, showing an extraordinary advantage concerning theoretical energy density, which is approximately 3-30 times higher than commercial Li-ion batteries [3]. Li-air batteries and Zn-air batteries are two sorts of metal-air batteries that have attracted the foremost attention. Li-air batteries (with Li_2O_2 as the discharge product)

can provide a predominant hypothetical execution of a huge energy density of 11,429 W h kg^{-1} (based on the mass of Li metal), a high specific capacity of 3,860 mAh g^{-1} (based on the mass of Li metal), and a cell voltage as high as 2.96 V [4]. Other than Li-air and Zn-air batteries, other types of metal-air batteries have their claimed superiorities. For illustration, Al-air batteries show the highest volumetric capacity (8,040 AhL^{-1}) [5], and Na-air batteries appear littler charge overpotentials than Li-air batteries. Hence, the metal-air battery family has extraordinary potential to serve as next-generation electrochemical energy-storage gadgets. Catalysts are often required to facilitate the ORR and OER, and metal oxide catalysts are incorporated to enhance the performance of metal-air batteries to measure overall cell performance with reciprocating efficiency and charge/discharge rate.

1.2. Structural aspects

The MO_2 (M= Mn, Ti, and V) bulk structure occurs in the tetragonal space group $P4_2/mnm$ as shown in Figure 1.2 below. The dominant structural constructing block is the MnO_6 octahedra which might be side-sharing alongside the c-axis and corner-sharing within the plane. The MO_2 systems are isostructural, and the distances between atoms are displayed in table 1.3 underneath.

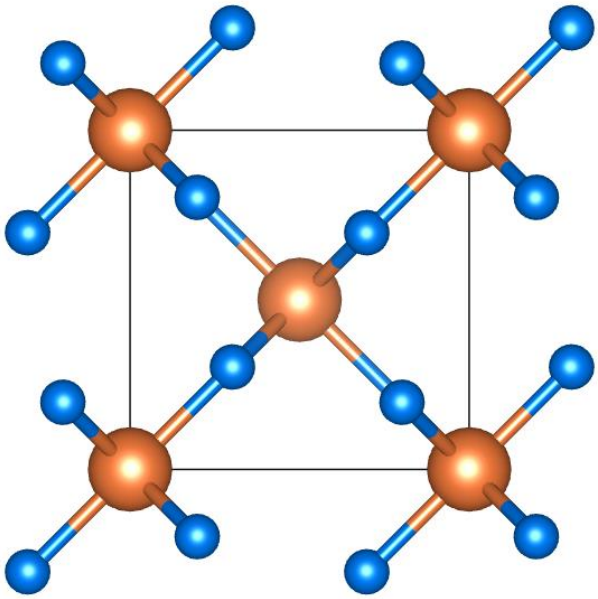

Figure 1.2: Primitive tetragonal structure for rutile MO_2, with brown spheres representing the metallic atom (Mn, Ti, and V) and blue spheres representing the oxygen atom.

Table 1.1: Lattice parameters of the MnO_2, TiO_2, and VO_2 bulk structures

Structure	a (Å)		c (Å)		V ($Å^3$)
β-MnO_2	4.366 [6]	4.410 [7]	2.961	2.887 [8]	56.44
β-TiO_2	4.627 [6]	4.954 [9]	3.008	2.959 [10]	64.40
β-VO_2	4.617 [6]	4.554 [7]	2.774	2.857 [8]	59.13

Table 1.2: Atoms present within the bulk structure for the metal oxides with positions of atoms

MnO_2		TiO_2		VO_2	
Atoms	Distance	Atoms	Distance	Atoms	Distance
Mn-O	1.8834	Ti-O	1.9553	V-O	1.9007
Mn-O	1.8834	Ti-O	1.9553	V-O	1.9621
Mn-O	1.8933	Ti-O	1.9823	O-O	2.5133
Mn-O	1.8933	Ti-O	1.9823	O-O	2.7318
Mn-Mn	2.8873	Ti-Ti	2.9635	O-O	2.8520
Mn-O	3.3304	Ti-O	3.4989	O-O	3.2951
Mn-Mn	3.4224	Ti-O	3.4989	V-O	3.4554
Mn-O	3.4527	Ti-O	3.5654	V-O	3.4617
Mn-O	3.4527	Ti-O	3.5654	O-O	3.8014
Mn-O	3.9112	Ti-Ti	3.5792	O-O	3.9242

Table 1.3: Coordinates of atoms within the bulk structure for the MO_2

Site	Wyckoff position	Element	X	Y	Z	Occupancy
MnO_2						
Mn1	2a	Mn	0.00000	0.00000	0.00000	1.0
O1	4f	O	0.30200	0.30200	0.00000	1.0
TiO_2						
Ti1	2a	Ti	0.00000	0.00000	0.00000	1.0
O1	4f	O	0.30540	0.30540	0.00000	1.0
VO_2						
V1	2a	V	0.00000	0.00000	0.00000	1.0
O1	4f	O	0.30479	0.30479	0.00000	1.0

1.3. Literature Review

1.3.1. Structural properties

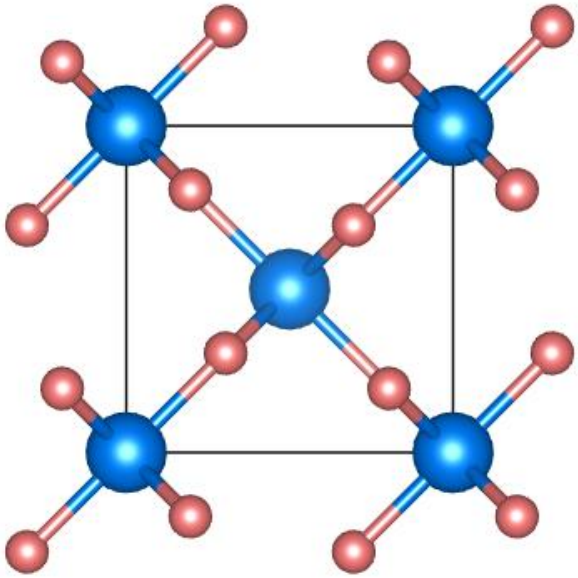

Figure 1.3: The β-MO_2 structure with the same space group P42/mnm. Oxygen is represented through brown atoms, and the blue atoms represent the M atoms.

The three rutile metal oxide systems, β-MnO_2, β-TiO_2, and β-VO_2 have a tetragonal lattice with space group $P4_2$/mnm as shown in figure 1.3 above, and their oxygen is characterized by a primitive tetragonal packing [11]. The MnO_2 system exists in diverse types of polymorphs that are based on the assembly of the octahedral MnO_6 subunits shared within corners or edges. The octahedral MnO_6 units that are shared between corners or edges result in MnO_2 tunnels that permit the access of reactants to the effective reaction sites as well as the absorption of tiny molecules within the structure.

The two-dimensional structure of β-MnO_2 allows for the continuous intercalation or deintercalation reaction of cationic species with the material. β-MnO_2 has poor ionic insertion properties and is not suitable for intercalation into lithium. It is narrow (1 x 1) tunnels that make it difficult to accommodate lithium during intercalation. The

properties of pyrolusite MnO_2, rutile VO_2, and rutile TiO_2 are comparable to those of the P42mnm space group.

1.3.2. Surface structure and properties

Simulation studies are of extraordinary significance in attempts to completely get it surface structures and properties of metal oxides. Stoichiometric and inadequate terminations of the β-MnO_2 (110), (100), and (101) surfaces have been explored as a work of oxygen fractional pressure and temperature utilizing ab initio thermodynamics [12]. The evaluated steadiness of the (110), (100), and (101) stoichiometric surfaces follow the patterns already obtained for rutile TiO_2 [13], MnO_2 [14], VO_2 [15], and rutile-type SnO_2: (100)<(101)<(110) [12]. The (110) surfaces for TiO_2, MnO_2, and VO_2 are anticipated to be the steadiest surfaces by different researchers followed by the (100) surface and then (101) surface. For the most part, the stoichiometric surfaces are anticipated to be examined beneath naturally favourable conditions.

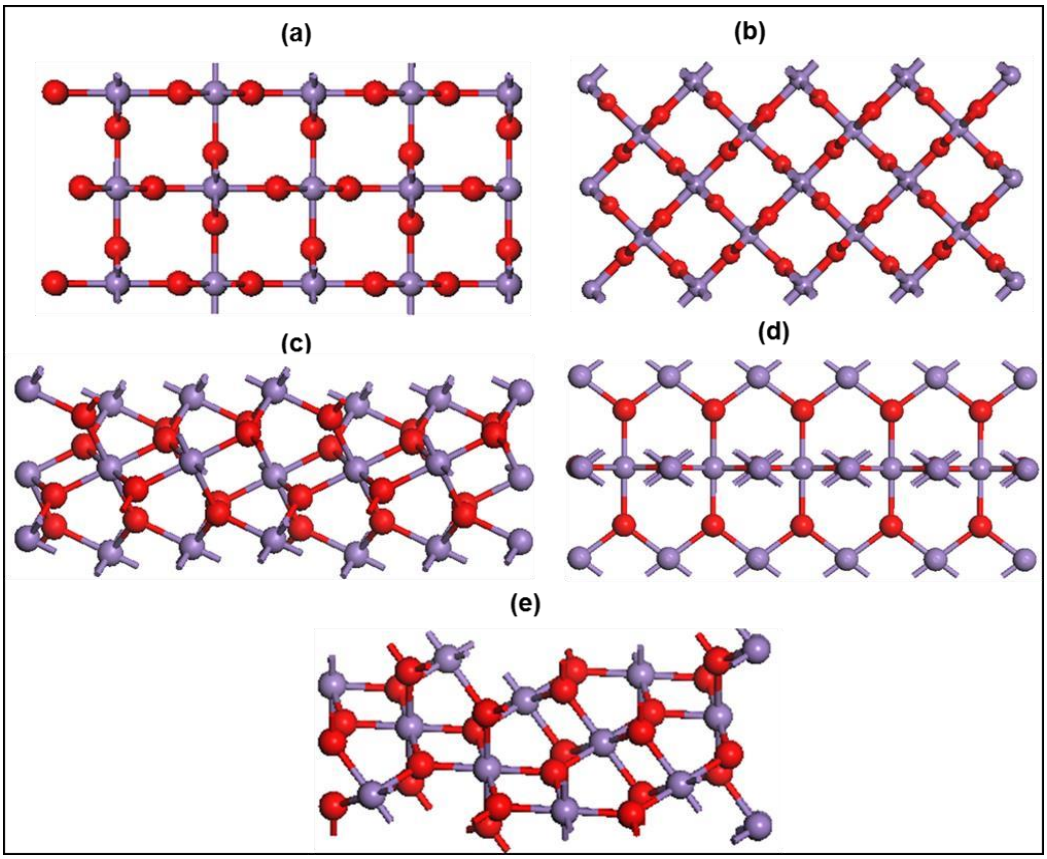

Figure 1.4: The β-MO_2 surfaces (a) (110), (b) (100), (c) (101), (d) (001), (e) (111) concurring to their steadiness trend, red particles are the oxygen, and the purple molecules are the manganese.

The (110) surfaces of TiO_2 are generally steady under certain conditions; the surfaces that form a peroxo group are steady compared to the unsteady titanyl group. Adsorption moreover occurs primarily within the form of the mononuclear peroxo species where oxygen bonds with one Ti cation. This configuration also has a point at which oxygen particles prefer to orientate themselves on the surface of TiO_2. The oxygen adsorption of TiO_2 has been thoroughly studied. The adsorption energies obtained are positive, consequently recommending that the reaction is nonspontaneous, and energy is required for oxygen particles to adsorb on the surface. For the oxidizing conditions, the surfaces are unstable and have a positive vacancy formation.

The VO_2 (110) surface can be anticipated to be oxidized under surrounding conditions, and even beneath emphatically reducing conditions, with an abundance of oxygen forming surface vanadyl groups [30]. Peroxo species are comparatively much less stable. However, reduction of surfaces is thermodynamically exceptionally unfavourable, and oxygen vacancies are less demanding to form within the bulk than on the surface. VO_2 surface will be steady against oxidation for oxygen chemical potential within the locale where the bulk VO_2 is steady. However, it is found that much of the surface abundance of oxygen can survive these exceptionally reducing conditions [30].

As in rutile TiO_2, the oxygen-terminated (110) surface is the strongest in rutile VO_2. The surface relaxation patterns also are very comparable in each oxide, as it is the order of balance of different low-index surfaces. The equilibrium morphology of VO_2(R) has been discovered to be acicular, laterally restricted by the (110) planes. The application of a correction to the over the binding of the oxygen molecule in the GGA approximation is discovered to have a big impact on the prediction of the surface composition under reducing conditions. The uncorrected effects imply that the VO_2 surface can be stable towards oxidation for oxygen chemical potentials in the area in which bulk VO_2 is stable [30]. However, after making use of corrections to the oxygen molecule energy, it is discovered that much of the surface excess oxygen can continue to exist in these very reducing conditions.

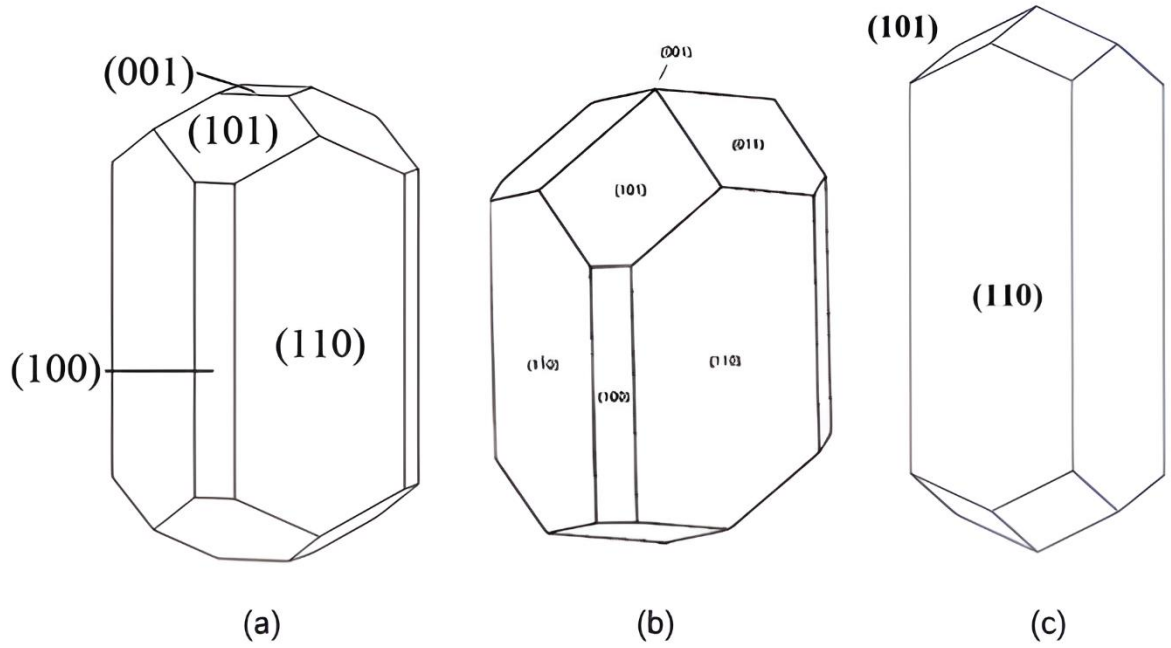

Figure 1. 5 Wulff's equilibrium morphology for (a) MnO_2, TiO_2, and (c) VO_2.

The morphology calculations were performed using metadise code (Minimum Energy Technique Applied to Dislocations, Interfaces, and Surfaces Energies) [14]. The code has its minimal energy optimizer primarily based totally upon interatomic potentials or is properly included to apply minimal energies calculated by external programs e.g., using the Density Functional Theory codes. The morphologies of the systems are dependent on the synthesis conditions, but the observed tendency to form particles with a large aspect ratio is consistent with the results obtained [16].

The surface plane of fivefold Mn atoms finally ends up being ~0.30 Å beneath the plane of sixfold Mn atoms. This is again just like the relaxed TiO_2 (110) surface, wherein the equal distance is 0.44 Å, according to low-energy electron diffraction experiments (and 0.39-0.42 Å in theoretical calculations, relying on the method) [16].

1.3.3. Catalyst in metal-air batteries

Metal-air batteries are considered the most promising future the batteries, owing to their high theoretical specific energy compared to the present frame of batteries such as the Li-ion. The Li-air battery changes over the chemical energy in lithium (anode) and oxygen (cathode) into electric energy amid discharge and its arrangements of electric energy by the portion Li-O_2 discharge products amid charge utilizing electricity [17]. These Li-air batteries contrast from the rest of the batteries in a way that the cathode dynamic material is oxygen is not stored within the battery.

The most recognizing highlight of this advancement is that it takes advantage of reversible transformation reactions of O_2 or other air components (such as N_2 or CO_2) at the cathode. To advance these reactions, catalysts are regularly required. A few materials such as platinum (Pt) and iridium oxide (IrO) have been examined for this reason. The role played by catalysts in metal-air battery frameworks and the dialogs on the Li-O_2 batteries as they are the most escalation considered within the literature. In this context, catalysts appeared to be compelling to encourage the oxygen (O_2) reduction responses and/or O_2 advancement reactions. The overall cell execution as measured by the round-trip efficiencies and charge/discharge rates can be essentially progressed by the consolidation of catalysts.

However, the presence of catalysts is additionally found to complicate the chemical reactions as they frequently show activities toward parasitic chemical reactions such as electrolyte and electrode disintegrations. The issue is particularly intense in aprotic Li-O_2 batteries, where organic electrolytes and receptive O_2 species are mixed. In expansion to heterogeneous catalysts, moreover, the discussions of the parts played

by homogeneous catalysts as redox mediators, which are viable to advance redox reactions that are basic to energy storage applications.

Upon battery discharge, the oxygen from the environment scatters into the air electrode and is reduced at the surface within the air cathode, which results in building up the peroxide or oxide particle that advance reacts with cationic species within the electrolyte [18]. Figure 1.6 illustrate the process of charging and discharging demonstrating how the products mentioned over are shaped in a nonaqueous electrolyte.

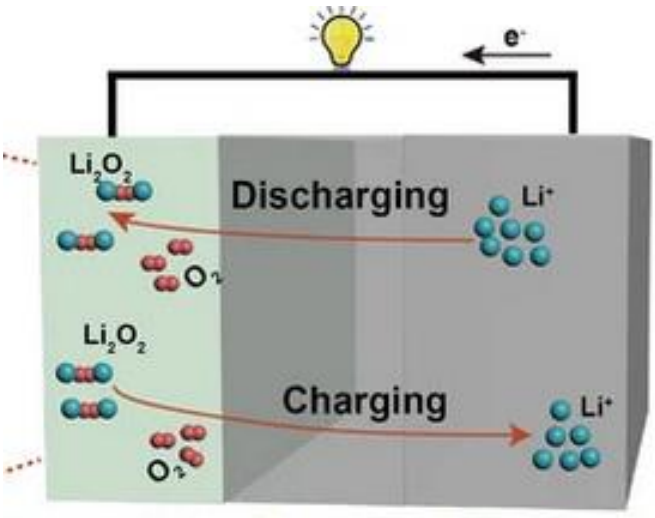

Figure 1.6: Schematic representation of Li-air battery appearing the charge and discharge cycles.

Subsequently, there are two sorts of Li-air batteries examined, the nonaqueous and aqueous electrolyte frameworks. Underneath are the two discharge reactions based on the nonaqueous Li/air battery:

$Li + O_2 \leftrightarrow Li_2O_2$; ($E^o = 3.10V$)……...1.1

$4Li + O_2 \leftrightarrow 2Li_2O$; ($E^o = 2.91V$)……1.2

The voltages of both the reversible reactions (1.1) and (1.2) are 3.10 and 2.91 V, respectively. Furthermore, water molecules are included in an aqueous electrolyte

based on the reaction underneath which comprise of voltage of almost 3.48 V in neutral solution:

$4Li + 6H_2O + O_2 \leftrightarrow 4(LiOH{\cdot}H_2O)$……1.3

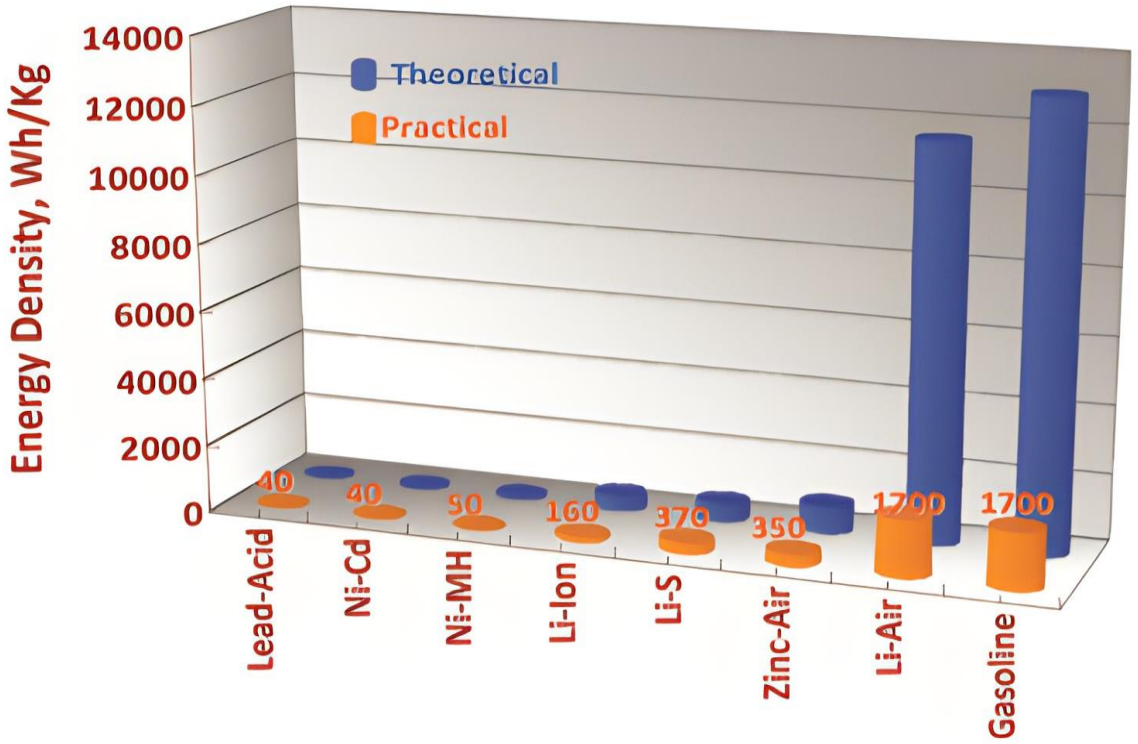

Figure 1.7: The energy densities (Wh/kg) for sorts of rechargeable batteries, the theoretical thickness is shown as blue bars although the viable density is inferred by the orange blocks.

Looking at figure 1.7 shows how gasoline employment viable energy density for car applications for around 1700 Wh/kg, which is the same for Li-air. Assessing the later Li-ion with the theoretical Li-air battery, a massive contrast in energy density (Wh/kg) is noticed whereby the execution of the two batteries will not be the same. When observing the theoretical energy density of Li-air and gasoline, a modern vision pointed to progress of the Li-air since its theoretical density is far way better than the Li-air density. The theoretical densities for both gasoline and Li-air are roughly 13 000 Wh/kg

and 11 000 Wh/kg, respectively. Where the current batteries have lesser theoretical density compared to Li-air batteries.

The Li-ion batteries have an energy density of generally 100 and 200 Wh/kg which is 10-fold less than both the Li-air and gasoline. The innovative chemistry of batteries needs to be applied to achieve or improve the existing batteries like Li-ion to be closer to the target of 1700 Wh/kg. Metal-air batteries such as Zn/air, as a rule, have a practical energy density of around 45-50% of their theoretical density.

In a nonaqueous Na-air battery, the Na^+ generated from a metal, sodium anode would react with O^{2-} or O_2^{2-} at the air cathode through an electrolyte to create NaO_2 or Na_2O_2 during the discharge process [19] [20]. These insoluble discharge products of NaO_2 or Na_2O_2 deposit onto their air cathode and block the dissemination pathway of oxygen to active sites, leading to the degradation of the execution of the Na-air battery [21]. The cycling execution of the Na-air battery was found to be subordinate to discharge products. The Na-air battery appeared or maybe great reversibility of more than 50 cycles and greatly poor reversibility of fewer than 10 cycles when NaO_2 and Na_2O_2 were shaped as discharge products, respectively [21].

It is well known that Na-air has a lower energy density compared to Li-air batteries, in this way the impact of a catalyst within the formation of NaO_2 [22]. The known products found during discharge in Na-air batteries are shown in the equations below:

$Na + O_2 \rightarrow NaO_2$ ($E^o = 2.27V$),……1.4

$Na + O_2 \rightarrow Na_2O_2$ ($E^o = 2.33V$),……..1.5

Alternately, in a Na-air, the formation of NaO_2 amid discharge matches with Na_2O_2 possessing their near-equilibrium potentials (2.27 V and 2.33 V), individually. It was concluded from the computation that Na_2O_2 may be a stable bulk phase, though NaO_2 is more stable at the nanoscale [23]. Although both the peroxide [19] and superoxide [24] have been detailed as the discharge products of a Na-O_2 cell, which of these is favoured is not understood.

1.3.4. Background of the calculated properties

Elastic properties

In materials science, any of various numbers quantify the response of a material to elastic or springy deflection. When tensile stress is applied to a material, the resulting strain is determined by Young's modulus, a constant defined as the ratio of the stress in a body to the corresponding strain. ab initio calculations for the determination of elastic constants are more complex than the calculations of bulk properties (i.e., lattice constants, heats of formation, etc.). The application of strain on the lattice implies a lowering of symmetry from that of bulk crystal and the strain energy involved is small. Elastic properties are imperative since they relate to different basics of solid-state properties, comprehensive the condition of the state, phonon spectra, and numerous others [25].

The bulk modulus is likewise one of the most essential parameters that signify the physical assets of a material system because it also measures the degree of stiffness or the power required to provide a given quantity of deformation, while the shear modulus describes the resistance to shape exchange due to shearing pressure; younger’s modulus displays the resistance of materials against uniaxial tensions.

Phonon dispersion

Phonon dispersion curves have an imperative role in various physical properties of condensed matter physics. Those comprise thermal conductivity, mechanical steadiness, and electrical conductivity. They suggest an excited state within the quantum mechanical quantization of the modes of vibrations of elastic frameworks of interacting particles. The behaviour of phonon dispersion branches displays functions of the crystal shape and the interatomic interactions and, consequently, offers the most complete and specific data approximately the dynamical properties of crystals. The phonon vibration frequencies are calculated as follows [26] [27]:

$$\omega = \upsilon_s q \quad \text{.....1.6}$$

Where υ is the speed and q is the wave-vector of the lattice vibrations. In a crystal in which there are two or more kinds of atoms; two forms of modes of vibrations are displayed: acoustic and optical. Optical phonons rise from out of phase vibrations among neighbouring atoms within the unit cell, even as in phase vibrations provide an upward push to acoustic phonons. Moreover, the acoustic modes have zero frequencies at $q = 0$ (the centre of the Brillouin zone, Γ), at the same time as the optical modes have non-zero.

The acoustic and optical break up into longitudinal and transverse modes abbreviated as longitudinal acoustic (LA), transverse acoustic (TA), longitudinal optical (LO), and transverse optical (TO). A linear relationship among frequency and long wavelengths phonon wave-vector is displayed within the acoustic modes. negative vibrational frequencies (soft modes) suggest mechanical instability of the framework, whilst positive vibrations display stability.

Electronic properties

The density of states (DOS) refers to the number of states which are available for occupation through electrons. The DOS offers numerical information on the states of availability at every energy stage. An excessive value for the density of states represents a better probability for the energetic states to be occupied. Energy levels in a crystalline may be broken up into multiple levels separated through their atomic interactions. Because of interatomic coupling, a crystal forms a single electronic framework obeying Pauli's exclusion principle.

Materials are categorized into three major corporations: metals, semiconductors, and insulators. Those classifications are distinguished via the presence and size of the energy gaps among the two highest energy bands specifically: the conduction band and the valence band. The energy gap (E_g) refers to a forbidden area between the most valence energy band (E_v) and the minimal conduction energy band (E_c). The boundary between the occupied states and the unoccupied states is referred to as the Fermi energy [28]. Information that occurs at the Fermi stage and the ensuing energy band gaps is very essential to infer the steadiness of the nanoclusters and the contributions of their atoms. The shift of the Fermi level (E_F) concerning the bandgap performs a crucial role in instability and alternate coordination in the framework.

1.4. Intentions of the study

Lithium-ion rechargeable batteries appear to be everywhere-they give control for most convenient electronics, an increasing extent of hand devices, as well as the advanced sorts of Battery electric powered automobiles (BEVs). MnO_2 recrystallizes into numerous crystallographic structures, including α, β, γ, δ, and λ structures. These frameworks depend on the way the MnO_6 octahedra are connected and have tunnels or interlayers with holes of different sizes.

Within all the polymorphs that the MnO_2 system possesses, the β-MnO_2 phase is selected since there are many setbacks concerning the lithium intercalation into β-MnO_2 such as capacity loss due to undesirable structural phase transformation into spinel like $LixMn_2O_4$. One of the fundamental appeals is to adjust and enhance the ultimate stability of β-MnO_2 to anticipate phase change amid lithium intercalation and rapid capacity fading throughout cycling. The Density functional tight-binding (DFTB) will be employed to derive the potentials for MnO_2, and the lattice parameters obtained from the derived potentials will be compared to the lattice parameters from the experiments and the density functional theory (DFT).

The DFTB will be used for the derivation of MnO_2 potentials to deal with the difficulty of computing time which is more intensive when shifting from bulk to surface study of MnO_2. The DFTB handles more atoms than the conventional DFT. When exploring the surface studies of MnO_2, it will be an advantage to applying the DFTB approach to not be time-consuming. The DFTB permits the introduction of temperature to the system which is not viable with the DFT approach. The potential derivation will take time since we begin with trial and error however, once the potentials are derived well, the calculations such as surface study, surface coating, and doping emerge as pleasant to the approach. The TiO_2 potentials had been studied by [29]. The VO_2 potential derivation is fundamental in the future.

Furthermore, we will examine the structural and electronic properties of MnO_2 using the potentials obtained from the DFTB. The structural properties such as lattice parameters and atoms position will be compared with the ones attained experimentally and using the DFT technique. To validate the potentials obtained, the electronic properties such as the electronic band structures and density of states (DOS) will be investigated to check the conductivity of the system and how the system behaves

towards the Fermi level. These discoveries will be imperative in protecting the crystal shape of $LiMnO_2$ and the maintenance of capacity amid cycling.

Additionally, we will be investigating the mechanical and the electronic properties of (110) MO_2 surfaces using the traditional DFT, where M symbolises Mn, Ti, and V using the DFT technique. The elastic properties and the phonon dispersion will be investigated to check the mechanical stability through the criteria provided for different systems and to compare the stability of the systems through the interaction within the gamma region, respectively. The electronic properties such as the electronic band structures and (DOS) will be investigated to check the conductivity of the system and how the system behaves toward the Fermi level

Lithium-air (Li-O_2) batteries have been increasingly studied because they exhibit the highest energy density among battery technologies. One of the essential problems for Li-air batteries is that the advanced catalysts exhibit gradual activity for both oxygen reduction reaction (ORR) and oxygen evolution reaction (OER). The adsorption of metal (Li/Na) and oxygen on (110) β-MO_2 is studied in a previous study [30], which is vital in the charge and discharge of Li/Na-air batteries. The mentioned study provides a better understanding of the catalytic activity of MO_2 for the oxygen reduction reaction (ORR) and oxygen evolution reaction from both the Li-air and Na-air batteries. Upon oxygen adsorption at the Li/MO_2, and at the Na/MO_2 several configurations such as dissociated, peroxo on Li, peroxo on M, peroxo on Li-M and dissociated, peroxo on M, peroxo on Na, peroxo on Na-M were obtained, respectively. From the configurations, electronic properties such as the electronic band structures and the density of states will be calculated to check the conductivity of the frameworks and to compare their stability of them to the Fermi level.

1.5. Outline of the study

In the current study, the density functional based tight-binding method and density functional plane-wave pseudopotential technique will also be applied to regulate the structural and electronic properties.

Chapter 1 introduces general knowledge of batteries and literature on lithium-ion, lithium-air, and sodium-air batteries. Furthermore, the outline of the study is also presented.

Chapter 2 theories behind the techniques used are explained in components, the density functional theory (DFT), and the density functional based tight-binding (DFTB) method.

Chapter 3 we derive Mn-O potentials using DFTB+ parameterization, we use parameters derived to investigate the structural and electronic properties of β-MnO_2.

Chapter 4 gives a detailed discussion on MO_2 clean (110) surfaces and oxygen adsorption at the Li/MO_2. The mechanical properties such as elastic properties and phonon dispersions for MO_2 (110) clean surfaces were determined. The electronic properties were determined for both the MO_2 clean surfaces and oxygen adsorbed Li/MO_2.

Chapter 5 gives a detailed discussion of the oxygen adsorption at the Na/MO_2 (110) surfaces. The electronic properties were determined for oxygen adsorbed Na/MO_2 (110) surfaces.

Chapter 2: Computational methods

2.1 Introduction

This chapter outlines the method of calculations employed in the study. We used two techniques, namely: density functional theory (DFT) and density functional tight binding (DFTB). The tight-binding (TB) quantum mechanical simulation method implemented in DFTB+ has been used to develop the set of parameters for β-MnO_2. DFT is widely used to study the properties of various materials such as MnO_2, VO_2, TiO_2, and adsorbed surfaces of the metal oxides. The CASTEP code is employed to deal with weak pseudo-potentials. Above all, the DFT and DFTB techniques can simulate electronic relaxation to ground states for metals, insulators, or semiconductors.

2.2 Density functional theory

Density functional theory is based on communicating the entire energy of a framework as a work of the entire electron density [31]. It was created by Hohenberg and Kohn in 1964 Thomas and Fermi [32], demonstrated that the complete ground-state energy of the many-electron system could be a work of the electron thickness ρ(r),

$$E = E[\rho(r)] \quad \text{.....2.1}$$

Utilizing two hypotheses (Kohn-Hohenberg hypotheses): the primary hypothesis sets the basis for decreasing many-body systems using the electron thickness and the moment hypothesis clarifies vitality useful for the system and confirms that the proper ground-state electron decreases this energy useful [7]. This empowered Kohn and Pretence to determine the conditions from the Hohenberg-Kohn hypothesis which appears to the plausibility of utilizing the ground-state density to calculate the

properties of the system [33]. The condition gives the course to discover the ground state thickness, which are compelling one-electron Schrodinger conditions inferred by, to begin with comparing the useful as the entirety of three terms composed as:

$$E[\rho] = T_o[\rho] + U[\rho] + E_{xc}[\rho], \quad \text{2.2}$$

where T_o is the kinetic energy of the non-interacting electrons, $U[\rho]$ representing the coulomb energy containing the electrostatic energy rising from the Coulomb attraction between electrons and nuclei E_{xc} being the exchange-correlation work. These effective one-electron Schrödinger conditions are known as the Kohn-Sham conditions, given by:

$$\left[-\frac{\hbar^2}{2m}\nabla^2 + V_{eff}(\boldsymbol{r})\right]\psi_i(\boldsymbol{r}) = \epsilon_i\psi_i, \quad \text{2.3}$$

where $V_{eff}(\boldsymbol{r})$ is the compelling potential composed as:

$$V_{eff}(\boldsymbol{r}) = \nu(\boldsymbol{r}) + \int \frac{\rho(r')}{|r-r'|}d\boldsymbol{r'} + \nu_{\boldsymbol{xc}}(\boldsymbol{r}), \quad \text{2.4}$$

and

$$\nu_{\boldsymbol{xc}}(\boldsymbol{r}) = \frac{\boldsymbol{\delta E_{xc}}}{\boldsymbol{\delta\rho(r)}} \quad \text{2.5}$$

Therefore, the Kohn-Sham total energy functional is written as:

$$E = \Sigma\epsilon_i - \frac{e^2}{2}\iint \frac{\rho(\boldsymbol{r})\rho(\boldsymbol{r'})}{|r-\boldsymbol{r'}|}d\boldsymbol{r}d\boldsymbol{r'} + E_{xc}[\rho(\boldsymbol{r})] - \int \rho(\boldsymbol{r})v_{xc}d\boldsymbol{r} \quad \text{2.6}$$

In any case, the precise work for trade and correlation energy (E_{xc}) is not known but for the free electron gas. There are commonly utilized approximations that concur to achieve DFT calculations: nearby density approximation (LDA) and generalized angle

guess (GGA). DFT at that point progressed as the foremost imperative first-principle quantum mechanical approach generally within the solid-state material science and has been as of late utilized in condensed matter considers as a strategy for calculating the quantum mechanical ground states of frameworks [34] [35].

2.3 Approximation methods

2.3.1. Local density approximation (LDA)

Local density approximations (LDA) are class of approximations to the exchange-correlation (XC) energy functional in the density functional theory (DFT) that are determined by the electronic density at each point in space. The local density approximation (LDA) states that, for regions of a material where the charge density is slowly varying, the exchange-correlation energy at that point can be considered the same as that for a locally uniform electron gas of the same charge density. This is the most widely used approximation, which locally substitutes the exchange-correlation energy density of an inhomogeneous system with that of an electron gas evaluated at local density. LDA rests upon two basic assumptions: the first being that the exchange and correlation effects come predominantly from the immediate vicinity of the point r and the second being that these exchange and correlation effects do not depend strongly on the variations of the electron density in the vicinity of r [36]. The fulfilment of these two conditions results the same contribution from the volume element dr as if this volume element were surrounded by a constant electron density $\rho(r)$ of the same value as within dr. In this approximation, the exchange-correlation energy density of the homogeneous electron gas $E_{XC}^{\text{hom}}(\rho_0)$ is dependent on the homogeneous density ρ_0 and replaces this for the inhomogeneous system with density $\rho(r)$ by

$$E_{XC}^{LDA}(\rho(r)) = E_{XC}^{\text{hom}}(\rho_0)|_{\rho_0} = \rho(r) \quad \text{.....2.7}$$

For a spin-unpolarized system (where the function depends only on the density) a local density approximation for the exchange-correlation energy is written as

$$E_{XC}^{LDA}[\rho] = \int p(r)\varepsilon_{XC}(\rho)dr \quad \text{.....2.8}$$

and

$$\frac{\delta E_{XC}(\rho(r))}{\delta\rho(r)} = \frac{\partial[\rho(r)\varepsilon_{XC}(r)]}{\partial\rho(r)} \quad \text{.....2.9}$$

where ρ is the electronic density and E_{XC} the exchange-correlation energy density.

This approximation does only work for systems with slowly varying densities, such as the weakly perturbed electron gas, but however, the approximation works well even for systems which have very inhomogeneous electron densities such as atoms and molecules. When considering the xc-hole and the pair correlation function, we get a more detailed look at LDA

$$\rho_{Xc}^{LDA}(r_1, r_2) = \rho(r_1)[g^{\text{hom}}([\rho];|r_1 - r_2|], \quad \text{.....2.10}$$

where $g^{\text{hom}}[\rho]$ is the coupling constant integrated pair-correlation function of the homogeneous electron gas [37]. The exchange-correlation part of the pair-correlation function which is unaffected by the coupling constant integration is given by

$$g_{xc}^{LDA}([\rho];r_1,r_2) = 1 - \frac{9}{2}\left[\frac{\sin(k_F(r_1)|r_1 - r_2|) - k_F(r_1)|r_1 - r_2|\cos(k_F(r_1)|r_1 - r_2|)}{(k_F(r_1)|r_1 - r_2|)^3}\right]^2 \quad \text{,...2.11}$$

where $k_F(r)$ is the local Fermi wave vector defined as.

$$k_F(r) = \left(\frac{3}{\pi}\right)^{\frac{1}{3}} \rho(r)^{\frac{1}{3}}$$,……2.12

The exchange-correlation energy is decomposed into exchange and correlation terms linearly

$$E_{XC} = E_x + E_c$$,……2.13

So that separate expressions for E_x and E_c are sought. The exchange term takes on an analytic form for the homogeneous electron gas (HEG). The exchange-energy density of a HEG is known analytically. The LDA for exchange employs this expression under the approximation that the exchange-energy in a system where the density in not homogeneous, is obtained by applying the HEG results pointwise, yielding the expression [38, 39].

$$E_x^{LDA}[\rho] = -\frac{3}{4}\left(\frac{3}{\pi}\right)^{\frac{1}{3}} \int \rho(r)^{\frac{4}{3}} dr.$$ ……..2.14

This equation satisfies the correct exchange scaling. There are corresponding equations for the correlation part of $g^{\text{hom}}[\rho]$ and for $E_C^{LDA}[\rho]$. The LDA xc-hole is spherical around the reference electron

$$\rho_{XC}^{LDA}(r_1, r_2) = \rho_{XC}(r_1, s)$$,……2.15

Where $s = | r_1 - r_2 |$ and it also satisfy the sum rule

$$\int \rho_{XC}^{LDA}(r_1, r_2) dr_2 = 4r \int_0^{\infty} \rho_{XC}^{LDA}(r_1, s) s^2 ds = -1$$,……2.16

Analytic expressions for the correlation energy of the HEG are not known except in the high-density and low-density limits corresponding to infinitely weak and infinitely strong correlation [38]. For a HEG with density ρ, the high-density limit of the correlation energy density is

$$\varepsilon_c = A\ln(r_s) + B + r_s(C\ln(r_s) + D) \quad \text{.....2.17}$$

And the low limit

$$\varepsilon_c = \frac{1}{2}\left(\frac{g_0}{r_s} + \frac{g_1}{r_s^{\frac{3}{2}}} + ...\right) \quad \text{.....2.18}$$

where the Wigner-Seitz radius is related to the density as.

$$\frac{4}{3}\pi r_s^3 = \frac{1}{\rho} \quad \text{.....2.19}$$

Local-density approximations are important in the construction of more sophisticated approximations to the exchange-correlation energy, such as generalized gradient approximations or hybrid functionals, as a desirable property of any approximate exchange-correlation functional is that it reproduces the exact results of the homogeneous electron gas (HEG) for non-varying densities. As such, LDAs are often an explicit component of such functionals.

2.3.2. Generalized gradient approximation (GGA)

Generalized angle guess could be a well-known work presented by Perdew and Wang [40], it was presented as an enhancement to LDA. The gradients' degree changes within the electron thickness and are utilized to progress the local density approximation. The theory of most gradient useful improvement is based upon the shifting electron gas [41]. The approximations are called Gradient Expansion Approximation (GEA), which can be written as:

$$E_x^{GEA}[\rho] = E_x^{LDA}[\rho] + \beta \int \frac{(\nabla\rho)^2}{\rho^{\frac{4}{3}}} dr + \cdots \quad \text{.....2.20}$$

$$E_c^{GEA}[\rho] = E_c^{LDA}[\rho] + \int C(\rho) \frac{(\nabla\rho)^2}{\rho^{\frac{4}{3}}} dr + \cdots, \quad \text{.....2.21}$$

where β is a constant and $C(\rho)$ is a function determined by response theory Conversely, the GEA provides no enhancement over the LDA as flexible densities in molecules and atoms don't fluctuate gradually over space. The investigation of the gradient extension of the xc-hole is done, they assign that the short-range portion (close to the reference electron) is upgraded, but the long-range is made more awful [42].

The two vital variations of GGA are distinguished as the ‘parameter free’ (parameters are decided from known coefficients) and experimental (parameters decided from fits to test information or calculated nuclear properties) [34]. For example, the PBE [43], and PW91 [44] are commonly utilized in material science, and reexamined forms of PBE both revPBE [45] as well as rPBE [45] are primarily utilized in catalysis [46] and are called ‘parameter free’ [34], whereas BLYP [34] is observational and commonly used in chemistry [34]. In this study, the GGA PBE functional will be used to optimize β-MnO_2, metal oxides (MO_2), and adsorbed surfaces of the metal oxides systems for accurate parameters to this material.

2.4 Tight binding

The tight binding is an electronic structure method generally utilized in solid-state physics for numerous structures including transition metals. The method is closely related to the direct combination of nuclear orbital (LCAO) strategy, where the development of eigenstates of a Hamiltonian within the orthogonalized premise of the atom-like orbitals signifies the exact many-body Hamilton administrator with a

parameterized Hamiltonian lattice with network components fitted to the band structure of the reference system.

The tight-binding method advantage is that the electron of a system is emphatically bounded so that, when the molecule is set in a crystal the cover of the nuclear wave is less. The Hamiltonian of the system is amplified by:

$$H(r) = \sum_{Rn} H_{at}(r - R_n) + \Delta U(r) \quad \text{.....2.22}$$

The Hamiltonian work of a single confined molecule and the arrangement to the time-independent single electron is represented with (H_{at}) , Schrödinger's equation is approximated as:

$$\psi(r) = \sum_{m,Rn} b_n(R_n)\psi_m(r - R_n), \quad \text{.....2.23}$$

where m is the m^{th}atomic energy level and R_n being the location of an atomic site of the crystal lattice.

2.4.1. DFT as Basis for a tight-binding Method

Taking after Fouilkes and Haydock [47] the electronic density is composed of a reference density ρ_o plus a small variance $\delta\rho$,

$$\rho(\vec{r}) = \rho_o(\vec{r}) + \delta\rho(\vec{r}) \quad \text{.....2.24}$$

This electronic equation is at that point embedded within Kohn-Sham (KS) strategy given by:

$$E[\rho] = \sum_i^M n_i \left\langle \psi_i \middle| -\frac{1}{2}\nabla_i^2 + v_{ext}(\vec{r}) + \frac{1}{2}\int \frac{\rho(\vec{r\prime})}{|\vec{r} - \vec{r\prime}|} d\vec{r}' \middle| \psi_i \right\rangle + E_{xc}[\rho] + \frac{1}{2}\sum_\beta^N \sum_{\propto \neq \beta}^N \frac{Z_\alpha Z_\beta}{|\hat{R}_\propto \hat{R}_\beta|} \quad \text{.....2.25}$$

Thus,

$$E[\rho_o + \delta\rho] = \left\langle \psi_i \middle| -\frac{1}{2}\nabla_i^2 + v_{ext}(\vec{r}) + \int \frac{\rho_o'}{|\vec{r} - \vec{r}'|} d\vec{r}' + v_{ext}[\rho_o] \middle| \psi_i \right\rangle$$

$$-\frac{1}{2}\iint \frac{\rho_o'[\rho_o + \delta\rho}{|\vec{r} - \vec{r}'|} d\vec{r} d\vec{r}'$$

$$-\int v_{ext}[\rho_o](\rho_o + \delta\rho)d\vec{r} + \frac{1}{2}\iint \frac{\rho_o'[\rho_o+\delta\rho]}{|\vec{r}-\vec{r}\prime|} d\vec{r} d\vec{r}' + E_{xc}[\rho_o + \delta\rho] + E_{nn}, \ldots 2.26$$

where $\rho_o' = \rho_o(r)$ and $\delta\rho' = \delta\rho(\vec{r}')$ are characterized as short-hand documentations, the second term in equation (2.13) amends the double counting in the coulomb term; the third term rectifies the new exchange-correlation contribution, and the fourth term results from splitting the coulomb energy into one part related to ρ_o and another related to $\delta\rho$. E_{nn} is the nuclear repulsion. Afterward, $E_{xc}[\rho_o + \delta\rho]$ expand in Taylor arrangement up to the second-order term:

$$E_{xc}[\rho_o + \delta\rho] = E_{xc}[\rho_o] + \int \frac{\delta E_{xc}}{\delta\rho} \left|\delta\rho d\vec{r} + \frac{1}{2}\iint \frac{\delta^2 E_{xc}}{\delta\rho\delta\rho'}\right| \delta\rho\delta\rho' d\vec{r} d\vec{r}' \ldots\ldots\ldots\ldots\ldots\ldots\ldots\ldots 2.27$$

$$E = \sum_i^M n_i \left\langle \psi_i \middle| -\tfrac{1}{2}\nabla^2 + v_{ext}(\vec{r}) + \int \frac{\rho_o'}{|\vec{r}-\vec{r}\prime|} d\vec{r}' + v_{ext}[\rho_o] \middle| \psi_i \right\rangle.$$

Substitution of equation (2.14) into (2.13) and use of the definition $\left(\frac{\delta E_{xc}}{\delta\rho}\right)_{\rho_o} = V_{xc}[\rho_o]$ results in:

$$-\frac{1}{2}\iint \frac{\rho_o'[\rho_o+\delta\rho}{|\vec{r}-\vec{r}\prime|} d\vec{r} d\vec{r}' + E_{xc}[\rho_o] - \int v_{ext}[\rho_o]\rho_o d\vec{r}$$

$$+E_{nn} + \frac{1}{2}\iint \left(\frac{\delta\rho_o\delta\rho}{|\vec{r}-\vec{r}\prime|} + \frac{\delta^2 E_{xc}}{\delta\rho\delta\rho'}\right) d\vec{r} d\vec{r}' \ldots\ldots\ldots\ldots\ldots\ldots\ldots\ldots\ldots\ldots\ldots\ldots\ldots\ldots 2.28$$

From equation (2.15) it is conceivable to characterize four imperative terms. The primary is a reference Hamiltonian $\widehat{H}^o$ depending only upon ρ_o at that point:

$$\widehat{H}^{o} = -\frac{1}{2}\nabla^2 + V_{xc}(\vec{r}) + \int \frac{\rho_o'}{|\vec{r}-\vec{r}\prime|} d\vec{r}' + V_{xc}[\rho_o] \quad \text{.....2.29}$$

The sum in the first line of equation (2.15) is analog to E_{bs} from $E = E_{bs}E_{rep}$. The terms in the second line equation (2.15) define the repulsion contribution:

$$E_{rep}[\rho_o] = -\frac{1}{2}\iint \left(\frac{\delta\rho_o\delta\rho}{|\vec{r}-\vec{r}\prime|} d\vec{r}d\vec{r}' + E_{xc}[\rho_o] - \int V_{xc}[\rho_o]\rho_o d\vec{r} + E_{nn} \quad \text{.....2.30}$$

Lastly, the term in equation (2.15) includes corrections related to the fluctuations in the electronic density. The term is defined as follows:

$$E_{2nd}[\rho_0, \delta\rho] = \frac{1}{2}\iint \left(\frac{\delta\rho\delta\rho'}{|\vec{r}-\vec{r}'|} + \frac{\delta^2 E_{xc}}{\delta\rho\delta\rho'}\Big|_{\rho_0}\right) d\vec{r}d\vec{r}' \quad \text{.....2.31}$$

Thereafter, equation (2.15) can be rewritten as:

$$E = \underbrace{\sum_i^M n_i \langle \psi_i | \widehat{H}^0 | \psi_i \rangle}_{E_{bs}} + E_{rep}[\rho_0] + E_{2nd}[\rho_0, \delta\rho] \quad \text{.....2.32}$$

To estimate a great reference electronic density ρ_o can be composed a superposition of atom-like densities centered on the nuclei $\propto$ as:

$$\rho_0(\vec{r}) = \sum_\alpha^N \rho_0^\alpha(\vec{r}_\alpha),\ \vec{r}_\alpha = \vec{r} - \vec{R}_\alpha \quad \text{.....2.33}$$

This approximation guaranteed that E_{rep} is free of the electronic density vacillations. In any case, the neutrality of $\rho_o^\propto$ the coulomb contributions become negligible for long distances. Where E_{rep} can be extended to:

$$E_{rep} = \sum_\propto^N E_{rep}[\rho_0^\alpha] + \frac{1}{2}\sum_\beta^N \sum_{\propto\neq\beta}^N \left(E_{rep}[\rho_0^\alpha] + \rho_0^\beta - E_{rep}[\rho_0^\alpha] - E_{rep}\left[\rho_0^\beta\right]\right) +$$

$$(interactions\ of\ 3\ and\ more\ centers) \quad \text{.....2.34}$$

The contributions can be neglected for three and more centers that are small. The approximations can be guarded by coulomb screening, for occasion, since ρ_0^{α} is the electronic density of unbiased atom, the electron-electron interaction terms with more than two centres are cancelled by the nucleus-nucleus intuitive.

Extraordinary screening of terms with more than two centers can be accepted that the two center commitments to be short ranged. However, there is no repulsion energy decay to zero for long interatomic separations. While it decays to the consistent esteem given by atomic commitments:

$$\lim_{R_{\propto\beta}\to\infty} E_{rep}\,[\rho_0] = \sum_{\propto}^{N} E_{rep}[\,\rho_0^{\alpha}] \qquad \text{2.35}$$

Thus, $\sum_{\propto}^{N} E_{rep}[\,\rho_0^{\alpha}]$ is expected to form E_{rep} subordinate as it were on two-centre commitments:

$$E_{rep}[\rho_0] \approx$$

$$\frac{1}{2}\sum_{\alpha,\beta}^{N} U[\rho_0^{\alpha}, \rho_0^{\beta}] \qquad \text{2.36}$$

It would be conceivable to calculate E_{rep} for known values of ρ_0^{α} it is more helpful to alter E_{rep} to ab initio outcomes. The E_{rep} fitted to the contrast between the DFT energy and E_{bs} as a function of interatomic distance $R_{\propto\beta}$ using an appropriate reference structure:

$$E_{rep}[\rho_0] \equiv E_{rep}\big(R_{\alpha\beta}\big) = \big\{E_{DFT}\big(R_{\alpha\beta}\big) - E_{bs}\big(R_{\alpha\beta}\big)\big\}\big|_{\text{ref. struct.}} \qquad \text{2.37}$$

The value of E_{bs} can be obtained by diagonalization of the Hamiltonian matrix, resulting into:

$$E_{bs} = \sum_{i=1}^{M} n_i \epsilon_i \qquad \text{2.38}$$

Value of E_{rep} is regularly fitted to a polynomial work or a series of splines. The discussed considerations make it possible to derive the DFTB model.

2.4.2. Density functional tight binding (DFTB)

Density functional tight binding is a technique that can perform calculations for larger systems containing up to 10 000 atoms The DFTB procedure combines the reliability of thickness functional theory with the computational proficiency of the tight-binding strategy to perform calculations and has been connected effectively to issues of different systems such as particles over clusters and undefined solids covering points counting surfaces and adsorbates [48]. The Taylor development of the Kohn-Sham density useful total energy around an appropriately chosen reference density $\rho(r)$ inferred the DFTB. The reference density ρ^o perturbed by a few thicknesses' fluctuation is accepted rather than finding the electron density that minimizes the energy. The $\rho(r)$ is represented by:

$$\rho(r) = \rho^o(r) + \delta\rho(r) \quad \text{.....2.39}$$

The standard DFTB method is fitting when the electron thickness of a structure with numerous particles to be spoken to as an entirety of atomic-like densities. To progress the overall energies, strengths, and transferability the DFTB strategy incorporates the efficient expansion of the tight-binding formalism to infer a generalized self-consistent-charge (SCC) methodology [49]. The self-consistent-charge density functional tight-binding (SCC-DFTB) method is regarded as an expansion of DFTB and is utilized to improve the depiction of the bonds for systems when adjustment of charges between sets of atoms is small [50]. The approximation method determined from density functional theory which is based on the second-order development of the Kohn-Sham total vitality concerning the charge thickness variances [51, 52] signified by:

$$E_{tot} = E_{BS} + E_{rep} + E_2(\rho, \Delta\rho) \quad \text{2.40}$$

The total energy E_{tot} incorporates electrostatic-interaction term $E_2(\rho, \Delta\rho)$ to the standard tight-binding Hamiltonian and the short-range repulsive two-particle interaction E_{rep} terms. The electrostatic-interaction accounting for the charge fluctuations is composed as:

$$E_2(\rho, \Delta\rho) = \frac{1}{2}\sum_{x,y}^{M} \gamma_{xy}\Delta q_x \Delta q_y \quad \text{2.41}$$

The Mulliken charges-based atomic charge fluctuation is represented by Δq_x and Δq_y with explanatory interpolating function γ_{xy}.

The improvement of Slater-Koster files which contain electronic parameters rearranges the utilize of DFTB since parameterization is the challenging portion when utilizing DFTB. Parameterizations comprise of the fitting of repulsive potentials within the E_{rep} in equation (2.27) and is communicated as:

$$E_{rep} = \sum_{i<j} V_{rep}^{ij}(R_{ij}) \quad \text{2.42}$$

where ij is a pair of atoms and $V_{rep}^{ij}(R)$ are the pair-wise repulsive functions depending only on the atomic numbers.

Transferability of repulsion possibilities requires the repulsion to be short-ranged and the cut-off radius R_{out} should be specified, the chosen cut-off radius is at that point utilized within the fitting of the, $V'_{rep}(R)$, the repulsion is then conveyed as:

$$V_{rep}(R) = -\int_{R}^{R_{cut}} V'_{rep}(r)dr \quad \text{2.43}$$

Transferability and quality of the inferred potentials are influenced by the cut-off radius quality of the fit, the band structure energy, electrostatic energy, and the reference structures utilized for parameterization process. The reference structure chosen for the parameterization should share in different fitted interactions such as changing coordination, diverse bond lengths and the significance of charge exchange to the system of intrigued, variety of charge exchange ought to be considered.

2.4.3. The standard DFTB model without self-consistency

The calculations for the entire energy do not depend on the electronic-density fluctuations, $\delta\rho$ since the second-order adjustment term of of E_{2nd} in equation (2.19) is ignored from the standard DFTB conspire. The Kohn-Sham orbitals are represented with a straight combination of atomic orbitals (LCAO) centered on the nuclei when using DFTB. However, the basis function is represented by Φ_v, the expansion coefficients by C_{iv}, the KS orbitals can be composed as:

$$\psi_i(\vec{r}) = \sum_v^N C_{iv}\ \Phi_v(\vec{r} - \vec{R}_\alpha), \quad \text{.....2.44}$$

from the LCAO model, the secular problem:

$$\sum_v^N C_{iv}\,(H_{\mu v}^o - \varepsilon_i S_{\mu v}) = 0, \quad \forall \mu, v \quad \text{.....2.45}$$

The elements of the Hamiltonian matrix given by,$H_{\mu v}^o$, the overlap matrix $S_{\mu v}$ denoted by:

$$H_{\mu v}^o = \langle \Phi_\mu | \widehat{H}^o | \Phi_v \rangle;\ S_{\mu v} = \langle \Phi_\mu | \Phi_v \rangle;\ \forall \mu\varepsilon\alpha, v\varepsilon\beta \quad \text{.....2.46}$$

From equation (2.19) the second term can be transformed with equation (2.31) and effective potential V_{KS} which is given by:

$$V_{KS}(\vec{r}) = v_{ext}(\vec{r}) + \frac{\delta J_s[\rho]}{\delta\rho(\vec{r})} + \frac{\delta E_{xc}[\rho]}{\delta\rho(\vec{r})}$$

$$= v_{ext}(\vec{r}) + \int \frac{\rho(\vec{r}')}{|\vec{r}-\vec{r}'|} d\vec{r}' + v_{xc}(\vec{r}) \quad \text{.....2.47}$$

Hence, equation (2.19) transforms into:

$$\sum_i^M n_i \langle \psi_i | \hat{H}^0 | \psi_i \rangle = \sum_i^M n_i \sum_{\mu,v}^N C_{i\mu} C_{iv} \langle \Phi_\mu | \hat{T} + v_{KS}[\rho_0] | \Phi_v) \rangle = \mathrm{tr}(P \cdot H^0) \quad \text{.....2.48}$$

The elements of the density matrix P can be defined as follows:

$$P_{\mu v} = \sum_i^M n_i C_{i\mu} C_{iv} \quad \text{.....2.49}$$

LCAO is confined as it were to valence orbitals since it is basic to guarantee the orthogonality of the fundamental capacities concerning to centre basis-functions of the extraordinary particles (by utilizing nuclear orbitals as essential capacities the orthogonality between the centre and valence capacities inside the same atom is as of now guaranteed).

$|\Phi\rangle$ is denoted as a non-orthogonalized basis-function and $|\Phi_c^\beta)$ as the core basis-function of atom β, the comparing orthogonalized basis-function of $|\Phi)$ is achieved by:

$$|\Phi_\mu\rangle = |\Phi_\mu\rangle - \sum_{\beta\neq\alpha} \sum_c |\Phi_c^\beta)(\Phi_c^\beta|\Phi_c), \ \mu, v \notin \alpha \quad \text{.....2.50}$$

Using orthogonalization procedure, equation (2.35) transforms into

$$\sum_i^M n_i \langle \psi_i | \hat{H}^0 | \psi_i \rangle = \sum_i^M n_i \sum_{\mu,v}^N C_{i\mu} C_{iv} \left(\Phi_\mu \left| \hat{T} + v_{KS} - \sum_\beta^N \sum_c \right| \Phi_c^\beta) \varepsilon_c^\beta (\Phi_c^\beta \right| \left| \Phi_v \right) \quad \mu, v \notin \{\beta\}, \quad \text{.....2.51}$$

where ε_c^{β} denotes the eigenvalue of the state c in atom β. The successful potential v_{KS} and the core correlation in equation (2.38) for which it can be translated as pseudo-potential (V_{pp}) writing v_{KS} as the sum of potentials $V_{\propto}$ centered on the particles,

$V_{KS[\rho_o]=\sum_{\alpha}^{N} V_{\alpha}(\vec{r}_a)}, \quad \vec{r}_a = \vec{r} - \vec{R}_a$.....2.52

Using the definition in equation (2.38), the viable potential is transformed into a pseudo-potential for all atoms within the framework, except for atoms which Φ_{μ} and Φ_{v} belong. Thus, pseudo-potential appears up in three-centre terms and within the two-centre terms whose valence orbitals have a place to the same particle (so-called crystal field terms). The pseudopotential commitments are altogether smaller than the commitments of the total possibilities and are:

$H_{\mu v}^{o} = \left(\Phi_{\mu}\left|-\frac{1}{2}\nabla_{v}^{2} + V_{\alpha} + (1-\delta_{\alpha\beta})V_{\beta}\right|\Phi_{v}\right), \ \mu\epsilon\{\alpha\}, v\epsilon\{\beta\},$.....2.53

wherever $\delta_{\alpha\beta}$ is the Kronecker's delta. The *potential superposition* approach has been used since the 1980s for the calculation of DFTB parameters. In 1998, Elstner *et al*. [49] displayed an elective approach to determine the DFTB conditions through a second-order development of the DFT add up to energy concerning to the electron thickness. As the result, the Hamiltonian lattice components are calculated as thickness superposition, which is indistinguishable to the condition (2.40) but for the commitment of the exchange-correlation potential. Certainly, due to the non-linear nature of v_{xc}, the successful potential cannot be portrayed as a basic entirety of reference possibilities inside this approach, instead one achieves.

$H_{\mu v}^{o} = \left(\Phi_{\mu}\left|-\frac{1}{2}\nabla_{v}^{2} + V_{KS}[\rho_o^{\alpha} - \rho_o^{\beta}\right|\Phi_{v}\right), \ \mu\epsilon\{\alpha\}, v\epsilon\{\beta\}$.....2.54

Both approaches are physically decided, and the comes about are comparable, which is not surprising in case the potential distinction between conditions (2.40) and (2.41) is calculated. Both methods have been used broadly in the past, the potential superposition being more prevalent for standard DFTB calculations, and the density superposition more widely used for SCC-DFTB.

The Φ_v basis functions and the reference atom-like densities ρ_o^α are attained by solving the Schrodinger equation.

$$\left[\hat{T} + V_{KS}[\rho_o^\alpha] + (\frac{r}{r_o})^2\right]\Phi_v(\vec{r}) = \epsilon_v\Phi_v(\vec{r}),\text{.....2.55}$$

for free atom within a self-consistent DFT strategy. The compression potential $(\frac{r}{r_o})^2$ in equation (2.42) constrains the wave functions, resulting in better basis sets for the study of condensed-phase systems and free molecules as well. The value for the parameter r_o is normally chosen between 1.85_{cov} and 2_{cov} with r_{cov} being the atomic covalent radius [48].

The Hamiltonian matrix components in practice, are calculated as follows: for the corner-to-corner components, the energy level of the free atom is chosen, which ensures precise separation limits. Due to the orthogonality of the essential capacities, the off-diagonal elements of the intra-atomic blocks are precisely zero. The interatomic pieces are computed as given in conditions (2.40) or (2.41), depending on the choice of potential era inside the density superposition approach the Hamiltonian lattice components uncover as:

$$H_{\mu v}^0 = \begin{cases} \varepsilon_\mu^{\text{free atom}}, & \mu = v \\ \left\langle \Phi_\mu \middle| \hat{T} + V_{KS}[\rho_0^\alpha - \rho_0^\beta] \middle| \Phi_v,\ \mu\epsilon\{\alpha\}, v\epsilon\{\beta\}, \alpha \neq \beta \right\rangle & \\ 0, & \text{otherwise} \end{cases} \text{.....2.56}$$

It is recognized that the Hamiltonian components $H_{\mu v}^{0}$ depend only on atoms α and β, in this manner, as it were the two-centre lattice components are unequivocally considered calculated, as well as two-centre components of the cover lattice. Based on condition (2.43) the free atom eigenvalues from the inclining of the Hamiltonian network, which guarantees the precise restrain for complimentary particles.

When utilizing Φ_{v} and ρ_{o}^{α} the Hamiltonian and overlap framework components can be calculated as a work of the distance between nuclear sets. As a result, it is not fundamental to recalculate any integrand amid, a geometry optimization or atomic dynamics recreation.

At last, an expository expression for nuclear strengths can be inferred from the overall energy concerning the nuclear space coordinates,

$$\vec{F}_{a} = -\sum_{i}^{M}\sum_{\mu,v}^{N} C_{i\mu}C_{iv}[\frac{\partial H_{\mu v}^{o}}{\partial \vec{R}_{\alpha}} - \epsilon_{i}\frac{\partial S_{\mu v}}{\partial \vec{R}_{\alpha}}] - \frac{\partial E_{rep}}{\partial \vec{R}_{\alpha}} \quad \text{.....2.57}$$

The DFTB approach contains all three demands for an atomistic tight-binding strategy.

2.4.4. The self-consistent charge correction: SCC-DFTB

The SCC-DFTB strategy is based on the second-order extension of the Kohn-Sham add up to energy concerning to the charge density fluctuations [49]. The entire energy expression incorporates not only the standard tight-binding (TB) 'band structure' E_{bs} and the short-range repulsive term E_{rep}, also an electrostatic-interaction term $E_{2}(n, \Delta n)$ that accounts for the charge fluctuations [53]:

$$E_{tot} = E_{BS} + E_{rep} + E_{2}(n, \Delta n) = \sum_{i}^{OCC} n_{i}\langle\psi_{i}|\hat{H}^{o}|\psi_{i}\rangle + E_{rep}$$

$$+\frac{1}{2}\sum_{a,b}^{M}\gamma_{ab}\Delta q_{a}\Delta q_{b} \quad \text{.....2.58}$$

The primary term of the over condition (2.45) is the entirety over the occupied electronic eigenstates ψ_i of the successful Kohn-Sham Hamiltonian $\widehat{H}^o$, derived beneath the estimation that the starting electronic thickness of the many-atom framework can be represented as a superposition of comparing unbiased nuclear charge densities. The Hamiltonian $\widehat{H}^o$ depends only on this appropriately chosen reference density. The second term E_{rep} accounts for the energy contrast between the electronic portion of the (SCC)DFTB strategy and DFT for a conferred reference framework and compromises a summation over the Coulombic and trade twofold counting terms as well as the particle core-core repulsion [53].

To have a much better portrayal of electronic systems and superior transferability of DFTB, from the cases where long-range coulomb intuitive are imperative, the approach has been moved forward which gives rise to the self-consistent charge adjustment DFTB (SCC-DFTB) [49]. To incorporate the density fluctuations in a straightforward however proficient way concurring to a tight-binding approach, δρ composed as the superposition of atom-like contributions $\delta\rho_\alpha$, which quick decay in conjunction with the separation from the comparing nuclear centre,

$\delta\rho = \sum_{\propto}^{N} \delta\rho_\alpha$.....2.59

The atom-like contributions are simplified with monopole approximation:

$\delta\rho_\alpha \approx \Delta q_\alpha F_{00}^{\alpha} Y_{00}$,.....2.60

where Δq_α is the Mulliken Charge, difference between the atomic mulliken population q_α [54] and the number of valence electrons of the neutral free atom $q_{\propto}^{0}(\Delta q_\alpha = q_\alpha - q_{\propto}^{0}), F_{00}^{\alpha}$ denotes the normalized radial dependence of the density fluctuation in the atom an approximated to spherical by the angular function Y_{00}. That is, the impacts of

charge exchange are included, where changes within the shape of the electronic thickness are neglected. Equation (2.18) gets to be:

$$E_{2nd} \approx \frac{1}{2}\sum_{\alpha,\beta}^{N} \Delta q_\alpha \Delta q_\beta \underbrace{\iint \left(\frac{1}{|\vec{r}-\vec{r}'|} - \frac{\delta^2 E_{xc}}{\delta\rho\delta\rho'}\Big|_{\rho_0} \right) F_{00}^{\alpha} F_{00}^{\beta} Y_{00}^{2} d\vec{r} d\vec{r}'}_{\gamma_{\alpha\beta}} \quad \text{.....2.61}$$

the revolution $\gamma_{\alpha\beta}$ was introduced merely for simplicity. To solve equation (2.47) $\gamma_{\alpha\beta}$ is analyzed. Within the restrain case where the interatomic separation is exceptionally large ($\left|\vec{R}_\propto - \vec{R}_\beta\right| = |\vec{r} - \vec{r}'| \to \infty$) one finds, by GGA-DFT, that the exchange-correlation term goes to zero and $\gamma_{\alpha\beta}$ portrays the interaction of two normalized spherical electronic densities, fundamentally diminishing to

$\frac{1}{|\vec{R}_\propto - \vec{R}_\beta|}$, thus:

$$E_{2nd} \approx \frac{1}{2}\sum_{\alpha,\beta}^{N} \frac{\Delta q_\alpha \Delta q_\beta}{|\vec{R}_\alpha - \vec{R}_\beta|} \text{.....2.62}$$

In the other case, where the interatomic distance tends to zero ($\left|\vec{R}_\propto - \vec{R}_\beta\right| = |\vec{r} - \vec{r}'| \to \infty$), $\gamma_{\alpha\beta}$ depicts the electron-electron interaction inside the atom α and can be related with the chemical hardness η_α [55], or Hubbard parameter $\gamma_{\alpha\alpha} = 2\eta_\alpha = U_a$. The atomic hardness can be calculated using the difference between ionization potential I_α and electron partiality A_a of atom α: $2h_\alpha = I_\alpha - A_a$. Due to viable issues, related to the non-existence of different anions and appropriately lost test approval of the electron liking of the comparing components, it is more helpful to misuse DFT to get these parameters.

Janak's theorem [56] application relates the atomic hardness to the subordinate of the HOMO energy concerning to the occupation number of HOMO $\eta_\alpha = \frac{\partial \varepsilon_{\propto,HOMO}}{\partial n_{\propto,HOMO}} = \frac{1}{2}U_a$

and the vitality alter concerning to electron alter inside the HOMO. The approach offers the plausibility to treat the charge commitment shell or indeed orbital-wise, which is critical for the calculation of certain components with s, p, and d holding commitments, particularly for move metals. The values of orbital hardness $\eta_\xi = \frac{\partial \varepsilon_\xi}{\partial n_\xi}$ have been tailed within the writing for elements from H to Xe [56]. The atomic SCC procedure suggests that all sums over charges run over the atomic index α. For orbital-dependent SCC the summation index for the charge would run over the shell index ξ. Employing a DFT method, U_α can be calculated inside the monopole estimation as the moment subsidiary of the entire nuclear vitality α for to its nuclear charge:

$$E_{2nd} \approx \frac{1}{2}\frac{\partial^2 E_\alpha \rho_0}{\partial q_\alpha^2}\Delta q_\alpha^2 = \frac{1}{2}U_\alpha \Delta q_\alpha^2 \quad \text{.....2.63}$$

To get a well-defined and valuable expression for the systems in all scales, and keep consistency with the approximations, an explanatory expression was developed [49] to approximate the density changes with spherical electronic densities. According to slater-type orbitals (Gaussian-type orbitals can also be employed) used to solve the KS equations [53], assumed an exponential decay of the normalized spherical electronic density:

$$\rho_0(\vec{r}) = \frac{\tau_\alpha^3}{8\pi} e^{-\tau_\alpha |\vec{r}-\vec{R}_\alpha|} \quad \text{.....2.64}$$

Neglecting the second-order contributions of E_{xC} in equation (2.47) the following is obtained:

$$\gamma_{\alpha\beta} = \iint \frac{1}{|\vec{r}-\vec{r}'|}\frac{\tau_\alpha^3}{8\pi} e^{-\tau_\alpha |\vec{r}-\vec{R}_\alpha|}\frac{\tau_\beta^3}{8\pi} e^{-\tau_\beta |\vec{r}-\vec{R}_\beta|} d\vec{r} d\vec{r}' \quad \text{.....2.65}$$

Then integrate over $\vec{r}'$, thus:

$$\gamma_{\alpha\beta} = \int [\frac{1}{\vec{r}-\vec{R}_{\propto}} - (\frac{\tau_{\alpha}}{2} + \frac{1}{|C|}) e^{-\tau_{\alpha}|\vec{r}-\vec{R}_{\alpha}|}] \frac{\tau_{\beta}^{3}}{8\pi} e^{-\tau_{\beta}|\vec{r}-\vec{R}_{\beta}|} d\vec{r} \quad \text{.....2.66}$$

Then set $\left|R = \vec{R}_{\propto} - \vec{R}_{\beta}\right|$, after coordinate transformations:

$$\gamma_{\alpha\beta} = \frac{1}{R} - s(\tau_{\alpha}, \tau_{\beta}, R), \quad \text{.....2.67}$$

where s is a short-range function with exponential decay, so that.

$$\lim_{R\to 0} s(\tau_{\alpha}, \tau_{\beta}, R) = \frac{5}{16}\tau_{\alpha} + \frac{1}{R} \quad \text{.....2.68}$$

It was assumed that the second-order contribution can be approximated by the Hubbard parameter $R = 0$, based on equation (2.50), the exponents of equation (2.54) are obtained:

$$\tau_{\alpha} = \frac{16}{5} U_{\alpha} \quad \text{.....2.69}$$

It is noted that harder components tend to have localized wave functions. The chemical hardness of a spin-delocalized particle is calculated by the energy derivative of the most elevated possessed nuclear orbital concerning its occupation number, condition (2.49), employing a completely self-consistent ab initio strategy. In this way, the impact of second-order contributions of the exchanges-correlation is included in $\gamma_{\alpha\beta}$ for short distances, where it is necessary. The exchange-correlation energy vanishes for expansive interatomic separations within the GGA. Within the case of periodic frameworks, the long-range portion s decays exponentially and can be summed over a small number of unit cells. Equation (2.53) could be a well-defined expression for amplified and periodic frameworks. In this way, the whole energy inside SCC-DFTB is composed as

$$E_{SCC} = \sum_i^M n_i \langle \psi_i | \widehat{H}^o | \psi_i \rangle + \frac{1}{2} \sum_{\alpha,\beta}^N \gamma_{\alpha\beta} \Delta q_\alpha \, \Delta q_\beta + E_{rep} \ldots\ldots\ldots\ldots\ldots\ldots\ldots\ldots\ldots\ldots\ldots\ldots\ldots\ldots 2.70$$

The charge fluctuations are calculated by Mulliken population analysis [54]:

$$q_\alpha = \frac{1}{2} \sum_i^M n_i \sum_{\mu \epsilon \alpha}^N \sum_v^N (C_{i\mu} C_{iv} C_{\mu v} + C_{iv} C_{i\mu} C_{v\mu}), \ldots\ldots\ldots\ldots\ldots\ldots\ldots\ldots\ldots\ldots\ldots\ldots\ldots\ldots 2.71$$

and common equations like those in condition (2.32) can be obtained with altered components within the Hamiltonian network:

$$H_{\mu v}^o = \langle \Phi_\mu | \widehat{H}^o | \Phi_v \rangle + \frac{1}{2} S_{\mu v} \sum_\xi^N (\gamma_{\alpha\xi} + \gamma_{\beta\xi}) \Delta q_\xi$$

$$= H_{\mu v}^0 + H_{\mu v}^1, \qquad \forall \mu \epsilon \{\alpha\}, v \epsilon \{\beta\} \ldots\ldots\ldots\ldots\ldots\ldots\ldots\ldots\ldots\ldots\ldots\ldots\ldots\ldots\ldots\ldots 2.72$$

The matrix components $H_{\mu v}^0$ and $S_{\mu v}$ are indistinguishable from those characterized within the standard DFTB strategy, from condition (2.33) the nuclear charges depend on the monoatomic wave capacities ψ_i it is fundamental to utilize a self-consistent procedure. Once the components $S_{\mu v}$ expand to some neighboring atoms, multiple interactions are established. The second-order correlation is accomplished by presenting the component $H_{\mu v}^1$, which depend on the Mulliken charges [57].

Self-consistent charge correction permits for the unequivocal treatment of charge exchange impacts, the transferability of E_{rep} is impressively way better in comparison with the non-self-consistent plot. In standard DFTB, a straightforward explanatory expression for the nuclear strengths can be inferred appropriately:

$$\vec{F}_\alpha = -\sum_i^M n_i \sum_{\mu,v}^N C_{i\mu} C_{iv} \left[\frac{\partial H_{\mu v}^0}{\partial \vec{R}_\alpha} - \left(\varepsilon_i - \frac{H_{\mu v}^1}{S_{\mu v}} \right) \frac{\partial S_{\mu v}}{\partial \vec{R}_\alpha} \right] - \Delta q_\alpha \sum_\xi^N \frac{\partial \gamma_{\alpha\beta}}{\partial \vec{R}_\alpha} \Delta q_\xi - \frac{\partial E_{rep}}{\partial \vec{R}_\alpha} \ldots\ldots\ldots\ldots 2.73$$

The DFTB schemes have been effectively utilized in a wide extend of applications, from atomic compounds [58] to systems in solid state [59, 60].

2.4.5. Dispersion-corrected SCC-DFTB: Weak forces

The London intuitive which are moreover known as the scattering powers are well-defined as appealing strengths between nonpolar particles due to their shared polarizability [61]. The dispersion forces are weaker than ordinary covalent or ionic intuitive and are too 10 times weaker than hydrogen bridge intelligence. It is noted that the scattering strengths have negligible impact on short-range intelligence and can be caught on as the long-range component of van der Waals powers.

In any case of their powerless nature, London's strengths influence numerous essential forms in chemistry, material science, and science. They influence the arrangement of atomic precious stones, the structure of natural particles such as proteins and DNA, adsorption forms, π-π stacking intelligence, among others.

However, both the standard and self-consistent DFTB strategies treat as they were short-range nuclear possibilities and terms with more than two centres are neglected, as clarified over. The Hamiltonian framework components drop off rapidly and ended up unimportant at interatomic separations characteristically found within the region of the van der Waals least. Subsequently, DFTB ignores van der Waals intelligence, especially scattering powers.

Two treatments implied to incorporate scattering interaction posterior have been proposed [62, 63]. The dispersion energy for both cases E_{disp} is calculated independently utilizing observational possibilities and after that included to the DFTB total energy expression.The expansion of E_{disp} does not present any double-counting blunders to the vitality since the van der Walls strengths are missing in DFTB.

We portray the treatment utilized within the show work since both treatments are marginally comparable [63]. The rectification was executed in an exploratory form of the deMon code [64] and make use of the UFF field [65], already accessible in deMon. The dispersion interaction $U_{\alpha\beta}$ between atoms α and β at a distance R is given in Lennard-Jones-type form, which includes two parameters: van der Waals distance $(R_{\alpha\beta})$ and well depth $(d_{\alpha\beta})$:

$$U_{\alpha\beta} = d_{\alpha\beta}\left[-2\left(\frac{R_{\alpha\beta}}{R}\right)^{6} + \left(\frac{R_{\alpha\beta}}{R}\right)^{12}\right] \text{.....2.74}$$

The $R_{\alpha\beta}$ and $d_{\alpha\beta}$ parameters are detailed within the unique paper [65] and are accessible from H to Lw within the intermittent table of components. In UFF the van der Waals term is set to zero concurring to a contiguousness basis: in any case, this requires a resolute topology of the framework, which is not alluring in a quantum-mechanical strategy. To overcome this issue, condition (2.60) is utilized as it were when $U_{\alpha\beta}$ is alluring (London interactions are never repulsive). In expansion, a short-range potential is inferred utilizing the polynomial,

$$U_{\alpha\beta}^{short-range}(R) = U_o - U_1 R^n - U_2 R^{2n}, \text{.....2.75}$$

where U_o, U_1 and U_2 are calculated to make the interaction energy and its, to begin with and moment subsidiaries coordinate equation (2.60) at $R = 2^{-1/6}R_{\alpha\beta}$. The finest esteem recommended for n is 5, which gives the following U_o, U_1 and U_2 parameters [66]:

$$U_o = \frac{396}{25} d_{\alpha\beta}, \text{.....2.76}$$

$$U_1 = 2^{5/6}\frac{672}{25}\frac{d_{\alpha\beta}}{R_{\alpha\beta}^5} \text{ .....2.77}$$

and

$$U_2 = -2^{2/3}\frac{552}{25}\frac{d_{\alpha\beta}}{R_{\alpha\beta}^{10}} \quad \text{.....2.78}$$

Thus, the dispersion potential for the DFTB method can be written as

$$U_{\alpha\beta}(R) = \begin{cases} d_{\alpha\beta}\left[-2\left(\frac{R_{\alpha\beta}}{R}\right)^6 + \left(\frac{R_{\alpha\beta}}{R}\right)^{12}\right], \forall R \geq 2^{-1/6}R_{\alpha\beta} \\ \frac{396}{25}d_{\alpha\beta} - 2^{5/6}\frac{672}{25}\frac{d_{\alpha\beta}}{R_{\alpha\beta}^5} + 2^{2/3}\frac{552}{25}\frac{d_{\alpha\beta}}{R_{\alpha\beta}^{10}}, \forall R < 2^{-1/6}R_{\alpha\beta} \end{cases} \quad \text{.....2.79}$$

and the dispersion energy is given by.

$$E_{disp} = \frac{1}{2}\sum_{\alpha,\beta}^{N} U_{\alpha\beta}(R) \quad \text{.....2.80}$$

This term is included to the total DFTB energy calculated either using standard DFTB or the SCC plot.

2.5 Plane-Wave Pseudopotential Method

Pseudo-potential plane-wave strategies have ended up a backbone for the consideration of basic and electronic properties based on a quantum mechanical treatment. This strategy has been progressed and finalized to dependably predict the inactive and energetic properties of atoms and crystalline solids [67]. The plane-wave pseudopotential strategy has come to be an effective and dependable instrument to consider the properties of wide lesson of materials. The complicated many-body issue of emphatically connected electrons and cores has been mapped inside the system of the Born-Oppenheimer estimation and the Thickness Utilitarian Hypothesis to a single-particle issue moving in a compelling outside potential for a set of settled cores. The most thought of this strategy is to disentangle the DFT issue by considering as it were valence electrons.

2.5.1. Plane-wave Basis

The plane-wave premise sets are liberally utilized within the calculations including boundary conditions, expansion to the localized premise sets, plane-wave premise sets are too utilized in quantum-chemical calculations. Plane-wave premise sets are ordinarily coupled with an “effective centre potential” or pseudopotential in viable execution so that they (plane-wave) are as they were utilized for valence charge thickness.

An interminable plane-wave premise set is utilized to extend the electronic wave capacities of the framework. The strategy is portrayed well by utilizing Bloch’s hypothesis, which states that the electronic wave work at each k-point can be extended in terms of a discrete plane-wave premise set.

$$\psi_{ki}(r) = \exp[ik, r] f_i(r) \ldots\ldots 2.81$$

This expression encompasses a wave-like and cell-periodic portion. The function $f_i(r)$ characterizes the periodicity of the strong and can be extended employing a premise set with a discrete set of plane waves, given by:

$$f_i(r) = \sum C_i G^{[iG,r]}, \ldots\ldots 2.82$$

where G is the corresponding lattice vectors of the occasional cell. Hence, each electronic wave work can be composed as an entirety of plane waves:

$$\psi_{ki}(r) = \sum C_{i,k} + G^{[i(k+G),r]}, \ldots\ldots 2.83$$

where $C_{i,k+G}$ are the coefficients for the plane waves that need to be solved and depend entirely on the specific kinetic energy:

$\frac{\hbar^2}{2m}|K+G|^2$……2.84

The merging of this development is controlled by the choice of the dynamic energy cut-off. The plane-wave premise set is constrained by counting all plane waves whose kinetic energies are less than a few energies cut-off E_{cut}. In this way, as it were the plane waves comply.

$\frac{\hbar^2}{2m}|K+G|^2 < E_{cut}$,……2.85

are included in the basis set. Introduction of E_{cut} to the discrete plane-wave basis set produces a finite basis set. The plane wave set at limited cut-off energy will lead to a blunder within the computed add up to energy; subsequently, the vitality must be expanded until the calculated energy has converged. It is exceedingly fitting and wise to utilize much denser k points to diminish errors and guarantee meeting. Sometimes recently making utilize of the plane wave development of the wavefunction we type in the Kohn-Sham condition of thickness useful hypothesis within the taking after the way [67]:

$\sum\left[\frac{\hbar^2}{2m}|K+G|^2\delta_{GG}+V_{eff}(r)\right]C_{j,K+G}=\varepsilon_j C_{j,K+G}$……2.86

Where,

$V_{eff}(r)=V_{ext}(r)+V_H[n(r)]+V_{XC}[n(r)]$……..2.87

$V_{ext}(r)$, $V_H[n(r)]$, and $V_{XC}[n(r)]$ are Fourier transforms of the external potential of the nuclei, Hartree, and exchange-correlation potentials, respectively.

2.5.2. Pseudo-Potentials

The plane-wave pseudopotential strategy may be a procedure utilized to calculate with precision the variety of self-consistent arrangements to the density useful hypothesis. Physical properties of solids are much reliable on the valence electrons than on the firmly bound centre electrons [68, 69]. In this procedure, the weaker pseudo potential replaces the centre electrons, and the solid alluring coulomb potential interior the ionic centre. The weaker pseudo-potential depicts all subsequently that depicts all notable highlights of a valence electron moving through a crystal, counting relativistic impacts [67, 68]. In this way, the original solid is presently supplanted by pseudo-ion centres pseudo valence electron. These pseudo electrons encounter the same potential outside the centre locale as the first electrons but have a much weaker potential interior the central locale.

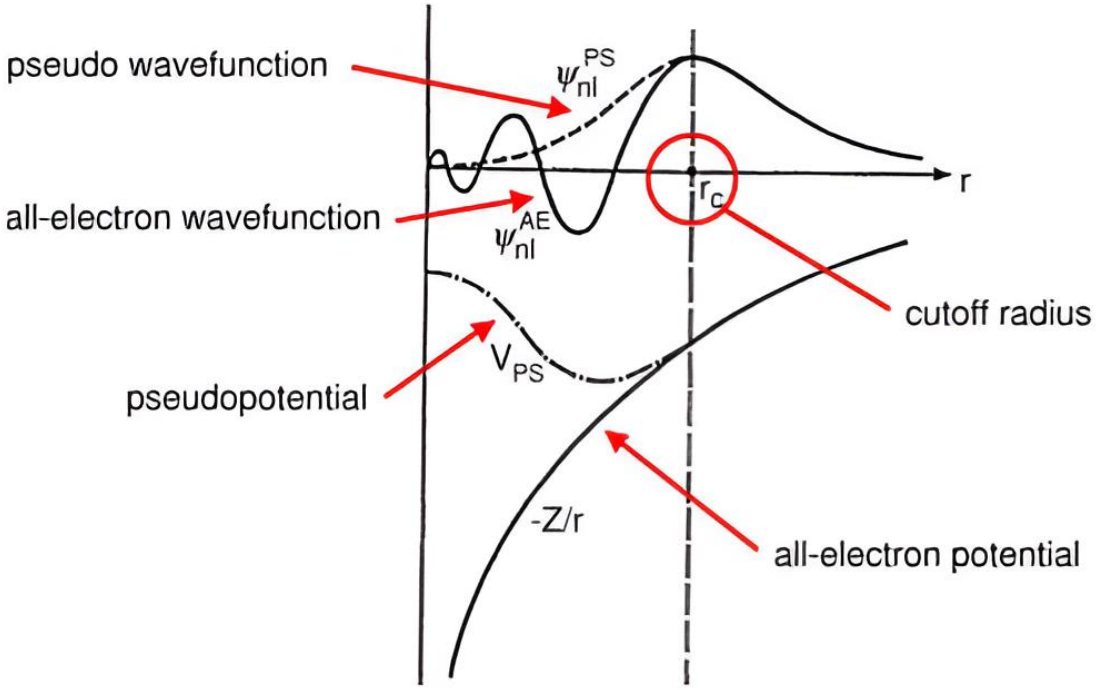

Figure 2.1: Schematic illustration of an atomic all-electron wave function and the corresponding atomic pseudo wave functions.

From figure 2.1 over, the valence wave functions oscillate quickly within the locale involved by the centre electrons due to the solid ionic potential in this region. The oscillations sustain the orthogonality between the centre and valence wave capacities, which is fundamental by the avoidance guideline. The pseudopotential is built superbly so that its scrambling properties or stage shifts for the pseudo wave capacities are indistinguishable from the diffusing properties of the particle and the centre electrons for the valence wave capacities, but in such a way that the pseudo wave capacities have no outspread hubs within the central locale. The presentation of pseudopotential estimation is an endeavour to kill the unsolvable complicated impacts of the centre electrons in movement and they are atomic with a compelling potential, or pseudopotential [70]. In this way, the Schrödinger equation presently contains an adjusted effective potential term rather than the coulombic potential term for centre electrons. Within the pseudopotential approach, as it where valence electrons are managed with expressly [71].

The advantage of utilizing pseudopotential approximation shape calculation can be decided by coordinate comparison with the vitality crevices (known as experimental pseudopotential) from ab-initio calculations. This permits the electronic wave work to be extended employing a much littler number of plane wave premise states and spares an enormous sum of computational time. The pseudo-potential has the frame:

$V_{NL} = \sum_{im} |lm\rangle V_i \langle lm|$,.....2.88

where $|lm\rangle$ is the spherical harmonics and V_i is the pseudo-potential for angular momentum l, acting on the electronic wave-function. Most of the pseudopotentials as of now utilized within the electronic structure are produced from all electron's nuclear

calculations. A pseudo-potential that uses the same potentials for all the precise energy components of the wave work is called a nearby pseudopotential.

2.5.3. Norm Conserving Pseudo-Potential

Norm preserving pseudo-potential is an illustration of a non-local pseudo-potential. Norm-conserving pseudo-potentials execute the condition that exterior of a cut-off span, the standard of each pseudo-wave work is undefined to its consequent all-electron wave work [72]. If the exchange-correlation energy is to be expected precisely, the pseudo wavefunction and the genuine wavefunction exterior the centre locale must be undistinguishable in both their halfway reliance and outright size for two wavefunctions to produce indistinguishable charge densities. Within the attempt to build pseudopotential of this sort, Starkloff, and Joannopoulos [73] presented a course of local pseudopotential that depicted the valence energies and wavefunctions of numerous significant atoms absolutely.

This sort of pseudopotential permits getting the pseudo wave capacities that are indistinguishable to genuine wave capacities past a chosen centre span, whose eigenvalue concurs with the genuine eigenvalue. The property produces a rectify portrayal of holding in pseudopotential calculations and amends self-consistent electrostatics and exchange-correlation possibilities. At the same time, norm-conserving pseudopotentials create the diffusing control of the total molecule potential accurately at energies absent from the bound valence state energy, to begin with arranging within the vitality contrast. Subsequently, norm-conserving pseudopotentials replicate all-electron electronic structure calculations with a high degree of accuracy.

2.5.4. Ultrasoft Pseudo-Potentials

Pseudopotentials create pseudo capacities that are smooth and however exact. Ultra-soft pseudopotentials unwind the norm-conserving imperative to decrease the basis-set estimate [74]. Vanderbilt [74] recommended a more radical approach, the ultra-soft pseudo-potentials (USP). The pseudo wavefunction can be as delicate as conceivable inside the centre locale through the USP plot. It is accomplished by presenting a generalized orthonormality condition. The electron thickness must be increased within the core region to recuperate the total electronic charge. The electron thickness is in this way subdivided into (1) a smooth portion that amplifies all through the unit cell and (2) a difficult portion localized within the central locale. Ultrasoft pseudopotentials have another advantage in addition being milder than their norm-conserving partners.

2.6 Implementation of methods

2.6.1 $DMol^3$

$Dmol^3$ is a density functional theory-based program that predicts the properties of different materials, such as electronic and basic properties [75, 76]. $DMol^3$ permits demonstrating the electronic structures and energetics of particles, solids, and surfaces utilizing thickness utilitarian hypothesis (DFT), which produces profoundly precise come about by keeping the computational costs low for an ab initio strategy. In this consider. In this consider, $DMol^3$ was utilized for geometry optimization of both MnO_2 which was backed by the interaction of Mn-O frameworks. The structures were arranged to be at their ground state vitality some time recently being utilized for self-consistent-charge thickness utilitarian tight-binding (SCC-DFTB) parameterization handle. The GGA-PBE exchange-correlation work coupled with the DND premise set was utilized with k-point inspecting of 6x6x9 for the bulk structure and speaking to the interaction of MnO_2.

2.6.2. DFTB+

Self-consistent density useful tight-binding parameterization and geometry optimization were carried out with a DFTB+ program [49]. Atomic parameters for the interaction between particles in DFTB+ are required to perform different calculations such as geometry optimization and atomic flow. There are a few parameters given inside the program for certain frameworks which can be utilized to perform calculations. Parameterization may be a preparation for creating Slater-Koster records that contains electronic parameters, short-range possibilities, and Hubbard term, chosen for a set of component sets for a system. Successful SCC-DFTB parameterization infers that most properties of the reference frameworks are created with understanding to the test comes about. The effective set of parameters for MnO_2 were accomplished by ceaselessly altering wave work and thickness restriction span for Mn and O components until the reasonable radii were obtained.

2.6.3. VASP

VASP (Vienna Ab-initio Simulation Package) could be a complex bundle planned to perform the primary rule, ab-initio quantum mechanical atomic elements (MD) re-enactments utilizing pseudopotentials or the projector-augmented wave strategy and a wave premise set [77]. The approach actualized in VASP is based on the (limited temperature) nearby thickness estimation with the free vitality as the variational amount and a correct assessment of the immediate electronic ground state at each MD time step. VASP employments productive lattice diagonalization plans and productive Pulay/Broyden charge thickness blending. This procedure is profoundly advanced in that it too dodges all the issues conceivably happening within the unique Car-Parrinello strategy, which is based on the simultaneous integration of electronic and ionic conditions of movement.

The interaction between particles and electrons is depicted by ultra-soft Vanderbilt pseudopotential (US-PP) [74] or by the projector-augmented wave that permits an impressive decrease of the number of plane waves per molecule for move metals and, to start with thrust components. Powers and the total thrust of a tensor can be calculated with VASP and utilized to unwind particles into their transitory ground state. VASP is based on a program at first composed by M. Payne [78] at MIT. Subsequently, VASP features a few roots as the CASTEP/CETEP code but branched from this root at an early organize.

2.6.4. CASTEP Code

CASTEP (Cambridge Sequential Total Energy Package) may be a software package that employments thickness useful theory to provide a great atomic-level portrayal of all ways of fabric and atoms [79]. CASTEP gives measurements that almost add up to energies, powers, and stresses on a nuclear framework, as well as calculating ideal geometries, band structures, optical range, phonon spectra, and much more. It can moreover total atomic energetic recreations. In any case, its traditions thickness utilitarian hypothesis (particularly, utilizing plane waves and pseudo-potential) to solve roughly the Schrodinger condition for intermittent frameworks of atoms, yielding the whole energy, nuclear powers, and inside stresses within the framework, as well as interesting electronic properties (the electron wave work, charge thickness conveyance thickness of electronic states, etc.). Electronic relaxation is accomplished by minimization of the overall energy. The minimization is accomplished utilizing the method called band-by-band, where each wave fun.

CASTEP uses extraordinary k-points analysing for integration over the Brillouin zone and Fast Fourier Alter (FFT) to assess system components [80] [81] [82] [83]. It moreover uses wave work symmetrisation for a precious stone with point bunch

symmetry higher than $P\bar{1}$ and for metallic systems, it presents partial inhabitancies for levels near to the Fermi vitality. It employs both the neighbourhood thickness approximations and the generalized slope estimation for the exchange-correlation energy functional and it is additionally utilizing ultra-soft pseudo-potential as put forward by Vanderbilt as well as norm-conserving potential [74].

Chapter 3: Potentials

3.1 Introduction

In this section, we discuss the parameterization and development of Mn-O potentials using the DMol^3 and the DFTB techniques [84]. The lattice parameters obtained after successfully derived the Mn-O system was compared with the results from the experiment and the DFT technique. Electronic properties such as electronic band structures and the density of states of MnO_2 were investigated to check how the system behaves towards the Fermi level.

3.2 Parameter development for Mn-O

3.2.1 Development of the DFTB set of parameters for MnO_2.

The number of k-points determined with a single point energy calculation of DMol^3, the k-points are determined in a way that the total energy difference per atom is equivalent or less than 1 meV, for this a recognition criterion for proper convergence in DFT calculations. The k-points mesh 6x6x9 was found to be sufficient to converge the MnO_2 structure. The bond distances of Mn-Mn, Mn-O, O-O interactions of atoms are expressed by creating the SCC-DFTB set of parameters.

The fitting process was accomplished for a range of different values of the polynomial order and the value that provides the best fit is chosen, in this case, the minimum order used is 8 and the maximum order used is 12 based on the bond length of the atoms. The longest bond distance was between Mn-O for which is 1.896 Å, this bond distance was used in the fitting process which assisted in determining the cut-off radius scale factor. The fitting was performed with different choices for the cut-off radius, expressed

as a factor of the sum of the covalent radii of the two elements concerned, the value that gives the best fit was chosen.

There are generators used in the parameterization process, for which they produced the desired number of configurations of the Mn-O system. In our case, the reference structures used was the β-MnO_2 structure using two different types of core treatment (all-electron and the DFT semi-core Pseudopots), and an O system using the core treatment (all-electron). However, these two-core treatments used were not only the ones available to be used but the ones that gave the best or more accurate results. The central Mn atoms from both the MnO_2 (all-electron) and the MnO_2 (DFT semi-core Pseudopots) were perturbed from the central position, and the O atom was also perturbed from the central position of the system. Further, we scale the Mn-O from the MnO_2 (DFT semi-core Pseudopots) for which the bond distance between the two atoms is 1.896 Å, such that the number of confirmations were good and ready to be used for parameterization.

The Slater-Koster library file contains the interaction between atoms of these parameters. Moreover, the Slater-Koster library is transferable from one project to the other. The files have information about the parameters, spin constants for the elements, and the wave plot data for each element. The parameterization of MnO_2 was performed by changing the wave function confinement radius (radii 1) and density confinement radius (radii 2) for Mn-O elements using the basis set DNP. It was conducted that the parameters are successfully developed when the wave function and density confinement radii (radii 1) are set to Mn = 2.6 and O = 2.1 Bohr and density confinement radius (radii 2) are set to Mn = 6.0 and O = 6.0 Bohr.

3.3 Structural properties of β-MnO_2

β-MnO_2 (Pyrolusite) is the most thermodynamically stable form of manganese dioxide than the other types of manganese dioxide such as the α-MnO_2, λ-MnO_2, γ-MnO_2, δ-MnO_2 and has a rutile type structure (isostructural to TiO_2) with tetragonal unit cell ($P4_2/mnm$) [85]. The manganese atoms were octahedrally characterized, where the oxygen atoms are octahedrally arranged around the Mn^{4+} ion with d^3 electron configuration.

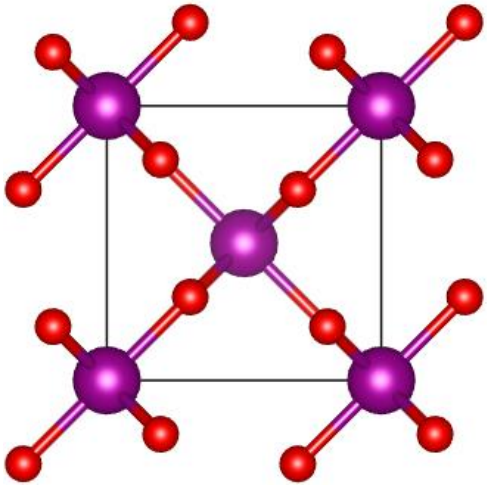

Figure 3.1: Pyrolusite MnO_2 structure with dissimilar atoms characterized by spheres and sticks for bonds; Purple spheres symbolizes Manganese atoms and red spheres symbolize Oxygen atoms.

The lattice parameters are attained from geometry optimization using the DTFB+ code and are listed below in table 3.1. The obtained values of the equilibrium lattice parameters from DFTB+ code together with experimental data and DFT data were compared. The results underneath were found to be in good agreement with the other results that are obtained from other studies. The obtained lattice parameters are within 2% of the experimental data. The atom's positions in table 3.2 are also obtained from the system and are compared to the other atoms positons using different techniques, the attained atom's position using the DFTB+ code is in good agreement with the results from the DFT and experiments.

Table 3.1: Lattice parameters of β-MnO_2 obtained using three different techniques

β-MnO_2 (P42/mnm)	a=b (Å)	c (Å)	V ($Å^3$)
DFTB	4.405	2.870	55.70
EXP [86]	4.408	2.871	55.81
DFT [7]	4.414	2.860	56.44

Table 3.2:

	DFTB		EXP [86]		DFT [7]	
Site	Mn1	O1	Mn1	O1	Mn1	O1
Wyckoff position	2a	4f	2a	4f	2a	4f
X	0.00000	0.28660	0.0000	0.30540	0.00000	0.29295
Y	0.00000	0.28660	0.00000	0.30540	0.00000	0.29295
Z	0.00000	0.00000	0.0000	0.00000	0.00000	0.00000
Occupancy	1.0	1.0	1.0	1.0	1.0	1.0

Coordinates/position atoms in the bulk structure of β-MnO_2

3.4 Electronic properties of β-MnO_2

The electronic properties of a material help with the insight, the categorization of the material under three main phases such as semiconductors, metal, and insulators. The description of a material is determined by the size and existence of the energy gap between the highest occupied orbitals (conduction band) and the lowest unoccupied orbitals (valence band). In semiconductors and insulators, the band gap is present, which happens to be larger for insulators. In metals, the occupied and unoccupied orbitals overlap, hence no gap between the bands is observed. High DOS at specific energy means that there are many states available for occupation and a zero DOS means that no states are available for occupation. In both cases, when using both the

DFT and DFTB techniques an overlap of the occupied and unoccupied orbitals is noticed. This simply means that both our systems show metallic behavior.

3.4.1 Electronic band structures

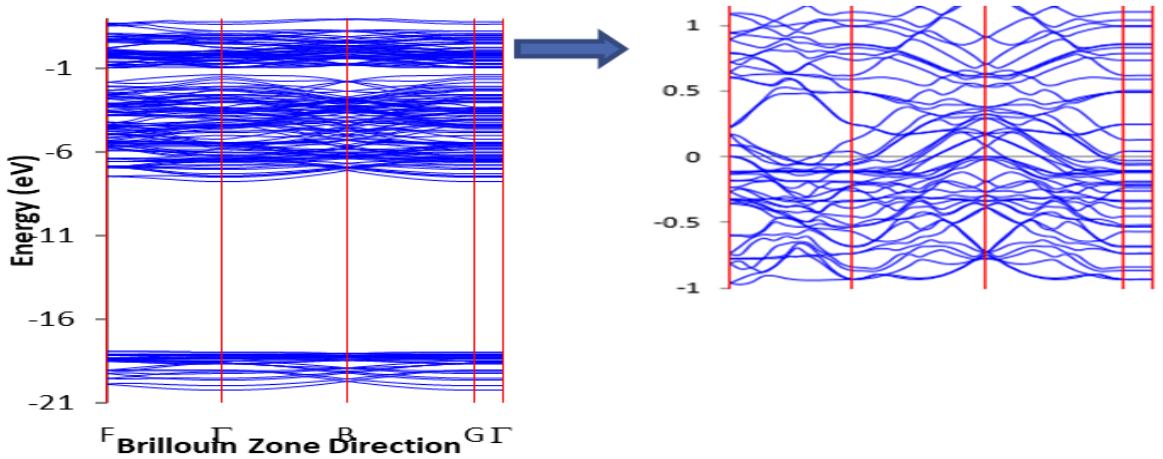

Figure 3.2: Electronic band structures of β-MnO_2 using DFT vasp code.

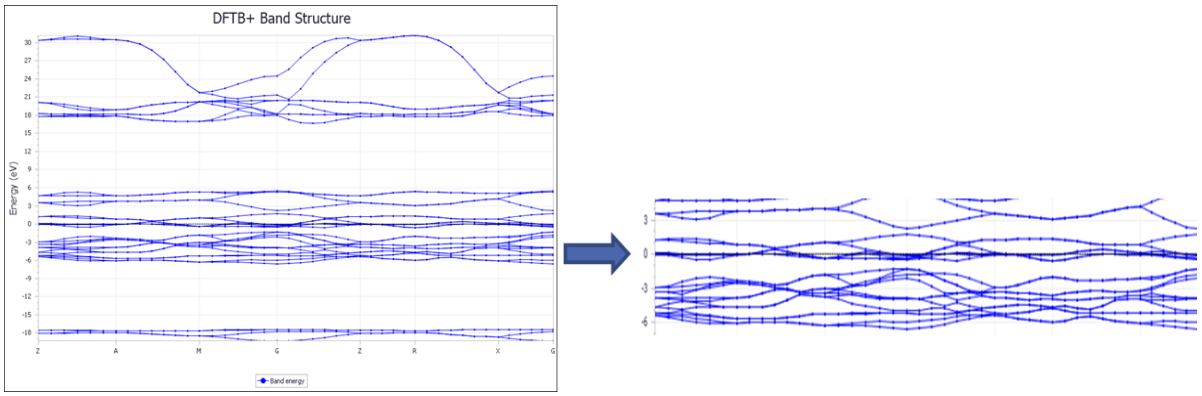

Figure 3.3: Electronic band structures of β-MnO_2 using DFTB.

In metal, the uppermost energy band is moderately packed or the uppermost packed band and the next unoccupied band overlap in energy. Semiconductors have resistivities between those of metals and insulators with a forbidden energy gap of 2 eV or less between the valence and the conduction band. In an insulator, the energy bandgap between the valence and the conduction bands is very large, greater than 2 eV. In our case, the calculated band structures for MnO_2 demonstrate the overlap of orbitals at the fermi level from both the vasp and DFTB codes. However, the absence

of an electronic band due to the filled uppermost energy band indicates that both structures are metallic.

3.4.2 Density of states (DOS)

The graphs below show the total density of states (TDOS) and partial density of states (PDOS) of MnO_2 from two different techniques. The DOS is conveyed in the number of states per atom per energy interval. The plots examine the differences in orbital contributions to each atom of MnO_2. The DOS consists of three kinds/types such as conduction band, Fermi level, and valence band.

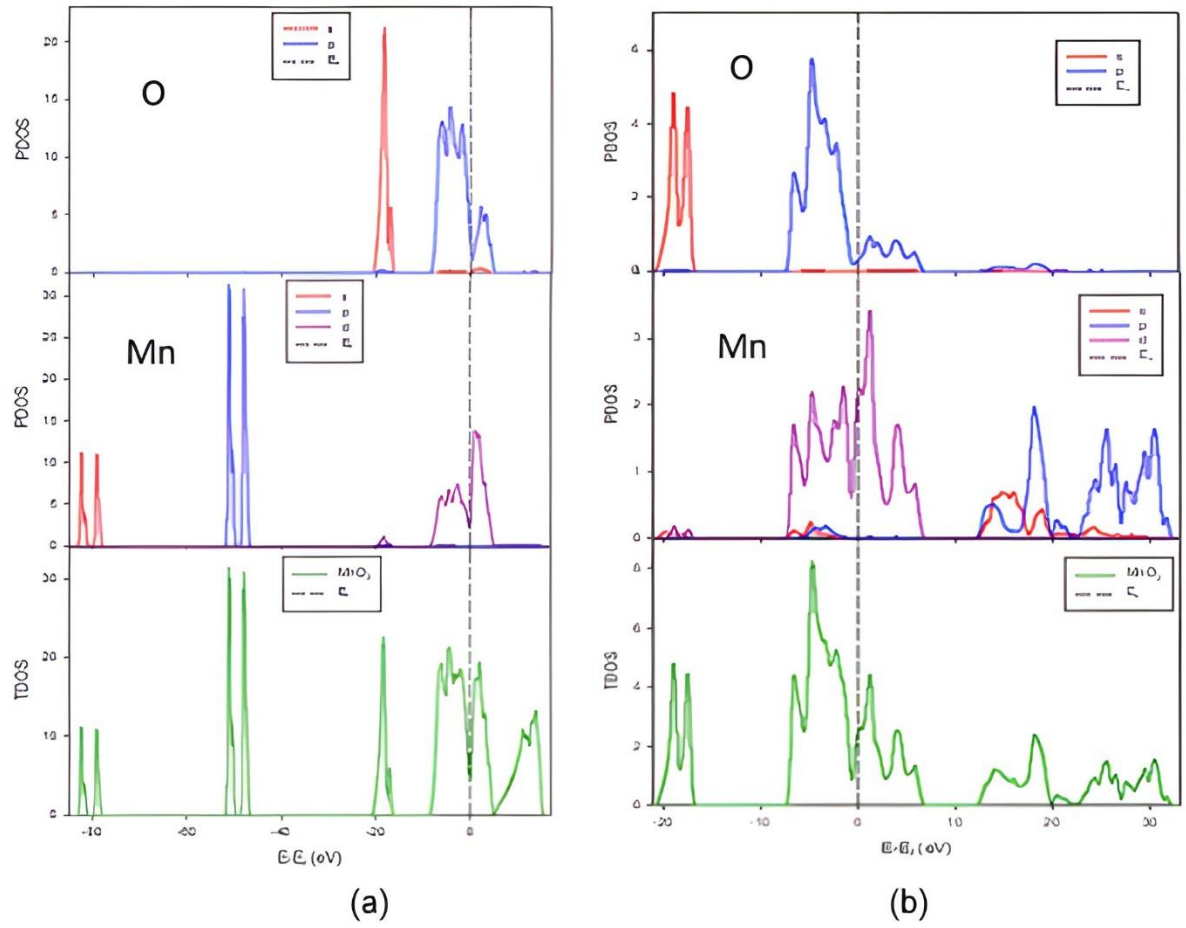

Figure 3.4: Comparison of the DOS for MnO_2 from (a) DFT (vasp) and (b) DFTB results.

Figure 3.4 above shows the calculated total and partial electronic density of states (TDOS/PDOS) for MnO_2 using the vasp and the DFTB codes. However, figure 3.4 (a) shows the DOS from vasp signifies how all the atoms contributed to each band. The

Manganese (Mn) PDOS is dominated by the s and p orbitals with two broad peaks at -85 to -78 eV and -55 to -46 eV, respectively at the conduction band. The d orbital contributes to the conduction band at around -9 to 0 eV. And further, the d orbital of Mn contributes to the valence band from 0 to +19 eV. There is no contribution of the s and p orbitals at the valence band. The oxygen atom shows the contribution of s and p orbital at the conduction band from -20 to -17 eV and -9 to 0 eV, respectively. The p orbital contributes to the valence band at 0 to +8 eV. Additionally, the s and d orbital does not show any contribution at the valence band.

Figure 3.4 (b) shows the DOS from DFTB findings signifying how each one of the orbitals contributed to each band. The conduction band of the Mn atom exhibits one peak of d orbital between -8 and 0 eV. There is no sign of the s and p orbital of Mn at the conduction band. From the valence band the s, p, and d orbital contribute to the band at 11 to +22 eV, +11 to +33 eV, and 0 to +8 eV, respectively. Furthermore, the PDOS of the O atom at conduction band displays the two peaks of s and p orbital from -21 to -17 eV and -8 to -1 eV, respectively. The d orbital does not exist for the O atom.

However, there is a slight shift of the peaks from all the orbitals from the conduction to the valence band. A slight shift is also noticed from the TDOS when both techniques are employed. The DFTB technique might be the reason behind the shift of the TDOS because it typically deals with systems of numerous atoms. The electronic band structures and the total density of states using both the DFT and DFTB techniques are in good agreement with one another since there is an overlap of orbitals at the Fermi level and the absence of a gap at the Fermi level which confirms that the MnO_2 system

is metallic. Previous experimental work [87] has shown similar results to DFT and DFTB obtained.

3.5 Summary

In this chapter, the potentials were developed using the DMol^3 and the DFTB techniques. These techniques were successfully used in the prediction of the lattice parameters of the β-MnO_2 system. The attained structural parameters from the DFTB approach were found to be in good agreement with reported DFT and experimental results. Furthermore, the electronic properties such as the electronic band structures from derived lattice parameters using the DFTB technique were attained to be comparable with the results from the DFT.

Chapter 4: Electronical and mechanical properties in Lithium air batteries

4.1 Introduction

In this chapter, a detail of the results of electronic and mechanical properties of lithium air will be covered. Convergence tests for cutoff and k-points are also investigated to substantiate our ground state energies of the systems. In the previous study [30], the discussion to understand charge transfer reactions that produce the potential difference in the battery from the Li adatom to the surface M (Mn, Ti, and V) to have lithium-air that is valuable is simplified. We investigated the electronic properties of the clean surfaces, surfaces with lithium adsorption, and oxygen adsorption at the Li/MO_2 (110) surfaces. The electronic structures were calculated to check the behavior of the system towards the Fermi level, the density of states was calculated where the stability of the systems was compared.

4.2 Convergence test for the energy cutoff and k-point sampling

4.2.1 Cutoff energy

To obtain the accurate and precise cut-off energy for metal-oxides (TiO_2, VO_2, and MnO_2), the geometry optimization for the cut-off energy and k-points allow the structures to relax completely and the calculations were accomplished for different kinetic energy (from 100 to 900 eV) at default k-points for each system. Energy cutoff is a vital parameter in plane-wave pseudopotential (PWP) calculations since it describes the number of plane waves required in a calculation. Various values of energy cutoff were calculated until constant minimum energy is acquired; thus, the energy becomes stable, and the cutoff energy agrees to the minimum total energy verified. In figure 4.1 to 4.3 below the cut-off energies at different kinetic energy and

the curve of total energy against cut-off energy for metal oxides. The energy cut-off of 500 eV was chosen for systems since it was sufficient for GGA-PBE where the structures could converge.

4.2.2 k-points

After establishing the appropriate cut-off energy, the number of k-points to use in the plane-wave pseudopotential calculations was assessed. Various methods of evaluating the k-points sampling in a Brillouin zone were suggested [88] [89] [90] which help in finding accurate approximation for the total energy by calculating the electronic state at a very small number of k-points. We have carried out total energy calculation at fixed cutoff energy for each system (determined above) while the number of k-points was varied based on the order of constant k-points from the systems. The total energy with respect to the number of k-points was considered converged when the total energy per atom (between two consecutive points) was within 1meV per atom. The k-points were discovered to be 6x6x1 for all the surfaces' metal-oxide systems.

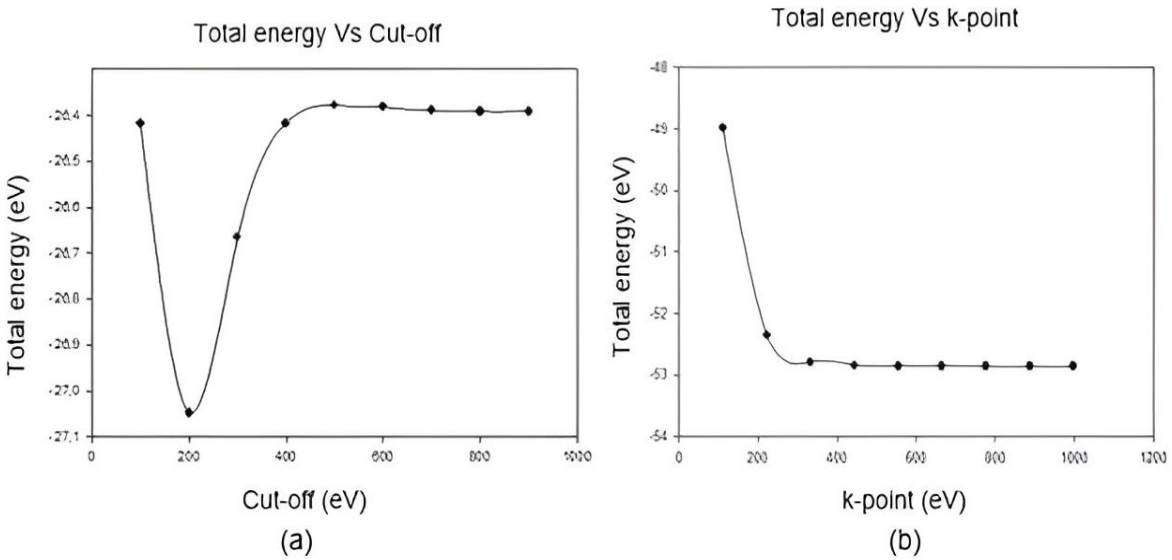

Figure 4.1: (a) Total energy against cut-off and (b) Energy cut-off against variation of the number of k-points for TiO_2.

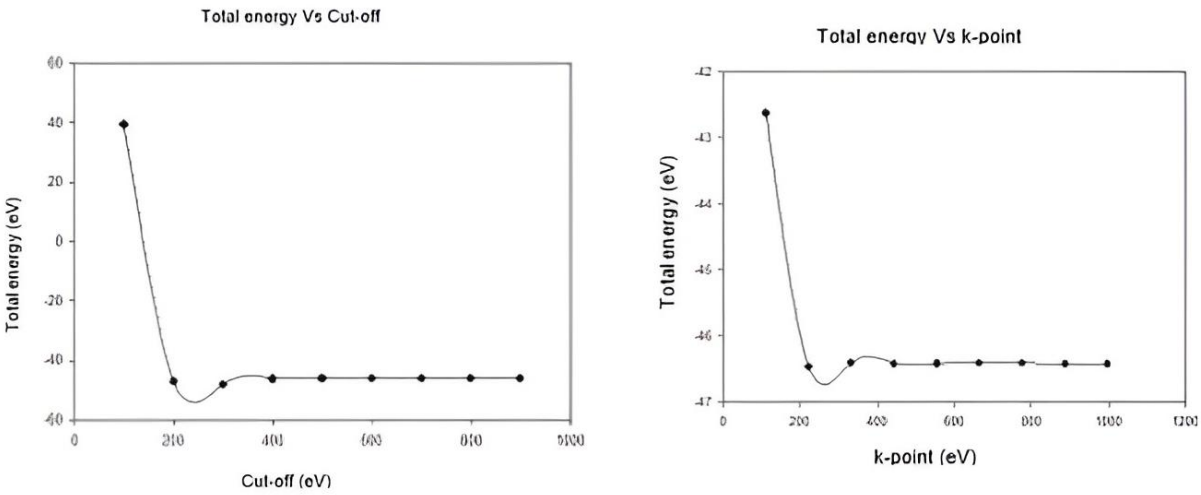

(a) (b)

Figure 4.2: (a) Total energy against cut-off and (b) Energy cut-off against variation of the number of k-points for VO_2.

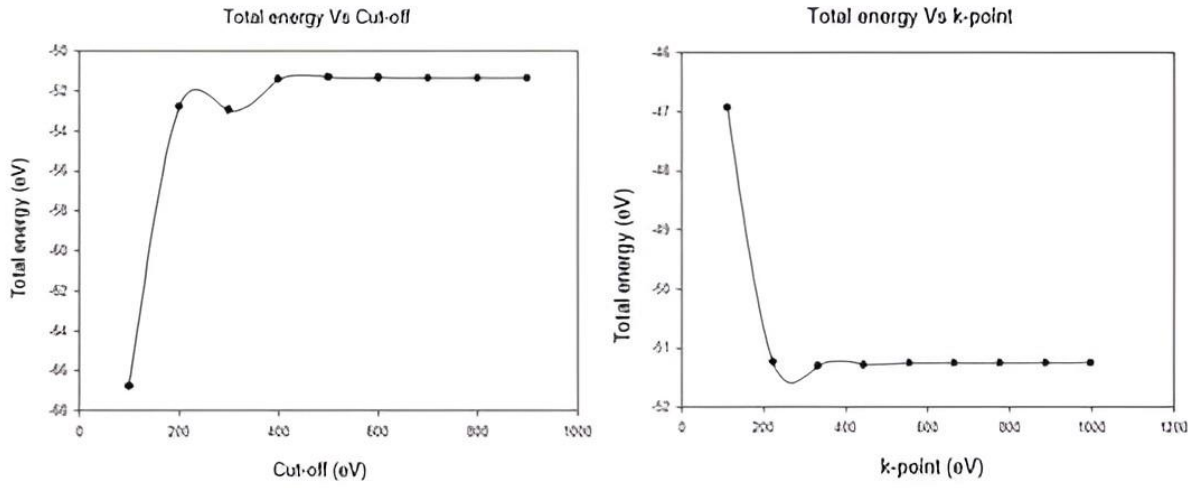

(a) (b)

Figure 4.3: (a) Total energy against cut-off and (b) Energy cut-off against variation of the number of k-points for MnO_2.

4.3 Structural aspects

4.3.1 MO_2 clean surfaces

The β-MnO_2 (110) surface stability prediction was predicted by calculating the surface free energy. The results obtained agree with the mechanism that occurs when β-MnO_2

is used as a catalyst in the Li-air batteries that enhances the reduction of the oxygen molecule. The stoichiometric β-MnO_2 (110) surface was found to be stable and the β-TiO_2 (rutile) has the same structure as β-MnO_2 and can also act as a catalyst in Li-air batteries, the β-VO_2 was determined to be the least stable structure based on the determined surface energies. A similar trend of surface energies for all three isostructural transitional metal oxides (MnO_2, TiO_2, and VO_2), (110) surface was found to be the most stable surface.

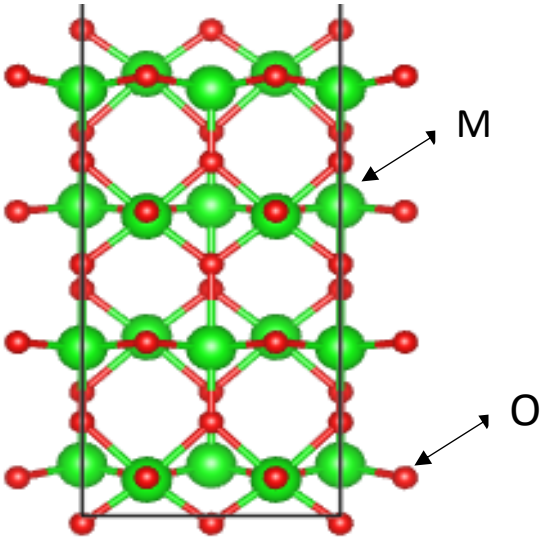

Figure 4.4: Tetragonal structure for rutile MO_2, with green spheres symbolizing the metal atom (M = Mn, V, and Ti) and red spheres embodying the oxygen atom.

4.3.2 Lithium adsorption

From the clean surfaces of MO_2 in figure 4.4 above, the primary step was to decide onto which surface location Li is specially adsorbed. Distinctive potential adsorption locales on the surface were methodically tested and the results are detailed within past studies [30]. It was found out that Li adatoms are more stable in sites of high oxygen coordination. The site with the least adsorption energy is that where Li is triply facilitated, bonded to two bridging and one in-plane oxygen molecule (bbi). Another adsorption site, with essentially the same adsorption energy, has Li coordinated to one

bridging and two in-plane oxygen molecules (bii). Sites with Li bonded to only two bridging oxygen (bb), or one bridging oxygen (b) do not take after the nearby minima of the potential energy scene and can only be stabilized by symmetry imperatives.

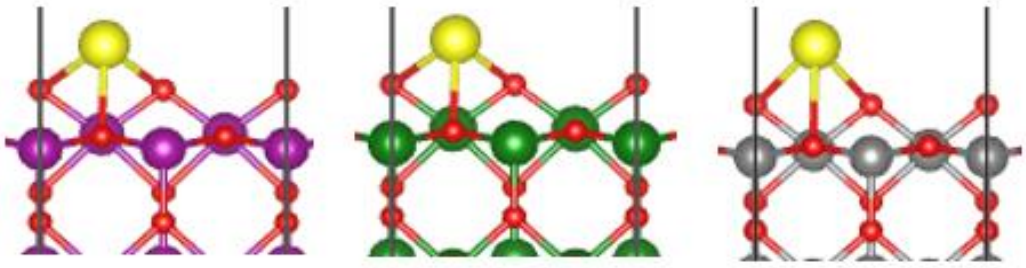

(a) (b) (c)

Figure 4.5: Lithium adsorption on relaxed (a) MnO_2, (b) TiO_2 and (c) VO_2 (110) surfaces.

4.3.3 Oxygen adsorption at the Li/MO_2 (110) surface

Some of the major products that have been reported in [30], and are bulk Li_2O_2 peroxos and monomers both with O-O the bond length of about 1.55 Å. The adsorption of oxygen (two O atoms per surface cell, Γ =2) on the Li/MO_2 (110) surface is considered. From [30], it is observed that the dissociated configuration is the most stable relative to all configurations, for the three metal oxides, which is followed by the peroxo on Mn configuration which is coherent with the calculated adsorption energies. The less stable configuration is the peroxo on Li and the least is peroxo on M/Li relative to the configurations, where the last two are near equivalent for VO_2.

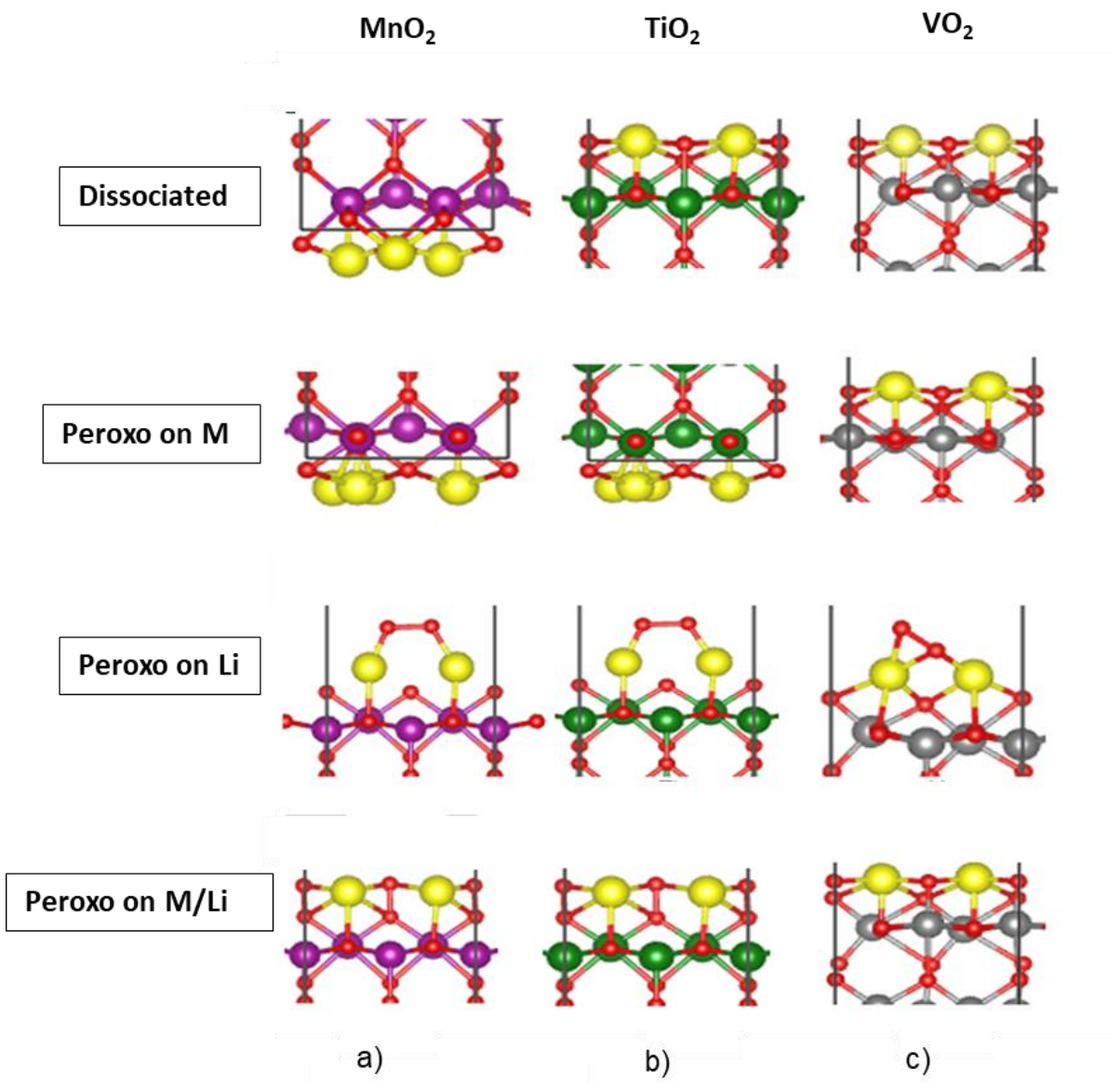

Figure 4.6: Stable configurations for oxygen adsorption at Li (a) MnO_2, (b) TiO_2, and (c) VO_2 (110) surface {M= Mn, Ti, & V}.

4.4 Elastic properties of clean surfaces

The precise calculation of elasticity is more fundamental for obtaining an understanding of the mechanical stability and elastic properties of a solid. Mechanical stability in an orthorhombic crystal leads to the taking after limitations on the flexible constants:

$(C_{11}+C_{22}-2C_{12})>0$, $(C_{11}+C_{33}-2C_{13})>0$, $(C_{22}+C_{33}-2C_{23})>0$,……4.1

$C_{11}>0$, $C_{22}>0$, $C_{33}>0$, $C_{44}>0$, $C_{55}>0$, $C_{66}>0$, $(C_{11}+C_{22}+C_{33}+2C_{12}+2C_{13}+2C_{23})>0$ 4.2

Where C_{11}, C_{12}, C_{13}, C_{22}, C_{23}, C_{33}, C_{44}, C_{55} and C_{66} are the independent elastic constants.

Based on the three independent single crystal elastic constants of a cubic crystal, the elastic moduli are determined using the following equations:

$$B = \left(\frac{C_{11}+2C_{12}}{3}\right) \qquad C' = \frac{C_{11}-C_{12}}{2} \qquad A = \frac{2C_{44}}{C_{11}-C_{12}} \quad \text{.....4.3}$$

Where B is the bulk modulus, C' is the tetragonal shear modulus, and A being the anisotropic factor.

The elastic moduli are determined using these expressions: the bulk modulus B, shear modulus G, anisotropic factor A, tetragonal shear modulus C', and the B/G ratio. The bulk modulus is a measure of resistance to volume change under pressure, while shear modulus G describes the resistance to shape change caused by shearing force, whereas elastic anisotropy A has a valuable implication in engineering science. If the material is entirely isotropic, the value of A will be 1, while values smaller or larger than 1 measure the degree of elastic anisotropy.

The TiO_2 and MnO_2 satisfy all the stability criteria set above for orthorhombic crystal. The TiO_2 and MnO_2 have positive C' values which suggest that these structures are mechanically stable, and all the other criteria above are obeyed. However, the VO_2 is mechanically unstable since the C_{44} value appears to be negative leading to the negative value of anisotropy, as such not all the criterion for stability is met under VO_2 system. The ductility of molecules is determined using the B/G ratio, if $k = B/G > 1.75$ ductile, otherwise brittle. MnO_2 and TiO_2 are both brittle since the $B/G < 1.75$. However, VO_2 is ductile since $B/G > 1.75$ [88].

Table 4.1: Elastic constants of TiO_2, MnO_2 and VO_2 clean surfaces.

	TiO_2	MnO_2	VO_2
C_{11}	99	195	222
C_{12}	75	70	83
C_{13}	12	4	22
C_{22}	219	174	190
C_{23}	20	12	12
C_{33}	28	6	9
C_{44}	28	48	-28
C_{55}	20	21	12
C_{66}	53	66	58
C’	61.68	62.28	69.5
A	0.46	0.76	-0.40
B/G	1.70	1.44	2.53

Table 4.2: The elastic moduli obtained for surfaces are outlined below.

	Voigt		
Modulus	TiO_2	MnO_2	VO_2
Bulk (GPa)	73.23	60.86	72.89
Shear (GPa)	42.92	42.18	28.71
Young's (GPa)	107.7	110.5	76.13

4.5 Phonon Dispersion for clean surfaces

The phonon dispersion curves for clean surfaces MnO_2, VO_2, and TiO_2 were calculated and are displayed in figure 4.7 below. The dispersion curves are invented from two types of phonons specifically the optical and acoustic modes associated with the upper and lower sets of curves in the diagrams, respectively. We note that the MnO_2 displays no negative phonon vibrations along high symmetry point Γ(0,0,0), but

only imaginary modes are observed along Z, A, and R direction. Which suggests the vibrational stability of MnO_2. We notice that the negative phonon vibrations remain down to -9THz along Γ direction, extended to X, and M direction for VO_2. The presence of soft modes along Γ direction suggests the instability of the VO_2 structure. All phonon branches lie above 0THz along Γ direction and as such no soft modes are observed along with high symmetry directions, from the S direction imaginary modes are noticed down to -1THz. The TiO_2 is vibrational stable. This confirms the predicted order of stability as TiO_2 > MnO_2 > VO_2, in agreement with the density of states.

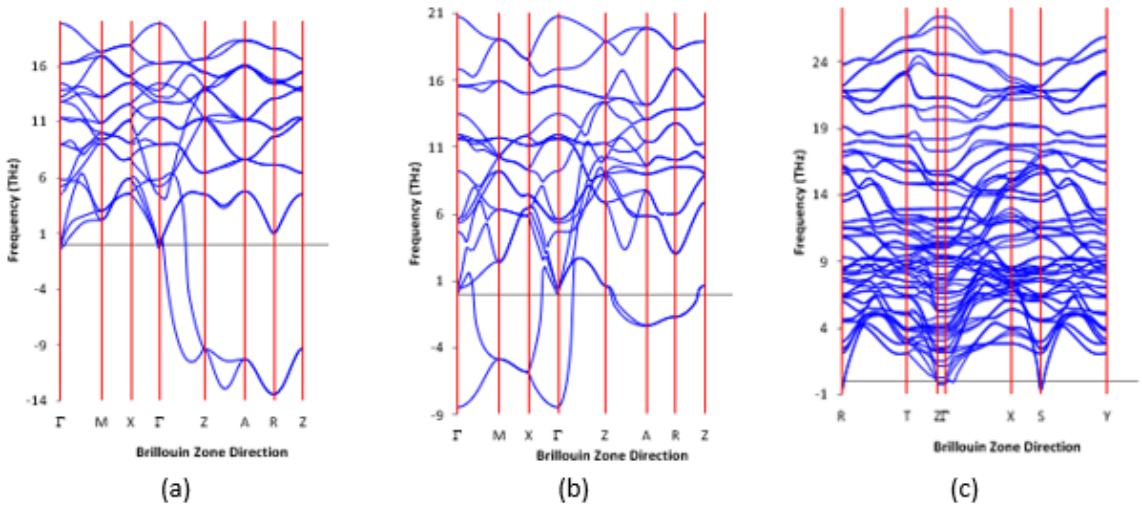

Figure 4.7: Phonon dispersion curves for (a) MnO_2, (b) VO_2, and (c) TiO_2 for the clean surfaces.

4.6 Electronic properties

4.6.1 Band structures

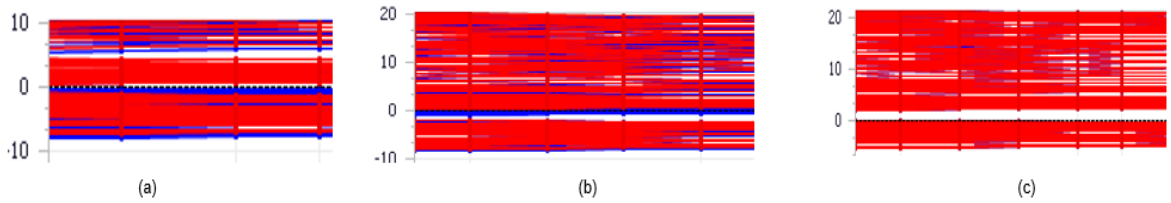

Figure 4.8: Electronic band structures of (a) MnO_2, (b) VO_2, and (c) TiO_2 clean surfaces.

The calculated band structure for MnO_2 and TiO_2 displays the presence of a direct gap of 0.094 eV and 1.984 eV respectively, which implies that the systems are semiconductors. However, there is an absence of an electronic band gap for VO_2 at the fermi level thus the structure is metallic.

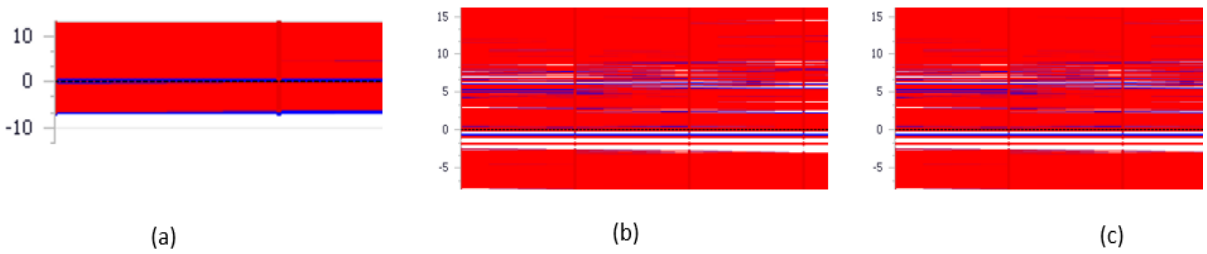

Figure 4.9: Electronic band structures of (a) $(LiMn_8O_{16})_2$, (b) $(LiV_8O_{16})_2$, and (c) $(LiTi_8O_{16})_2$ adsorbed surfaces.

The calculated band structure for $(LiMn_8O_{16})_2$ demonstrates the existence of a direct gap at the fermi level of about 0.095 eV thus, the systems is a semiconductor. Furthermore, there is an absence of an electronic band gap at the fermi level for both $(LiTi_8O_{16})_2$ and $(LiV_8O_{16})_2$ thus the systems are metallic.

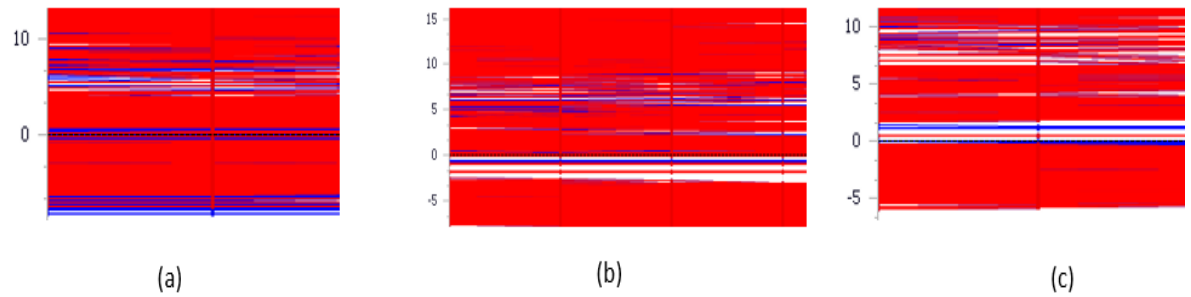

Figure 4.10: Electronic band structures of (a) $(LiMn_4O_9)_4$, (b) $(LiV_4O_9)_4$, and (c) $(LiTi_4O_9)_4$ dissociated surfaces.

The calculated band structure for $(LiMn_4O_9)_2$ and $(LiTi_4O_9)_4$ reveals the presence of a direct gap of 0.007 eV and 0.547 eV respectively, which signifies that the systems are semiconductors. However, there is an absence of an electronic band gap for $(LiV_4O_9)_4$ at the fermi level thus the structure is metallic.

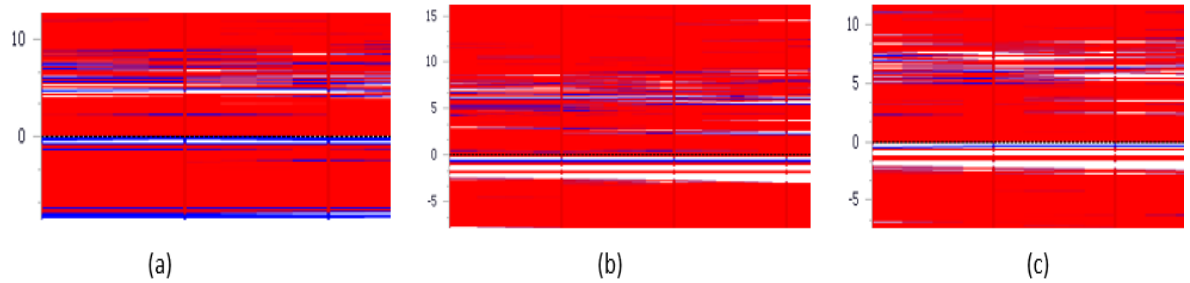

Figure 4.11: Electronic band structures of (a) $(LiMn_4O_9)_4$, (b) $(LiV_4O_9)_4$, and (c) $(LiTi_4O_9)_4$ peroxo on Li.

The calculated electronic band structures from all the systems $(LiMn_4O_9)_2$, $(LiTi_4O_9)_4$, and $(LiV_4O_9)_4$ confirm an absence of a gap at the fermi level. Consequently, all the systems are metallic.

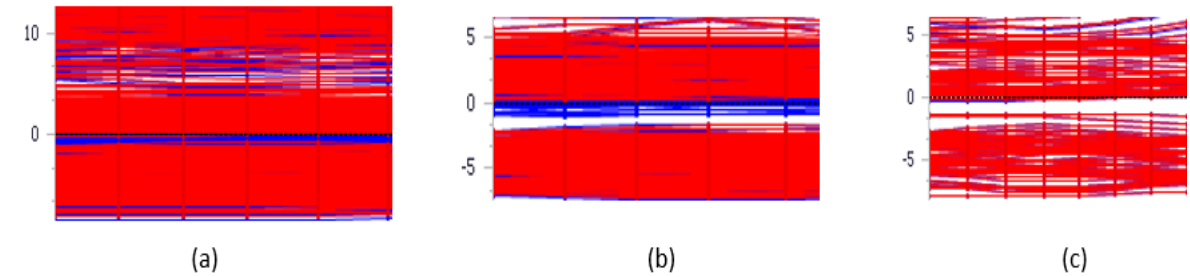

Figure 4.12: Electronic band structures of (a) $(LiMn_4O_9)_4$, (b) $(LiV_4O_9)_4$, and (c) $(LiTi_4O_9)_4$ peroxo on Li-M.

The calculated electronic band structures from all the systems $(LiMn_4O_9)_2$, $(LiTi_4O_9)_4$, and $(LiV_4O_9)_4$ validates an absence of a gap at the fermi level. Subsequently, all the systems are metallic.

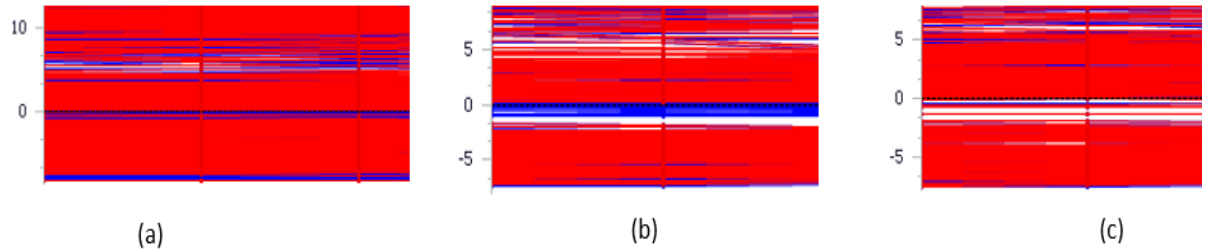

Figure 4.13: Electronic band structures of (a) $(LiMn_4O_9)_4$, (b) $(LiV_4O_9)_4$, and (c) $(LiTi_4O_9)_4$ peroxo on M.

The calculated band structure for $(LiMn_8O_{16})_2$ illustrates the presence of a direct gap at the fermi level of about 0.035 eV, as a result, the system is a semiconductor. Moreover, there is an absence of an electronic bandgap at the fermi level for both $(LiTi_8O_{16})_2$ and $(LiV_8O_{16})_2$ thus the systems are metallic.

4.6.2. Density of states

The graphs below show the total density of states (TDOS) for clean surfaces, lithium and oxygen adsorption, and co-adsorption on MO_2 (M = Mn, Ti, V). The density of states (DOS) is expressed in the number of states per atom per energy interval. We plot TDOS to examine the differences in the structural stability of each atom, related to the details of the contribution of the atoms at the fermi level concerning the pseudo gap. The structure with the highest and lowest density of states at E_f is examined as the least and most stable, respectively.

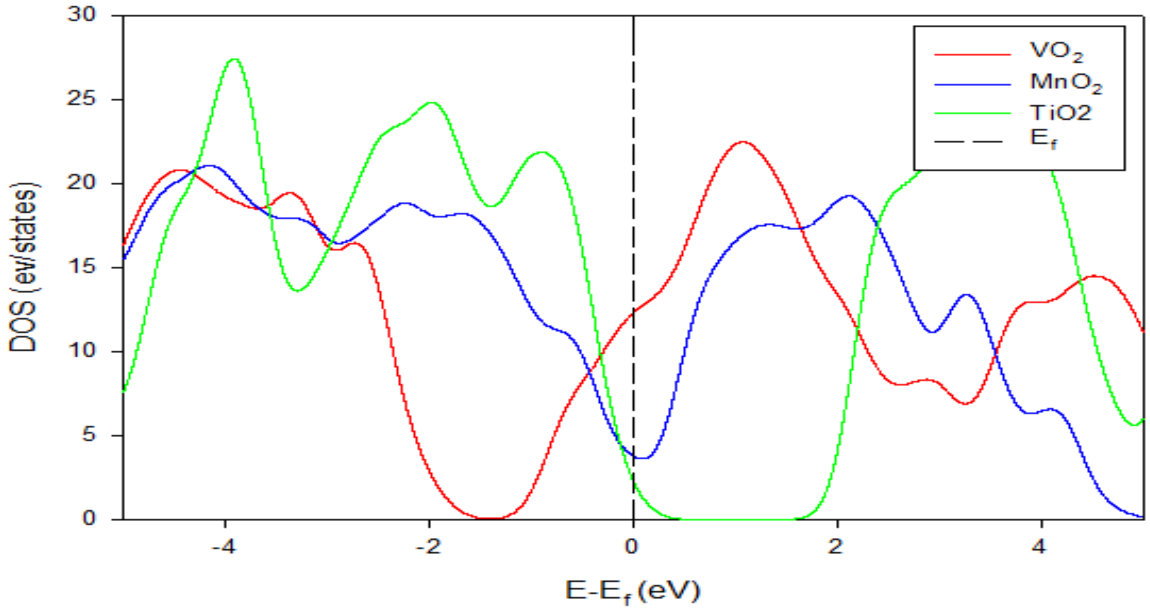

Figure 4.14: Comparison of the total density of states for the clean surfaces.

The graph above (Figure 4.14) shows the total density of states (TDOS) for MnO_2, TiO_2, and VO_2 surfaces. The density of states (DOS) is expressed in the number of states per atom per energy interval. We observe that near E_f the DOS peak of VO_2 has a higher density of states which confirms that it is the least stable. However, TiO_2 has a lower density of states compared to the other structures near E_f. It is distinctly visible that TiO_2 is the most stable compared to VO_2 and MnO_2, whereas the MnO_2 system is found in between the most stable and the less stable. The stability trend can be written as $TiO_2 > MnO_2 > VO_2$.

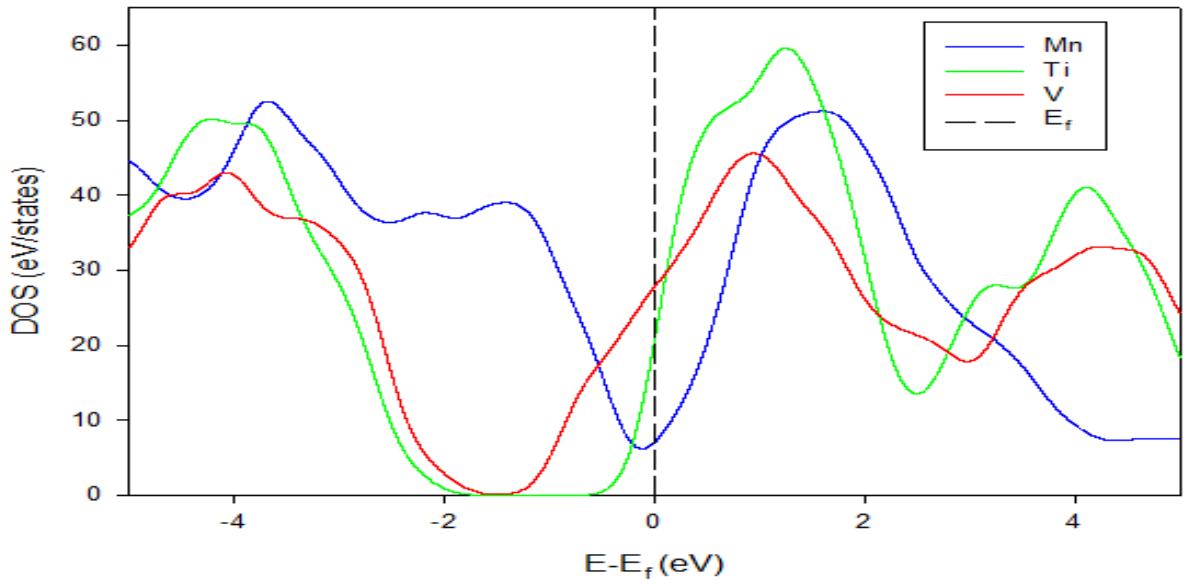

Figure 4.15: Comparison of the total density of states for the Li adsorption surfaces.

In Figure 4.15 above, we observe that near E_f the DOS peak of $(LiMn_8O_{16})_2$ has a lower density of states which approves that it is the most stable. The slight shift to the valence band of the DOS for $(LiTi_8O_{16})_2$ and $(LiV_8O_{16})_2$ is observed in comparison with the DOS for the clean surfaces. However, $(LiMn_8O_{16})_2$ has a lower density of states compared to the other structures near E_f, the $(LiV_8O_{16})_2$ DOS are just above the DOS for $(LiTi_8O_{16})_2$. It is visible that $(LiMn_8O_{16})_2$ is the most stable compared to $(LiV_8O_{16})_2$ and $(LiTi_8O_{16})_2$, the stability trend can be written as $(LiMn_8O_{16})_2$ > $(LiTi_8O_{16})_2$ > $(LiV_8O_{16})_2$.

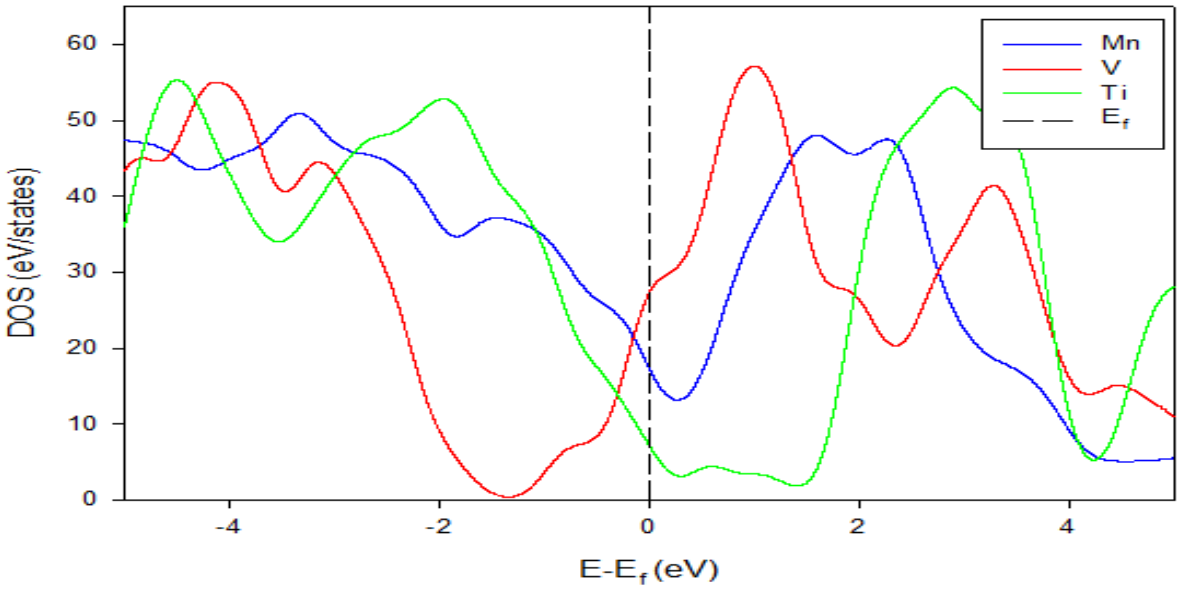

Figure 4.16: Comparison of the total density of states for the dissociated surfaces.

From Figure 4.16 Above, we observe that near E_f the DOS peak of $(LiV_4O_9)_4$ has a higher density of states which approves that it is the least stable. However, $(LiTi_4O_9)_4$ has a lower density of states compared to the other structures near E_f. It is visible that $(LiTi_4O_9)_4$ is the most stable compared to $(LiV_4O_9)_4$ and $(LiMn_4O_9)_4$, the stability trend can be written as $(LiTi_4O_9)_4 > (LiMn_4O_9)_4 > (LiV_4O_9)_4$.

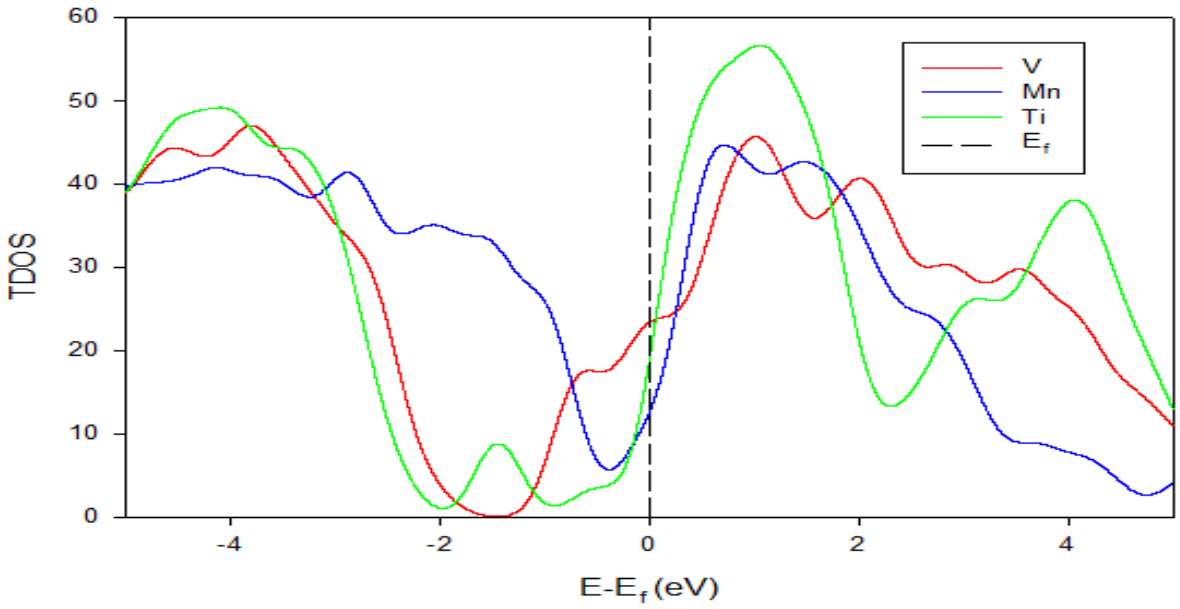

Figure 4.17: Comparison of the total density of states for the Peroxo on Li surfaces.

The graph above (Figure 4.17) shows the total density of states (TDOS) for $(LiMn_4O_9)_4$, $(LiTi_4O_9)_4$, and $(LiV_4O_9)_4$ surfaces. The density of states (DOS) is expressed in the number of states per atom per energy interval. We notice that towards E_f the DOS peak of $(LiMn_4O_9)_4$ has a lower density of states which agrees that it is the most stable structure. Furthermore, we notice that $(LiTi_4O_9)_4$ and $(LiV_4O_9)_4$, both have a higher density of states at E_f compared to $(LiMn_4O_9)_4$. The DOS for $(LiV_4O_9)_4$ has a higher density of states at E_f, indicating that it is the least stable structure. The stability trend can be written as $(LiMn_4O_9)_4 > (LiTi_4O_9)_4 > (LiV_4O_9)_4$.

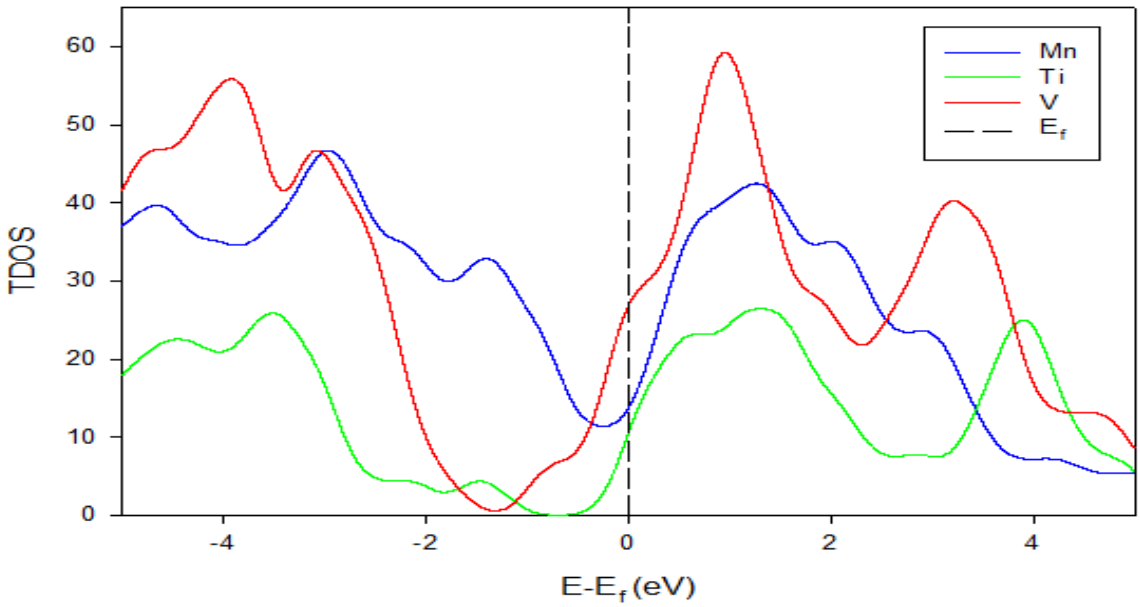

Figure 4.18: Comparison of the total density of states for the Peroxo on Li/M surfaces.

The graph above (Figure 4.18), shows the total density of states (TDOS) for $(LiMn_4O_9)_4$, $(LiTi_4O_9)_4$, and $(LiV_4O_9)_4$ surfaces. The density of states (DOS) is expressed in the number of states per atom per energy interval. We notice that along with E_f the DOS peak of $(LiTi_4O_9)_4$ has a lower density of states which agrees that it is the most stable structure with a slight shift towards the conduction band. Furthermore, we notice that $(LiMn_4O_9)_4$ and $(LiV_4O_9)_4$, both have a higher density of states at E_f compared to $(LiTi_4O_9)_4$. The shift from the valence band from both $(LiMn_4O_9)_4$ and $(LiV_4O_9)_4$ to the conduction band is observed. The DOS for $(LiV_4O_9)_4$ has a higher density of states at E_f, indicating that it is the least stable structure. The stability trend can be written as $(LiTi_4O_9)_4 > (LiMn_4O_9)_4 > (LiV_4O_9)_4$.

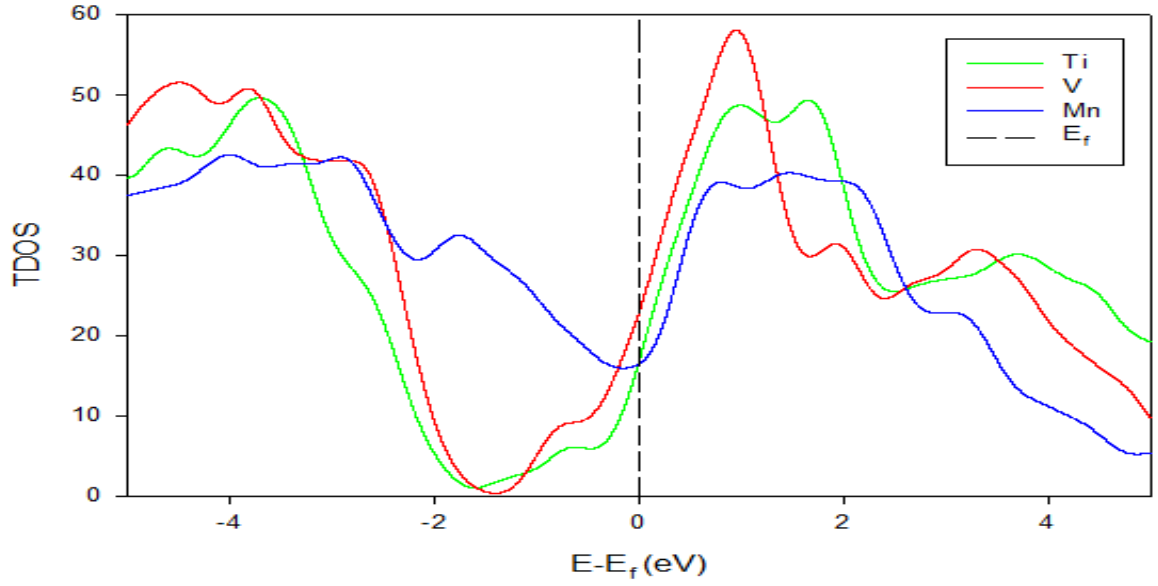

Figure 4.19: Comparison of the total density of states for the Peroxo on M surfaces.

The graph shows (Figure 4.19), the total density of states (TDOS) for $(LiMn_4O_9)_4$, $(LiTi_4O_9)_4$, and $(LiV_4O_9)_4$ surfaces. The density of states (DOS) is expressed in the number of states per atom per energy interval. We note that near E_f the DOS peak of $(LiMn_4O_9)_4$ has a lower density of states which agrees that it is the most stable. However, we notice that $(LiTi_4O_9)_4$ and $(LiV_4O_9)_4$, both have higher density of states at E_f compared to $(LiMn_4O_9)_4$. The shift from the valence band from both $(LiTi_4O_9)_4$ and $(LiV_4O_9)_4$ to the conduction band is observed. The DOS for $(LiV_4O_9)_4$ has a higher density of states at E_f, implicating that it is the least stable structure. The stability trend can be written as $(LiMn_4O_9)_4 > (LiTi_4O_9)_4 > (LiV_4O_9)_4$.

The above discussed results prove or show the correspondence of elastic constants and phonon dispersion, band structures, and density of states. The assurance of elastic constants requires information of energy bends as a function of lattice strain for distinctive unit cell deformation. Within the DFT system, mechanical and electronic properties of different materials have been calculated and critical results are produced.

Unfortunately, there is no exploratory or hypothetical information of elastic constants to compare with our numerical results for the (110) surfaces.

Looking at both the elastic constant and phonon dispersion, there is a relationship between the systems (MO_2). The MnO_2 and TiO_2 share the comparative characteristics since their elastic constants are found to be mechanically stable in conjunction with the phonon dispersion, in any case, the VO_2 elastic constants were found to have a negative value of C_{44} while within the phonon dispersion along with the gamma (Γ) locale negative vibrations were noticed. It is well known that B, C', and C_{44} must be positive for a structure to remain mechanically stable. The negative C_{44} value for VO_2 is responsible for the negative vibrations found along the Brillouin zone on the phonon dispersion.

The composition is isotropic when values are littler or bigger than 1 to measure the degree of elastic anisotropy, consequently, MnO_2, TiO_2, and VO_2 structures satisfy the condition for the framework to be isotropic with VO_2 having negative esteem. The ductility of the particles was decided based on the Pugh's ratio, wherein case $k = B/G > 1.75$ ductile, otherwise brittle [88]. Both the MnO_2 and TiO_2 are found to be brittle with VO_2 being ductile.

It is critical to understand the way electrons are apportioned for individual molecules within the systems. The band structure may be a great way to imagine the wave vector-dependence of the energy states, the bandgap, and the conceivable electronic transitions. The actual transition probability depends on how numerous states are accessible in both the starting and last energies. The correspondence between the electronic band structure and DOS is greatly different, the MnO_2 and TiO_2 clean surfaces both have a bandgap of approximately 0.094 eV and 1.984 eV for which both

the frameworks are found to be steady. The coordinate bandgap observed for MnO_2 and VO_2 lead to the semiconductor behaviour of the frameworks, though the VO_2 was found to have orbital overlap at the Fermi level due to a high density of states. After effectively dissociating the clean surfaces the behaviour of the frameworks changed with a lesser potion where the bandgaps of MnO_2 and TiO_2 diminished by the little potion. With VO_2 remaining unaltered concurring to its contributions.

After successful adsorption with oxygen at the Li/MO_2, the clusters (dissociated, peroxo on Li, peroxo on Li/M, and peroxo on M) are produced. Configurations such as peroxo on Li, and peroxo on M yielded the same trend of stability since the density of states for $(LiMn_4O_9)_4$ intercepts the Fermi level at a lowest point, followed by the $(LiTi_4O_9)_4$ configurations. However, the configuration of $(LiMn_4O_9)_4$ peroxo on Li/M is slightly less stable than that of $(LiTi_4O_9)_4$. All density of states of V based configurations, $(LiV_4O_9)_4$, intercept the Fermi level at highest points alluding to less stability. Such trends are affirmed by the catalytic activities of MO_2 surfaces, shown in Figure 4.20, reported by [91]. The only deviation from such behaviour is reflected by the dissociated configuration, where the $(LiTi_4O_9)_4$ is more stable than $(LiMn_4O_9)_4$, and this anomaly could be further explored.

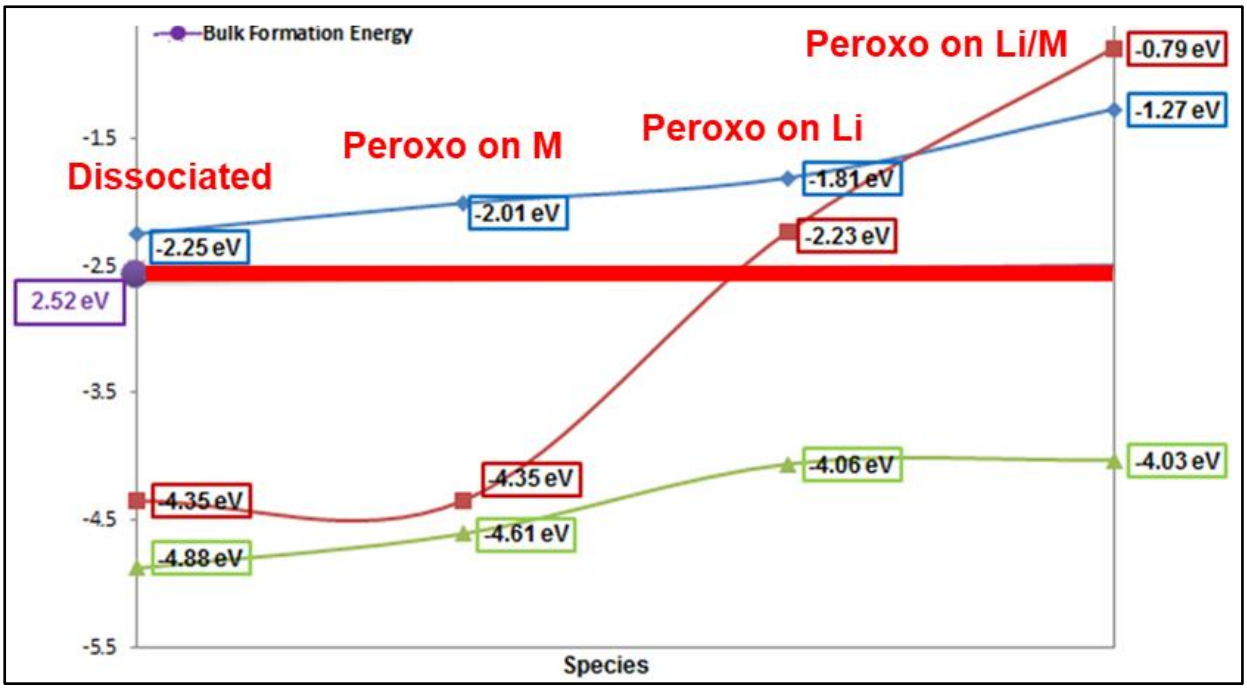

Figure 4.20: MO_2 surface (110) adsorption and lithium peroxide bulk energetics.

The behaviour of the systems is characterized by how the frameworks are associated with the Fermi level, which ordinarily results in finding a way of classifying the metallic, semiconductor, and insulator behaviour.

4.7. Summary

In this chapter, the mechanical and electronic properties were effectively obtained from the DFT using the Vasp and CASTEP codes. The k-points used throughout the calculations are 6x6x1 for all the (110) surface systems. The mechanical properties of the clean (110) surfaces are determined and compared to each other to check if they correspond to one another, where both the MnO_2 and TiO_2 surfaces were found to be stable. The negative C_{44} value for VO_2 led to negative vibrational frequency along the gamma region of the Brillouin zone. The electronic properties such as the electronic band structures and the density of states were successfully obtained for the clean (110) surfaces. Oxygen adsorption on the Li/MO_2 resulted in configurations such as

the dissociated, peroxo on Li, peroxo on Li/M, and peroxo on M. The stability of these specified arrangements was distinguished by how much contribution each system makes at the Fermi level. The high density of states means the system is less stable compared to the one with a low density of states at the Fermi level. The electronic band structures corresponded well with the attained density of states.

Chapter 5: Electronic properties in Sodium air batteries

5.1 Introduction

In this chapter, it is important to understand charge transfer reactions that produce the potential difference in the battery from the Na adatom to the surface M (Mn, Ti, and V) to have lithium-air that are productive [30]. We calculated the electronic properties of the oxygen adsorption at the Na/MO_2 (110) surfaces. Band structures were calculated to check the nature of the system, the density of states was calculated where the stability of the systems was compared.

5.2 Structural aspects

5.2.1 Oxygen adsorption at the Na/MO_2 (110) surface

The mode of transfer of an electron from a Na adatom to a surface M cation using Bader analysis is considered as studied before [30]. The first step is to determine onto which surface site Na preferentially adsorbs. Different possible adsorption sites on the surface were systematically tested and the results are reported in the previous study [30], it was found that the Na adatoms are more the stable in the site of lower oxygen coordination. The discharge products during the cycling of Na air batteries are NaO_2 and Na_2O_2. It was reported that there is no trend in terms of most stable surface, the most stable configuration is the superoxide group on sodium which encourages the formation of NaO_2. The most stable configuration for the adsorption of oxygen on the Na/TiO_2 is the configuration with the dissociated whilst the most stable configuration for the adsorption of oxygen on Na/VO_2 is the configuration with peroxo on the surface V and adsorbed Na.

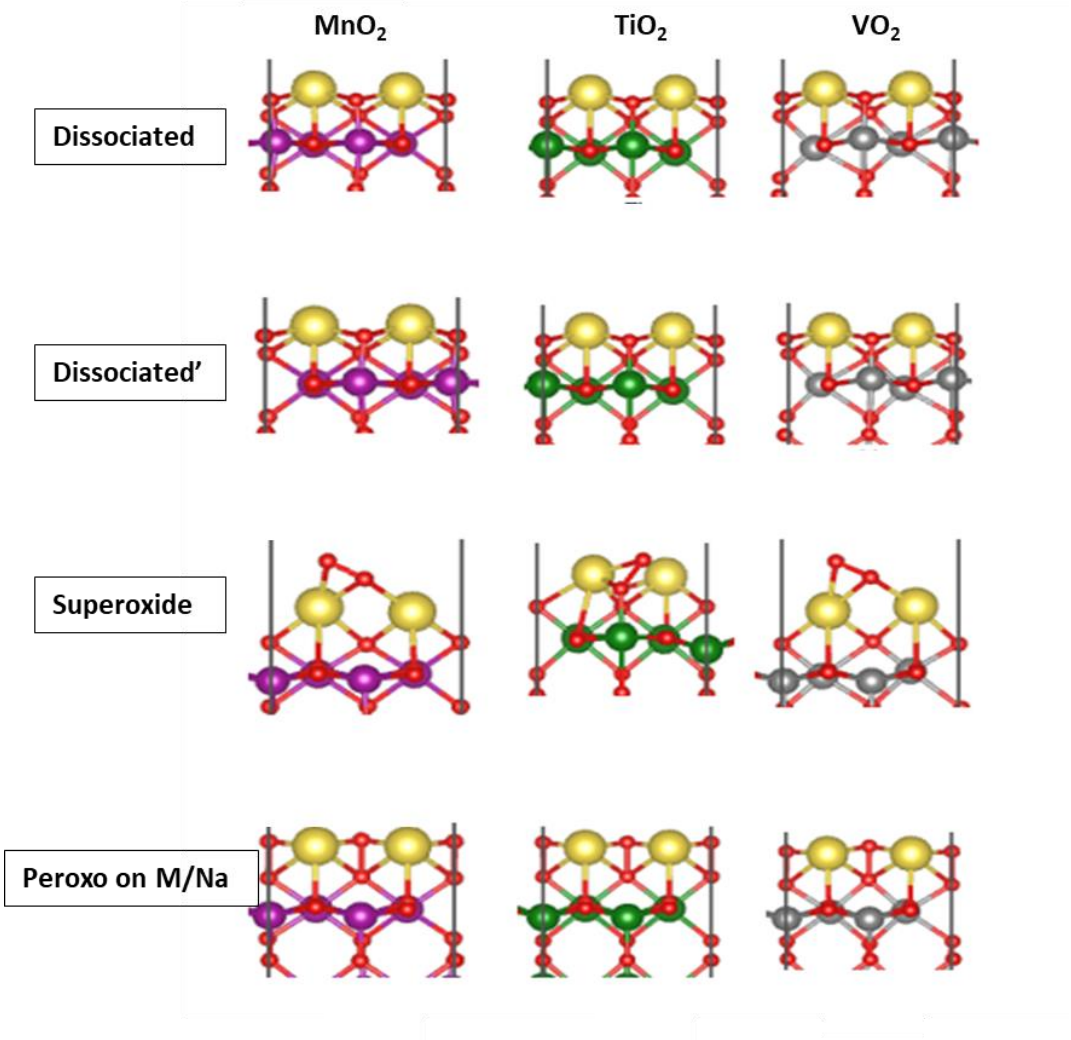

Figure 5.1: Stable adsorption configurations for two oxygen atoms at Na (a) MnO_2, (b) TiO_2, and (c) VO_2 (110) surface {M=Mn, Ti, & V}.

5.3 Electronic properties

5.3.1 Electronic band structures

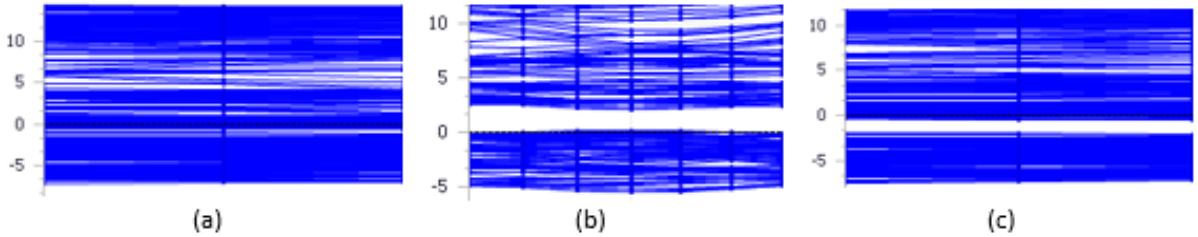

Figure 5.210: Electronic band structures of (a) $(NaTi_4O_9)_4$, (b) $(NaMn_4O_9)_4$, and (c) $(NaV_4O_9)_4$ of dissociated surfaces.

The calculated electronic band structures from all the systems $(NaMn_4O_9)_4$, $(NaTi_4O_9)_4$, and $(NaV_4O_9)_4$ confirm an absence of a gap at the fermi level. Consequently, all the systems are metallic.

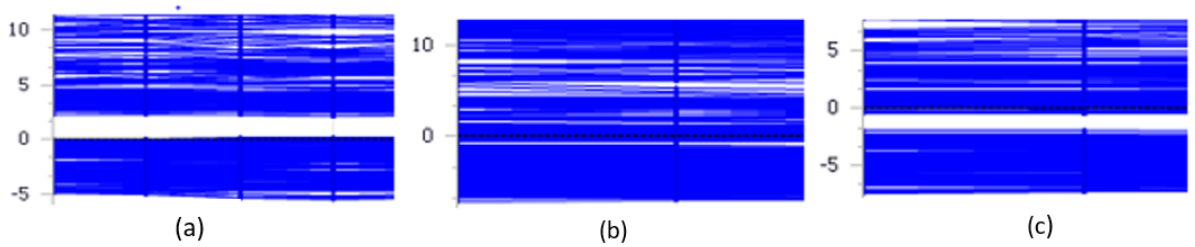

Figure 5.3: Electronic band structures of (a) $(NaTi_4O_9)_4$, (b) $(NaMn_4O_9)_4$, and (c) $(NaV_4O_9)_4$ of dissociated' surfaces.

The calculated band structure for $(NaMn_4O_9)_4$ demonstrates the existence of a direct gap at the fermi level of about 0.032 eV thus, the system is a semiconductor. Furthermore, there is an absence of an electronic band gap at the fermi level for both $(NaTi_4O_9)_4$ and $(NaV_4O_9)_4$ thus the systems are metallic.

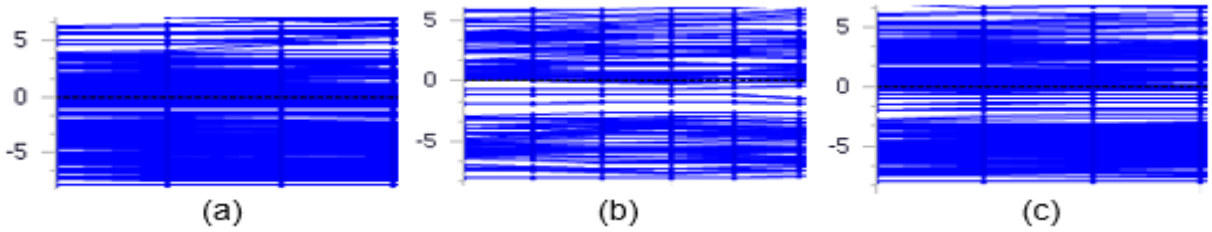

Figure 5.4: Electronic band structures of (a) $(NaTi_4O_9)_4$, (b) $(NaMn_4O_9)_4$, and (c) $(NaV_4O_9)_4$ of peroxo on M/Na.

The calculated electronic band structures from all the systems $(NaMn_4O_9)_2$, $(NaTi_4O_9)_4$, and $(NaV_4O_9)_4$ approve an absence of a gap at the fermi level. Consequently, all the systems are metallic.

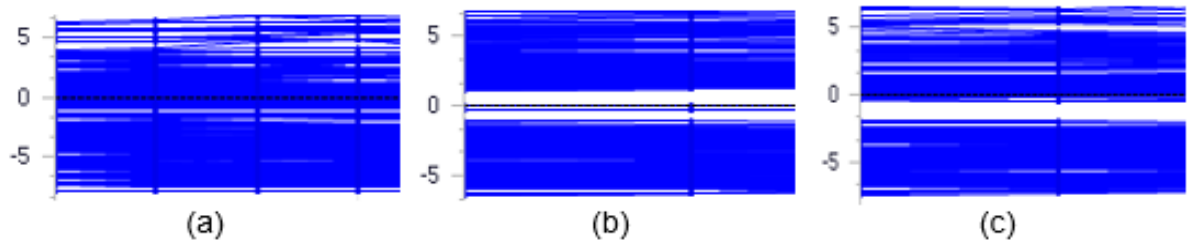

Figure 5.5: Electronic band structures of (a) $(NaTi_4O_9)_4$, (b) $(NaMn_4O_9)_4$, and (c) $(NaV_4O_9)_4$ of superoxide.

The calculated band structure for $(NaMn_4O_9)_4$ reveals the existence of a direct gap at the fermi level of about 1.135 eV thus, the system is a semiconductor. Moreover, there is an absence of electronic band gap at the fermi level for both $(NaTi_4O_9)_4$ and $(NaV_4O_9)_4$ thus the systems are metallic.

5.3.2 Density of states

The graphs below show the total density of states (TDOS) oxygen adsorption at the Na/MO_2 (110) surface. The density of states (DOS) is expressed in the number of states per atom per energy interval. We plot TDOS to examine the differences in the structural stability of each atom, related to the details of the contribution of the atoms at the fermi level concerning the pseudo gap. The structure with the highest and lowest density of states at E_f is examined as the least and most stable, respectively.

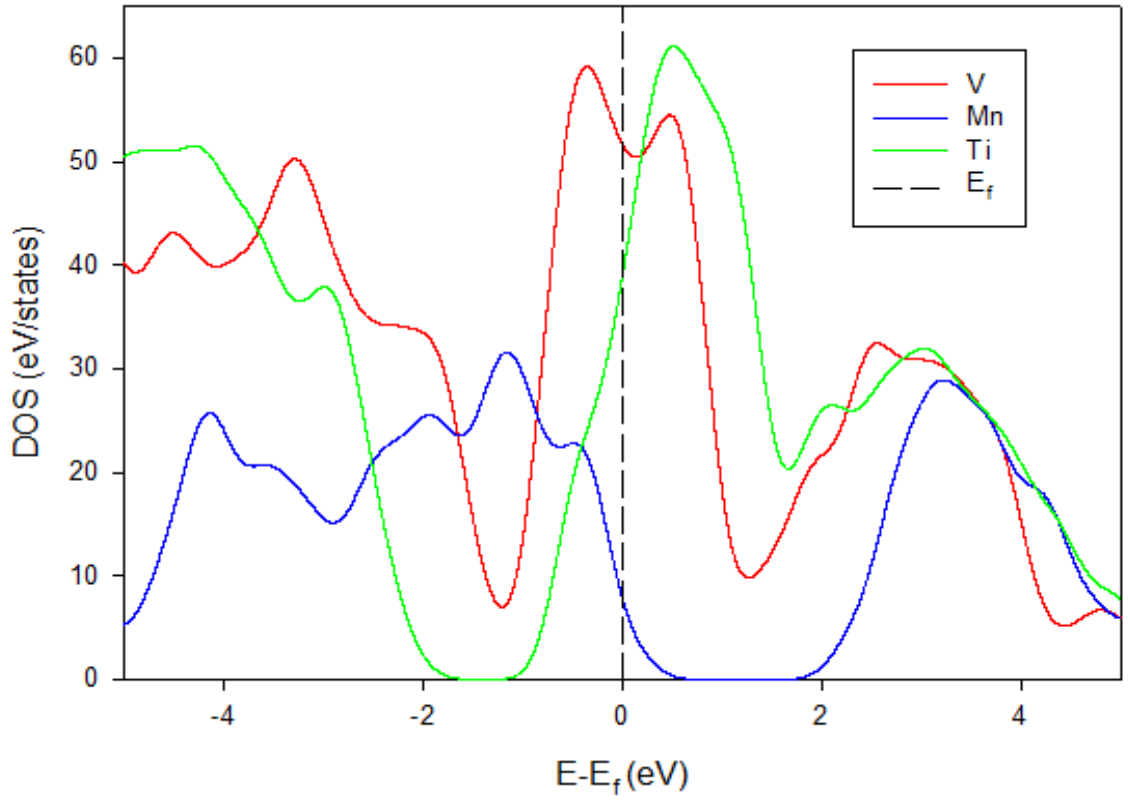

Figure 5.6: Comparison of the total density of states for the dissociated surfaces.

The graph above (Fig 5.6) shows the total density of states (TDOS) for $(NaMn_4O_9)_4$, $(NaTi_4O_9)_4$, and $(NaV_4O_9)_4$ surfaces. The density of states (DOS) is expressed in the number of states per atom per energy interval. We notice that towards E_f the DOS peak of $(NaMn_4O_9)_4$ has a lower density of states which suggest that it is the most stable structure. Furthermore, we notice that $(NaTi_4O_9)_4$ and $(NaV_4O_9)_4$, both have a higher density of states at E_f compared to $(NaMn_4O_9)_4$. The DOS for $(NaV_4O_9)_4$ has a higher density of states at E_f, indicating that it is the least stable structure. The stability trend can be written as $(NaMn_4O_9)_4 > (NaTi_4O_9)_4 > (NaV_4O_9)_4$.

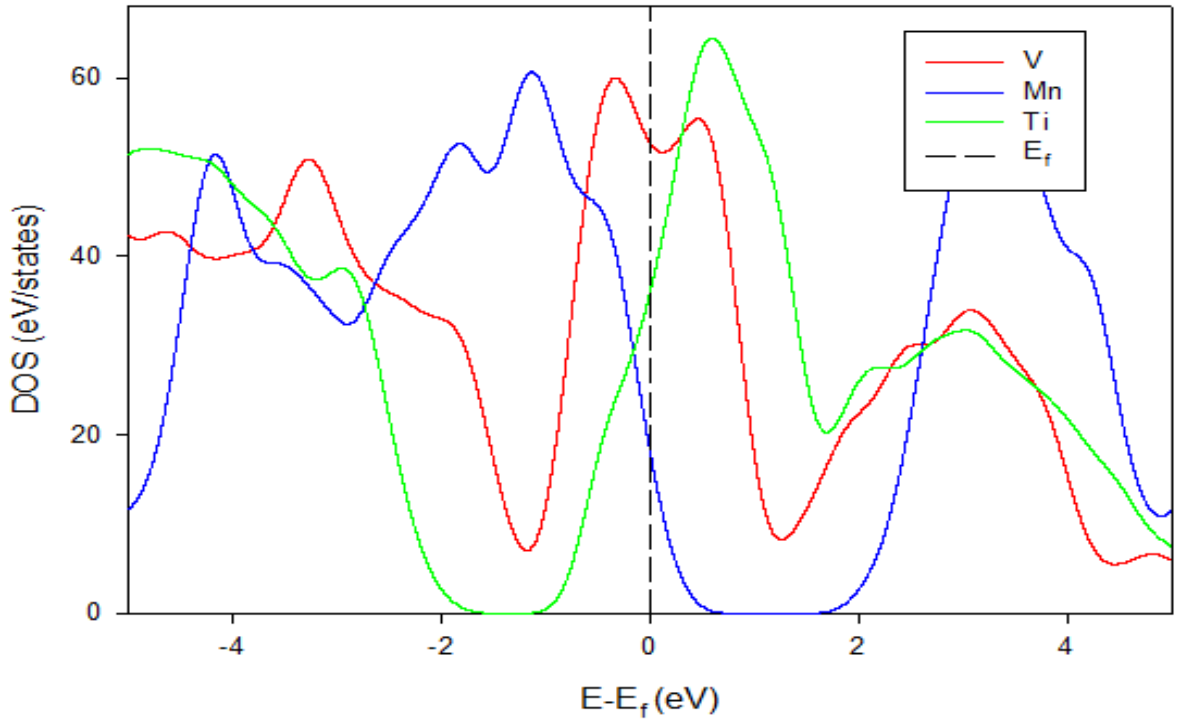

Figure 5.7: Comparison of the total density of states for the dissociated' surfaces.

The graph above (Fig 5.7) shows the total density of states (TDOS) for $(NaMn_4O_9)_4$, $(NaTi_4O_9)_4$, and $(NaV_4O_9)_4$ surfaces. The density of states (DOS) is expressed in the number of states per atom per energy interval. We notice that towards E_f the DOS peak of $(NaMn_4O_9)_4$ has a lower density of states which certifies that it is the most stable structure. Moreover, we notice that $(NaTi_4O_9)_4$ and $(NaV_4O_9)_4$, both have a higher density of states at E_f compared to $(NaMn_4O_9)_4$. The DOS for $(NaV_4O_9)_4$ has a higher density of states at E_f, indicating that it is the least stable structure. The stability trend can be written as $(NaMn_4O_9)_4 > (NaTi_4O_9)_4 > (NaV_4O_9)_4$.

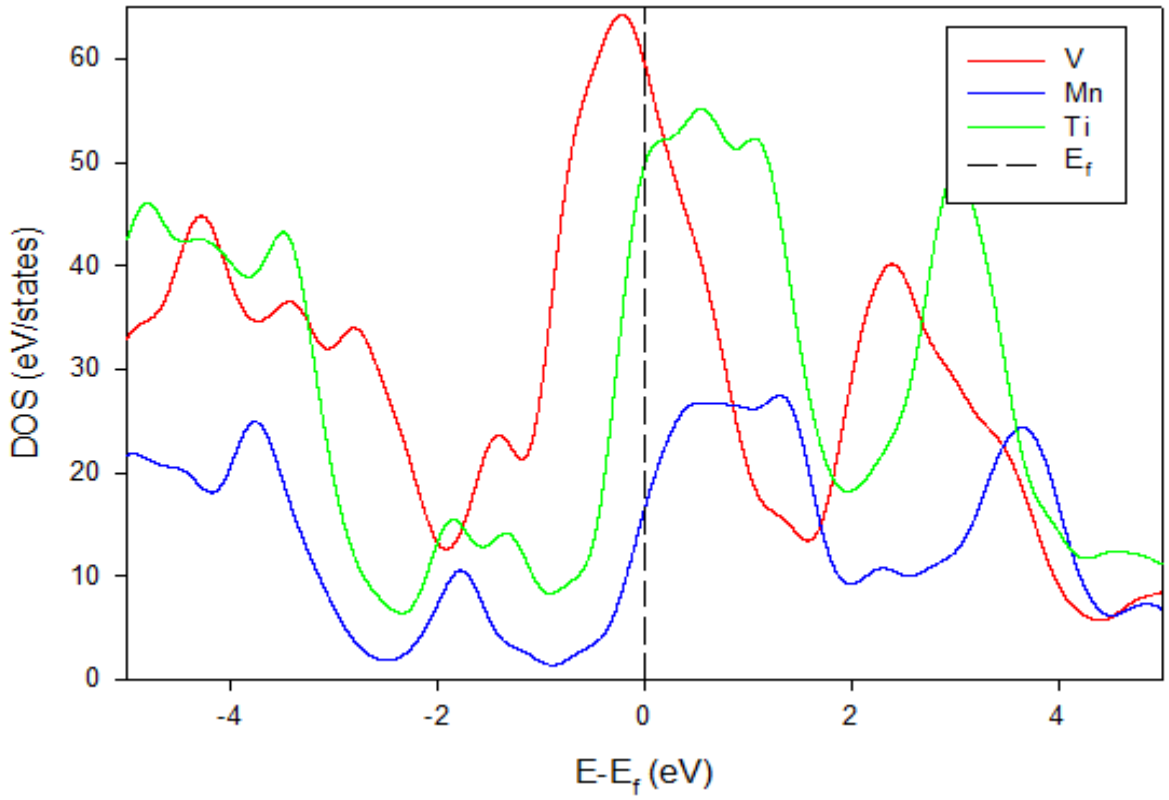

Figure 5.8: Comparison of the total density of states for the peroxo on M/Na surfaces.

The graph above (Fig 5.8) shows the total density of states (TDOS) for $(NaMn_4O_9)_4$, $(NaTi_4O_9)_4$, and $(NaV_4O_9)_4$ surfaces. The density of states (DOS) is expressed in the number of states per atom per energy interval. We notice that towards E_f the DOS peak of $(NaMn_4O_9)_4$ has a lower density of states which indicates that it is the most stable structure. Likewise, we notice that $(NaTi_4O_9)_4$ and $(NaV_4O_9)_4$, both have a higher density of states at E_f compared to $(NaMn_4O_9)_4$. The DOS for $(NaV_4O_9)_4$ has a higher density of states at E_f, suggesting that it is the least stable structure. The stability trend can be written as $(NaMn_4O_9)_4 > (NaTi_4O_9)_4 > (NaV_4O_9)_4$.

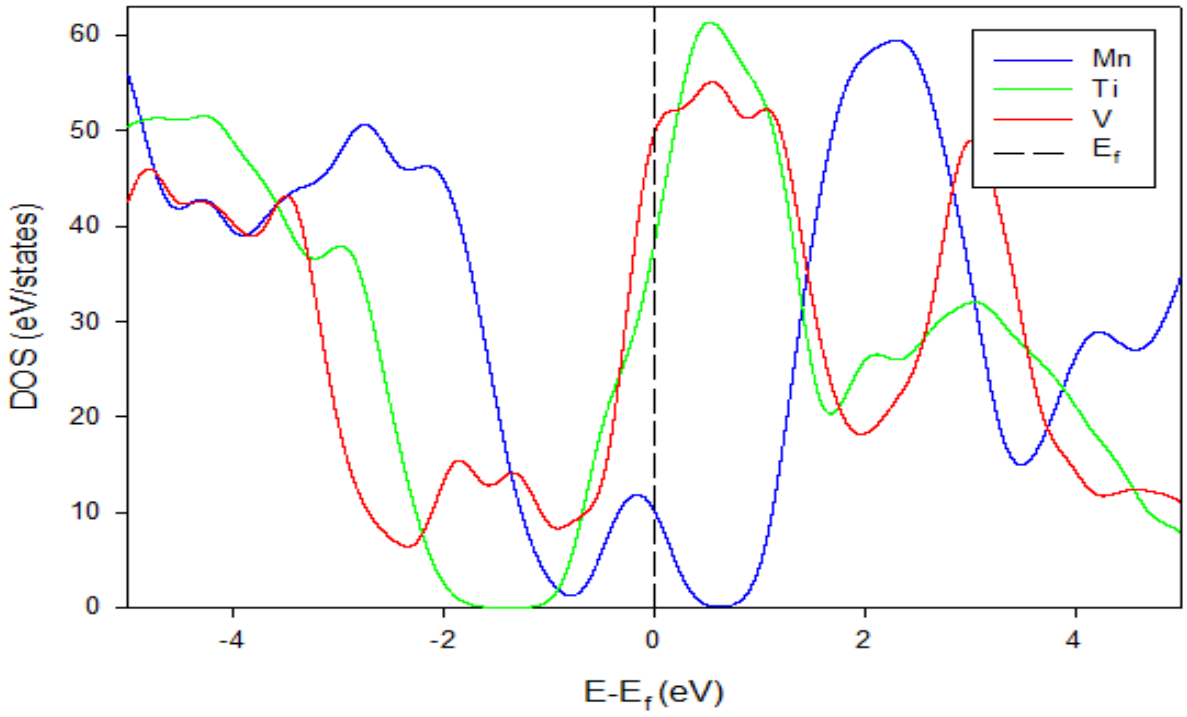

Figure 5.9: Comparison of the total density of states for the superoxide surfaces.

The graph above (Fig 5.9) shows the total density of states (TDOS) for $(NaMn_4O_9)_4$, $(NaTi_4O_9)_4$, and $(NaV_4O_9)_4$ surfaces. The density of states (DOS) is expressed in the number of states per atom per energy interval. We notice that towards E_f the DOS peak of $(NaMn_4O_9)_4$ has a lower density of states which suggests that it is the most stable structure. Similarly, we notice that $(NaTi_4O_9)_4$ and $(NaV_4O_9)_4$, both have a higher density of states at E_f compared to $(NaMn_4O_9)_4$. The DOS for $(NaV_4O_9)_4$ has a higher density of states at E_f, implying that it is the least stable structure. The stability trend can be written as $(NaMn_4O_9)_4 > (NaTi_4O_9)_4 > (NaV_4O_9)_4$.

As observed above, the resulting configurations after oxygen adsorption at Na/MO_2 on (110) surfaces are dissociated, dissociated', peroxo on M/Na, and superoxide. All configurations yield the same trend of stability since the density of states for $(LiMn_4O_9)_4$ intercepts the Fermi level at a lowest point, followed by $(LiTi_4O_9)_4$ at a higher value and $(LiV_4O_9)_4$ at the highest; $(NaMn_4O_9)_4 > (NaTi_4O_9)_4 > (NaV_4O_9)_4$. Such trends are

affirmed by the catalytic activities of MO_2 surfaces, shown in figure 5.10 reported by [92].

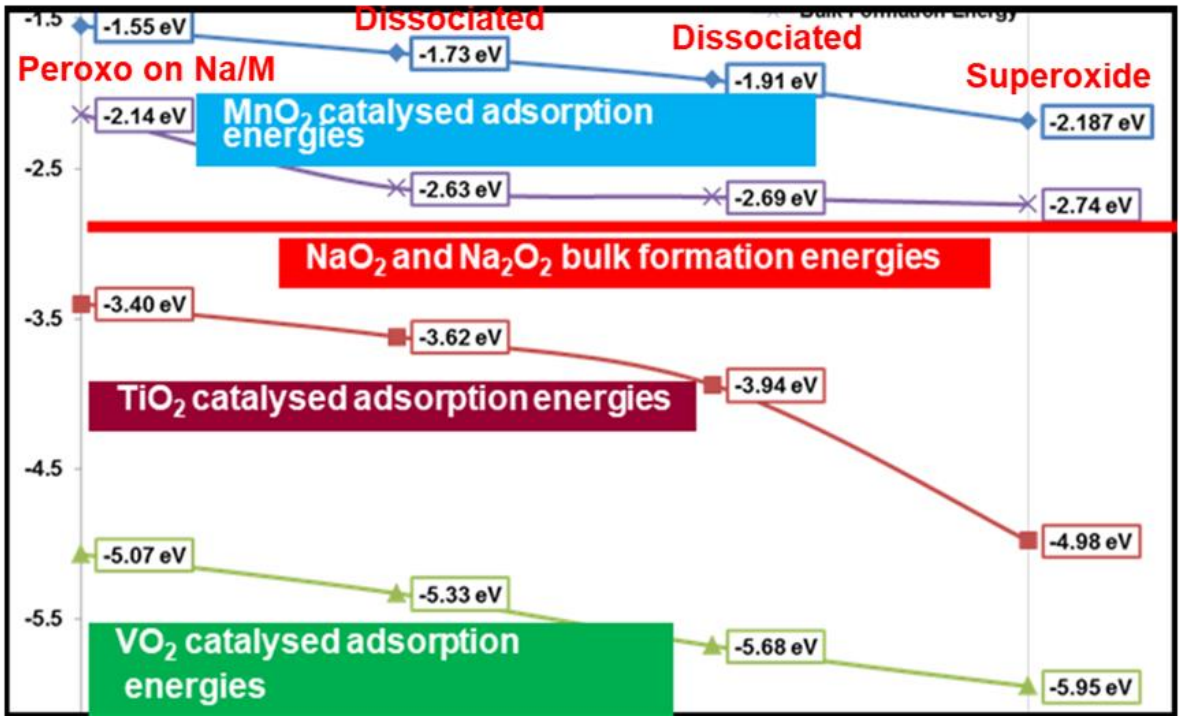

Figure 5.10: MO_2 surface (110) adsorption and sodium peroxide bulk energetics.

5.4 Summary

In this chapter, the electronic properties were successfully obtained from the DFT using the Vasp and CASTEP codes. The electronic properties such as the electronic band structures and the density of states were successfully achieved for oxygen adsorption on the Na/MO_2 and resulted in configurations such as the dissociated, superoxide, peroxo on Na/M, and dissociated'. The stability of these mentioned configurations was distinguished by how much contribution each system makes to the fermi level. The high density of states means the system is less stable compared to the one with a low density of states at the Fermi level. The electronic band structures corresponded well with the attained density of states.

Chapter 6: Conclusions

6.1 Conclusions

We present a new method, which mainly deals with large systems. The self-consistent density functional tight binding approach (SCC-DFTB) method is used to develop potentials, to obtain the structural and electronic properties of β-MnO_2 accurately. The major advantage of the SCC-DFTB over the typical tight-binding (NCC-DFTB) and other techniques is the introduction of Coulomb interaction between charge fluctuations. We successfully derived parameter for Mn-O and O-O interactions using different reference systems such as MnO_2, O, and Mn using a DND basis set. These structures were first subjected to geometry optimization using the $DMol^3$ code before parameterization was performed. The calculated or obtained lattice parameters for β-MnO_2 structure are in good agreement with the experimental and DFT results, for which they are within 2% of percentage difference. The electronic properties calculated from these lattice parameters were in good agreement or were comparable with the DFT results.

Moreover, to provide a better understanding of the catalytic activity of MnO_2, TiO_2, and VO_2 for the oxygen evolution and oxygen evolution reactions in both Li-air and Na-air, density functional theory is used to calculate different properties of MO_2, Li/MO_2, and Na/MO_2 such as structural, mechanical, and electronic properties. The surfaces of MO_2 found the (110) plane to be the most stable of them all, hence the (110) was used in all the MO_2 calculations.

The mechanical properties of the clean surfaces were successfully calculated. The elastic properties and the phonon density of states are in good agreement. Looking at the elastic properties of MO_2 both MnO_2 and TiO_2 were found to be mechanically stable

since all the stability criteria for orthorhombic were met. However, the VO_2 system was found to have a negative value for C_{44} which led it to be unstable since the stability criteria for orthorhombic was not met. The B/G ratio for MnO_2 and TiO_2 is found to be brittle since the B/G < 1.75. However, VO_2 is ductile since B/G > 1.75. The phonon calculations obtained for the MO_2 systems seem to be in good agreement with the elastic properties discussed. The TiO_2 and MnO_2 systems were found not to have soft modes along Γ direction, which suggest that both structures are vibrationally stable. But only imaginary modes are observed along the Z, A, and R direction for MnO_2 for it does not make the system to be unstable. The VO_2 system appears to have soft modes along Γ direction this suggests that the system is vibrationally unstable. The soft modes along the Γ direction are the results of the negative value of C_{44} found from the elastic properties of VO_2. Hence the stability trend from the phonon dispersion is written as $TiO_2 > MnO_2 > VO_2$.

The electronic properties of the clean surfaces of MO_2 were calculated and compared, and the density of states. The stability of surfaces was determined in such a way that one with a higher density of states at the Fermi level is regarded as less stable and the system with a low density of states is more stable. The MnO_2 was found to be the most stable surface since it has a low density of states as compared to VO_2 since it has a higher number of density of states. From all the observations from the clean surfaces the stability trend can be written as $MnO_2 > TiO_2 > VO_2$. After the Li adsorption to the MO_2 there were no changes to the stability trend $(LiMn_8O_{16})_2 > (LiTi_8O_{16})_2 > (LiV_8O_{16})_2$.

Following the oxygen adsorption at the Li/MO_2, different configurations occurred namely, peroxo on Li, peroxo on Li/M, peroxo on M and dissociated; and related electronic properties were successfully calculated. In case of peroxo on Li, peroxo on

Li/M, and peroxo on M configurations the trend of stability remained unchanged and is like those of pure and Li doped surfaces, i.e. $(LiMn_4O_9)_4$ > $(LiTi_4O_9)_4$ > $(LiV_4O_9)_4$. However, for the dissociated configuration the stability trend is different, where the $(LiTi_4O_9)_4$ appears where the Fermi level intercepts the density of states at a lower point compared to the other systems. The density of states of $(LiV_4O_9)_4$ was intercepted at a higher point and that of $(LiMn_4O_9)_4$ was in between; hence the resulting stability trend is $(LiTi_4O_9)_4$ > $(LiMn_4O_9)_4$ > $(LiV_4O_9)_4$. The electronic band structures from all the calculated surfaces were in good agreement with the DOS obtained.

When oxygen is adsorbed at the Na/MO_2, different configurations were obtained specifically dissociated, superoxide, peroxo on Na/M, and dissociated'. The electronic properties were successfully calculated, and for all configurations it was found that the $(NaMn_4O_9)_4$ has a low density of states at the Fermi level, whereas the $(NaV_4O_9)_4$ has the highest density of states, suggesting that it is less stable. However, the $(NaTi_4O_9)_4$ densities of states suggest that stabilities of related configurations are lying between those of $(NaMn_4O_9)_4$ and $(NaV_4O_9)_4$. Hence the stability trend from the Na/MO_2 can be written as $(NaMn_4O_9)_4$ > $(NaTi_4O_9)_4$ > $(NaV_4O_9)_4$ for all configurations. The electronic band structures obtained from Na/MO_2 are in good agreement with the DOS attained. The observed trend is consistent with catalytic activities of the metal oxides deduced from adsorption energies [92].

6.2 Recommendations

Factors to consider when parameterizing:

DFT and DFTB calculations

For data generation required by the fitting process energy calculations (and force calculations if requested) are done twice. One calculation is a DFT calculation, for

which the DFTB+ Parameterization task uses DMol^3. The other calculation uses DFTB+ with the Slater-Koster files that were generated from the electronic part. For heavy elements, the DFT calculations, for both the repulsive part (DMol^3) and the electronic part, need to include relativistic effects. For the DFTB+ electronic fitting, the Zero Order Regular Approximation (ZORA) formalism is used. These relativistic calculations are activated for elements with an atomic number greater than 36 (Kr).

Once the energies and forces have been derived from both the DFT and DFTB calculations for all the sample systems it is possible to fit the coefficients of the polynomials for the repulsive terms to this data. This uses a standard least-squares fitting technique. The fitting process is performed several times; for different orders of the polynomials and for different values of the cut-off radii around which the polynomials 53 are based. The best fit from all these trials is used for the final set of

Once the polynomial coefficients have been calculated, the Slater-Koster files containing just the electronic part are updated to include the repulsive part. These are then used to generate fully functional Slater-Koster files. All the individual files are packaged up, together with some auxiliary data, into a single Slater-Koster library file. This form can be used by other DFTB+ tasks.

References

[1] D. Deng, *Energy Science and Engineering,* vol. 5, pp. 385-418, 2015.

[2] Z.P. Cano, D. Banham, Y. Siyu, A. Hintennach, J. Lu, M. Fowler, and Z. Chen, *Nature Energy,* vol. 3, pp. 279-289, 2018.

[3] H. Ye, M. Li, Liu T, Y. Li, J. Lu, *ACS Energy Lett.,* vol. 5, pp. 2234-2245, 2020.

[4] P. Zhang, Y. Zhao, X.B. Zhang, *Chem. Soc. Rev.,* vol. 47, pp. 2921-3004, 2018.

[5] J. Ryu, M. Park, J. Cho, *Adv. Mater.,* vol. 31, p. 1804784, 2019.

[6] K.P. Maenetja and P.E. Ngoepe, Density functional theory study of (110) β-MnO2, β-TiO2 and β-VO2 surface in metal-air batteries, Polokwane, 2017.

[7] K.D. Rogers, *Powder Diffr,* vol. 8, p. 240, 1993.

[8] L.A.H. MacLean and F.L. Tyle, *J. Solid State Chem.,* vol. 123, p. 150, 1996.

[9] S.C. Abrahams and J.L. Bernstein, *J. Chem. Phys.,* vol. 55, p. 3206, 1971.

[10] C. Greenwood, N. Norman and A. Earnshaw, Chemistry of elements, Oxford: Elsevier, 2012.

[11] M. Park, H. Sun, H. Lee, J. Lee, J. Cho, *Adv. Energy Matt.,* vol. 2, pp. 780-800, 2012.

[12] G. A. E. Oxford and A. M. Chaka, *J. Phys. Chem C.,* vol. 115, pp. 16992-7008, 2011.

[13] H. Perron, C. Domain, J. Roques, R. Drot, E. Simoni, H. Catalette, *Theor Chem Acc,* vol. 117, pp. 565-574, 2007.

[14] A. Thomas, K.P. Maenetja, P.E. Ngoepe, M. Scott, C. Woodley, A. Richard, R. Grau-Crespo, *J. Mater. Chem A,* vol. 1, pp. 14799-15168, 2013.

[15] T.A. Mellan, and R. Grau-Crespo, *J. Chem. Phys,* vol. 137, p. 154706, 2012.

[16] R.R. Maphanga, S.C. Parker and P.E. Ngoepe, *Surface science,* vol. 603, pp. 3184-3190, 2009.

[17] Y. Shao, S. Park, J. Xiao, J. Zhang, Y. Wang, and J. Liu, *ACS Catalysis,* vol. 2, pp. 844-857, 2012.

[18] W. Dai, H. Wang, X.Z. Yuan, J.J. Martin, D. Yang, J. Qiao, J.A. Ma, *Journal of hydrogen energy,* vol. 34, pp. 9467-9478, 2009.

[19] Q. Sun, Y. Yang and Z.W. Fu, *Electrochem. Commun,* vol. 16, pp. 22-25, 2012.

[20] J. Kim, H. Lim, H. Gwon, and K. Kang, *J. Phys. Chem. Chem. Phys.,* vol. 15, pp. 3623-3629, 2013.

[21] W. -W. Yin, Z. Shadike, Y. Yang, F. Ding, L. Sang, H.Li, and Z. Fu, *Chem. Commun.,* vol. 51, pp. 2324-2327, 2015.

[22] Z. Khan, M. Vagin, X. Crispin, *Advance science,* vol. 7, p. 1902866, 2020.

[23] S. Kang, Y. Mo, S.P. Ong, and G. Ceder, *Nano Lett,* vol. 14, pp. 1016-1020, 2014.

[24] P. Hartmann, C.L. Bender, J. Sann, and A.K. Durr, *Phys. Chem. Chem. Phys.,* vol. 15, pp. 11661-11672, 2013.

[25] P. Ravindram, L. Fast, P.A. Korzhayvi, B. Johansson, J. Willis, and O. Eriksson, *J. Appl. Phys.,* vol. 84, pp. 4891-4904, 1998.

[26] S.J. Blundell, and K.M. Blundell, Concepts in Thermal Physics, New York: Oxford University Press, 2009.

[27] C. Kittel, Elementary statistical Physics, Courier Corparation, 2004.

[28] W. Drube, I. Schafer, M. Skibowski, *J. Phys C: Solid state Phys.,* vol. 20, p. 4201, 1987.

[29] G. Mulatedzi, Computer modelling study of TiO2 nanotubes, Polokwane, 2019.

[30] T.A. Mellan, K.P. Maenetja, P.E. Ngoepe, S.C. Woodley, C. Richard, A. Catlow, and R. Grau-Crespo, *J. Material Chemistry A.,* vol. 1, pp. 14799-15168, 2013.

[31] R.G. Parr, S.K. Ghosh, *Proceedings of the national academy of sciences of the united state of america,* vol. 83, pp. 3577-3579, 1986.

[32] N.M. Kinnunen, J.T. Hirvi, M. Suvanto, T.A. Pakkanen, *J. Phys Chem,* vol. 115, pp. 19197-19202, 2011.

[33] E. Wimmer, *Material Science and Engineering: B.,* vol. 37, pp. 72-82, 1996.

[34] A.E. Mattsson, P.A. Schultz, M.P. Desjarlais, T.R. Mattsson, K. Leung, *Modelling and Simulation in Material Science and Engineering,* vol. 13, pp. 1-31, 2005.

[35] R.G. Parr, W.T. Yang, Density functional theory of atoms and molecules, Oxford University Press, 1989.

[36] K. Horn, M. Scheffler, Electronic Structure (Handbook of Surface Science), Elsevier, 2000.

[37] D.J.W. Geldart, and M. Rasolt, *Phys. Rev. B,* vol. 13, p. 1477, 1976.

[38] G.P. Robert, and Y. Weltao, Density-Functional Theory of Atoms and Molecules, Oxford: Oxford University Press, 1994.

[39] P.A.M. Dirac, Note on Exchange Phenomena in the Thomas-Fermi Atom, vol. 26, Cambridge: Cambridge university press, 1930.

[40] J.P. Perdew, K. Burke, Y. Wang, *Physical Review Letters,* vol. 54, pp. 16534-16539, 1996.

[41] D.J.W. Geldart, M. Rasolt, *Phys. Rev B.,* vol. 13, p. 1477, 1976.

[42] J.P. Perdew, *Phys. Rev B.,* vol. 172, p. 6, 1991.

[43] J.P. Perdew, K. Burke, M. Ernzerhof, *Physical Review Letters,* vol. 77, pp. 3865-3868, 1996.

[44] J.P. Perdew, J.A. Chevary, S.H. Vosko, K.A. Jakson, M.R. Pederson, D.J. Singh, C. Fiolhais, *Phys. Rev B.,* vol. 46, p. 6671, 1992.

[45] K. Yang, J. Zheng, Y. Zhao, D.G. Truhlar, *J. Chem. Phys.,* vol. 132, p. 164117, 2010.

[46] Y. Zhang, W. Yang, *Physical Review Letter,* vol. 890, p. 80, 1998.

[47] W. Matthew, C. Foulkes, *Phys. Rev B.,* vol. 39, pp. 12520-12536, 1989.

[48] Th. Frauenheim, G. Seifert, M. Elstner, Z. Hajnal, G. Jungnickel, D. Porezag, S. Suhai, R. Scholz, *Physical Status Solid B.,* vol. 217, pp. 41-62, 2000.

[49] M. Elstner, D. Porezag, G. Junnickel, J. Elsner, M. Haugk, Th. Frauenheim,S. Suhai, G. Seifert, *Phys. Rev. B.,* vol. 11, pp. 7260-7268, 1998.

[50] K. Jolla, J.W. Matthew, H. Kersti, C. Christof, *J. Phys. Chem.,* vol. 8, pp. 4593-4607, 2017.

[51] G. Dolgonos, B. Aradi, N.H. Moreira, T. Frauenheim, *J. Chemical Theory and Computatin,* vol. 6, p. 266=278, 2010.

[52] M. Elstner, T. Frauenhelm, S. Suhai, *J. Molecular Structures,* vol. 632, pp. 29-41, 2003.

[53] G. Dolgonos, B. Aradi, N.H. Moreira, Th. Frauenheim, *J. Chem. Theory Comput.,* vol. 6, pp. 266-278, 2010.

[54] R.S. Mulliken, *J. Chem. Phys.,* vol. 23, pp. 1833-1840, 1955.

[55] R.G. Parr, R.G. Pearson, *J. American Chemical society,* vol. 105, pp. 7512-7516, 1983.

[56] J.F. Janak, *Phys. Rev. B.,* vol. 18, pp. 7165-7168, 1978.

[57] G. Mulatedzi, P.E. Ngoepe, *University of Limpopo,* 2019.

[58] T. Heine, H.F. Dos Santos, S. Patchkovskii, H.A. Duarte, *J. Phys. Chem A.,* vol. 111, pp. 5648-5654, 2007.

[59] J. Frenzel, J. O. Joswig, G. Seifert, *J. Phys. Chem C.,* vol. 111, pp. 10761-10770, 2007.

[60] A. Kuc, A. Enyashin, G. Seifert, *J. Phys. Chem B.,* vol. 111, pp. 8179-8186, 2007.

[61] P. Muller, *Pure and Applied Chemistry,* vol. 66, pp. 1077-1184, 1994.

[62] M. Elstner, P. Hobza, T. Frauenheim, S. Suhai, E.Kaxiras, *J. Chem. Phys.,* vol. 114, pp. 5149-5155, 2001.

[63] L. Zhechkov, T. Heine, S. Patchkovskii, G. Seifert, H. A. Duarte, *J. Chemical Theory and Computation,* vol. 1, pp. 841-847, 2005.

[64] F.O. Augusto, G. Seifert, T. Heine, *Journal of the Brazilian Chemical Society,* vol. 20, pp. 1193-1205, 2009.

[65] A. K. Rappe, C. J. Casewit, K. S. Colwell, W. A. Goddard, W. M. Skiff, *J. American Chemical Society,* vol. 114, pp. 10024-10035, 1992.

[66] L. Zhechkov, T. Heine, S. Patchkovskii, G. Seifert, H. A. Duarte, *J. Chemical Theory and Computation,* vol. 1, pp. 841-847, 2005.

[67] M.C. Payne, M.P. Teter, D.C. Allan, T.A. Arias, J.D. Joannopoulos, *Rev. Mod. Phys,* vol. 64, p. 1045, 1992.

[68] M.L. Cohen, V. Heine, *Solid State Physics,* vol. 25, pp. 37-248, 1970.

[69] J.C. Phillips, *Phys. Rev.,* vol. 112, pp. 685-695, 1958.

[70] J.C. Phillips, L. Kleinman, *Phys. Rev.,* vol. 116, p. 287, 1959.

[71] D. Brust, B. Alder, *Methods in Computational Physics,* vol. 8, p. (Academic Press), 1968.

[72] G.B. Bachelet, D.R. Hamann, M. Schluter, *Phys. Rev. B.,* vol. 26, pp. 4199-4228, 1982.

[73] J.D. Joannopoulos, T.H. Starkloff, M.Kastner, *Phys. Rev. Lett,* vol. 38, p. 660, 1977.

[74] D. Vanderbilt, *Phys. Rev. B.,* vol. 41, pp. 7892-7895, 1990.

[75] B. Delley, *J. Chem. Phys.,* vol. 92, pp. 508-517, 1990.

[76] B. Delley, *J. Chem. Phys.,* vol. 94, pp. 7245-7250, 1991.

[77] G. Kresse, M. Marsman, J. Furthmuller, *Vasp Guide: Computational Physics,* 2009.

[78] J.P. Perdew, *Phys. Rev.,* vol. 6, p. 172, 1992.

[79] V. Milman, B. Winkler, J.A. White,C.J. Pickard, M.C. Payne, E.V. Akhmatskaya and R.H. Nobes, *J. Quant. Chem.,* vol. 77, pp. 895-910, 2000.

[80] D.J. Chadi and M.L. Cohen, *Phys. Rev. B.,* vol. 8, pp. 5747-5753, 1973.

[81] H.J. Monhorst and J.D. Pack, *Phys. Rev. B.,* vol. 13, pp. 5188-5192, 1976.

[82] J.D. Joannopoulos and M.L. Cohen, *Phys. Rev. B.,* vol. 7, pp. 2644-2657, 1973.

[83] R.A Evarestov and V.P. Smirnov, *Phys. Status Solid,* vol. 119, pp. 9-40, 1983.

[84] G. Seifert, *J. Phys. Chem A.,* vol. 111, pp. 5609-5613, 2007.

[85] M.I. Said and B. Harbrecht, *journal of alloys and compounds,* vol. 710, pp. 635-643, 2017.

[86] T. Barudzija, V. Kusigerski, N. Cvjeticanin, S. Sorgic, M. Perovic, and M. Mitric, *Journal of alloys and compounds,* vol. 665, pp. 261-270, 2016.

[87] G. Xiong, K.P.S.S. Hembram, R.G. Reifenberger, and T.S. Fisher, *J. Power Sources,* vol. 227, pp. 254-259, 2013.

[88] Chadi D.J., Cohen M.L., *Phys. Rev B.,* vol. 8, pp. 5747-5753, 1973.

[89] Z. Hu, W. Xu, C. Chen, Y. Wen, L. Liu, vol. 13, China: Advanc. Matt. Science and Engineering, 2018, pp. 5188-5198.

[90] A. Poredda, V.A. Lovchikov, K. Jug, Development of Sindo1 for Extended Systems, Springer, Boston, MA, 1992, pp. 641-650.

[91] K.P. Maenetja and P.E. Ngoepe, *J. electrochem. Soc.,* vol. 168, no. 7, p. 070556, 2021.

[92] K.P. Maenetja and P.E. Ngoepe, "Unravelling Catalytic Activity of MnO_2, TiO_2, and VO_2 (110) Surface by Oxygen Co-adsorption Sodium Adsorbed MO_2 {M= Mn, Ti, V}," *ACS,* 2022.